

AD-A250 988



①

**Experimental Study of Vortex Ring  
Interaction with a Free Surface**

Jung Tai Kwon  
Department of Aerospace Engineering

**DTIC**  
**S** **ELECTE** **D**  
**C**  
JUN 2 1992

Contract Number N00014-86-K-0684  
Technical Report No. 89-06

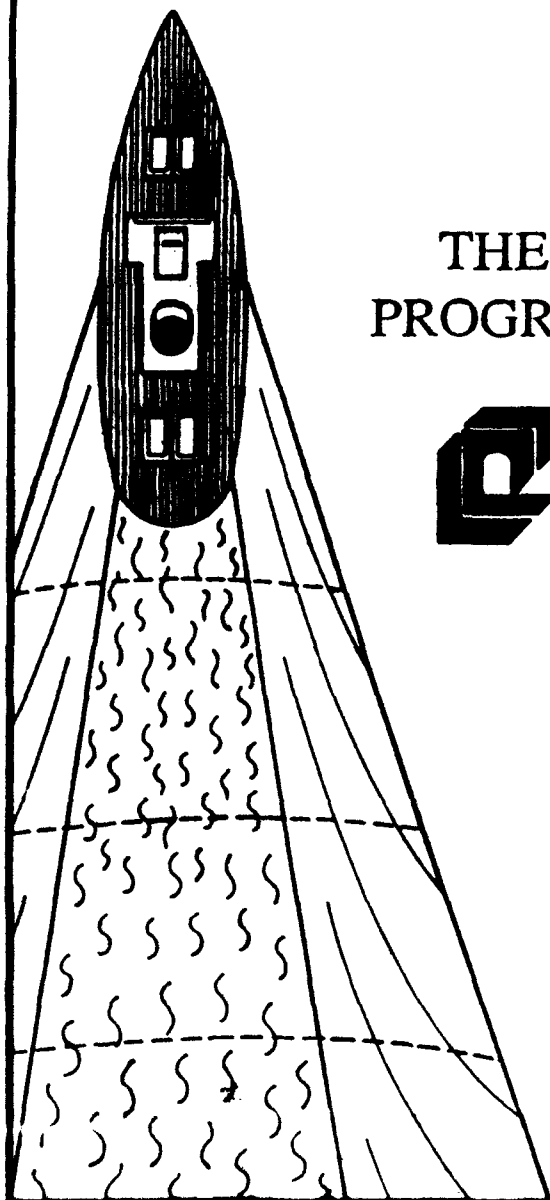
August, 1989

**DISTRIBUTION STATEMENT A**

Approved for public release;  
Distribution Unlimited

92 5 26 011

**92-13785**



# THE UNIVERSITY OF MICHIGAN PROGRAM IN SHIP HYDRODYNAMICS



COLLEGE OF ENGINEERING

NAVAL ARCHITECTURE &  
MARINE ENGINEERING

AEROSPACE ENGINEERING

MECHANICAL ENGINEERING &  
APPLIED MECHANICS

SHIP HYDRODYNAMIC  
LABORATORY

SPACE PHYSICS RESEARCH  
LABORATORY



## ABSTRACT

The results of an experimental investigation on the interaction of vortex rings with a free surface are presented. Laminar vortex rings with Reynolds numbers in the range  $2 \times 10^3$  to  $10 \times 10^3$  were formed underwater at several incidence angles to the free surface. When the vortex core closest to the surface interacts with it, vortex lines are found to disconnect and reconnect with the free surface resulting in open vortex lines beginning and terminating at the surface. Under certain conditions a second reconnection process is observed resulting in a vortex line topology consisting of two semicircles propagating away from each other on divergent paths. This double reconnection of vortex rings at a free surface is documented in detail by flow visualization and surface velocity field measurements. A new technique was developed to measure the velocity field at the free surface using Laser Speckle Photography and automated digital image analysis. Test results show the accuracy of the velocity measurement to better than 1%.

It is further shown that the interaction geometry when the vortex ring moves initially parallel to the surface is independent of the ring Reynolds number. The effect of Reynolds number on reconnection time is also investigated and showed to be independent of Reynolds number. It is however quite sensitive to the incidence angle.

The effect of free surface contamination is investigated at an incidence angle of  $90^\circ$ . The results show the formation of secondary and tertiary rings with a contaminated surface. With a cleaner surface the formation of a secondary ring is delayed.

Statement A per telecon  
Dr. Edwin Rood ONR/Code 1132  
Arlington, VA 22217-5000

NWW 6/1/92



Accession For	
NTIS GRA&I	<input checked="" type="checkbox"/>
DTIC TAB	<input type="checkbox"/>
Unannounced	<input type="checkbox"/>
Justification	
By	
Distribution/	
Availability Codes	
Dist	Avail and/or Special
A-1	

## **ACKNOWLEDGEMENTS**

I would like to acknowledge those who gave me special help during my stay at the University of Michigan.

I would also like to thank the financial support of the Agency for Defense Development in Korea as well as support from the office of Naval Research, Contract no. N000184-86-K-0684 under the URI Program for Ship Hydrodynamics, and the National Science Foundation, Grant no. MSM-850634.

I wish to express special thanks to my advisor, Professor Luis P. Bernal, for his creative suggestions and guidance in this study.

I am grateful to my dissertation committee, Professors. A.Messiter, M.Sichel and G.Tryggvason for providing helpful suggestions on my thesis work.

Most of all, I want to thank my wife, Tan Keum Lee, and our daughter, Young-Sun. Their enduring patience and constant love made this work successful.

## TABLE OF CONTENTS

ABSTRACT.....	ii
ACKNOWLEDGEMENTS.....	iii
LIST OF FIGURES.....	vi
NOMENCLATURE.....	ix
CHAPTER	
I. INTRODUCTION.....	1
II. FLOW FACILITY AND INSTRUMENTATION.....	6
2.1 The Facility	
2.2 Vortex Generator	
2.3 Flow Visualization	
2.4 Hot Film Velocity Measurement	
III. FREE SURFACE VELOCITY FIELD MEASUREMENT.....	12
3.1 General Consideration	
3.2 Fringe Image Analysis	
3.2.1 Image Processing System	
3.2.2 Image Enhancement	
3.2.3 Autocorrelation Technique	
3.2.4 Sensitivity Study	
3.2.5 Implementation	
3.3 Velocity Field Analysis	
3.4 Photographic Recording	
IV. RESULTS AND DISCUSSION.....	26
4.1 The Characteristics of the Vortex Rings	
4.2 Vortex Ring Interaction with Free Surface	
4.2.1 Vortex Ring Parallel to the Free Surface	
4.2.1.1 Contaminated Free Surface	
4.2.1.2 Clean Free Surface	
4.2.2 Normal Incidence to the Free Surface	
4.2.3 Inclined Incidence to the Free Surface	

#### 4.3 The Double Reconnection Process

##### 4.3.1 Flow Visualization

##### 4.3.2 Free Surface Velocity Field

##### 4.3.3 Deformation Rate Field Analysis

V. SUMMARY AND CONCLUSIONS.....	46
FIGURES.....	49
TABLE.....	125
APPENDIX.....	127
BIBLIOGRAPHY.....	129

## LIST OF FIGURES

<u>Figure</u>	<u>Page</u>
1.1 Schematic diagram of the flow geometry	50
2.1 Schematic diagram of the facility	51
2.2 Photograph of the vortex generator	52
2.3 Detail of vortex generator assembly	53
2.4 Vortex generator apparatus	54
2.5 Block diagram of vortex generator driving circuit	55
2.6 Schematic diagram of simultaneous flow visualization system	56
2.7 Schematic diagram of imaging system	57
2.8 Block diagram of hot film velocity measurement system	58
3.1 Schematic diagram of the rotating disk experiment	59
3.2 Photograph of a typical fringe image	60
3.3 Schematic diagram of the digital image processing system	61
3.4 Block diagram of the Feedback Processor	62
3.5 Power spectral density vs. wavenumber of fringe image. ____; Horizontal spectrum,.....; Vertical spectrum	63
3.6 Schematic diagram of the line averaging technique	64
3.7 Photograph of line averaged image for fringe image in Figure 3.2	65
3.8 Power spectral density vs. wavenumber of the line averaged image. ____; Horizontal spectrum,.....; Vertical spectrum	66
3.9 Photograph of image after background subtraction	67
3.10 Power spectral density vs. wavenumber of image after background subtraction. ____; Horizontal spectrum,.....; Vertical spectrum	68

3.11	Photograph of image after contrast enhancement	69
3.12	Power spectral density vs. wavenumber of image after contrast enhancement. _____; Horizontal spectrum,.....; Vertical spectrum	70
3.13	Autocorrelation vs. offset for image after contrast enhancement _____; Horizontal autocorrelation, .....; Vertical autocorrelation	71
3.14	Fringe spacing error as a function of initial expected fringe angle	72
3.15	Fringe direction error as a function of initial expected fringe angle	73
3.16	Flow chart of digital image processing program	74
3.17	Vector plot of the velocity field measured in the rotating disk experiment	75
3.18	Schematic diagram of CVL free surface imaging system	76
3.19	Photograph of the microballoons	77
3.20	Fringe image obtained with the surface imaging optical system	78
3.21	Vector plot of the velocity field at the free surface	79
3.22	Contour plot of the vorticity at free surface derived from the results plotted in Figure 3.21	80
3.23	Schematic diagram of CVL shadowgraph system used to obtain the speckle photographs	81
4.1	Velocity trace measured on the centerline at $X/D_0 = 5$ for $\Gamma = 64 \text{ cm}^2/\text{s}$	82
4.2	Measured vortex ring position as a function of time for several generator operating conditions	83
4.3	Measured Reynolds number as a function of nondimensional downstream position for several generator operating conditions	84
4.4	Measured Reynolds number after vortex ring formation vs. measured Reynolds number at the exit	85
4.5	Circulation ratio as a function of slug length	86
4.6	Sequence of photographs showing simultaneous views of the vortex ring evolution: (a) $\Gamma_0/a^2=5$ , (b) $\Gamma_0/a^2=13$ , (c) $\Gamma_0/a^2=20$ , (d) $\Gamma_0/a^2=25$	87
4.7	Effect of depth on the extent of interaction for vortex rings formed at an incidence angle $\alpha = 0^\circ$ ; Contaminated surface	88
4.8	Downstream location of vortex cores as a function of time for the contaminated surface	89

4.9	Distance of vortex core to the free surface and at the surface as a function of time for the contaminated surface	90
4.10	Effect of depth on the extent of interaction for vortex rings formed at an incidence angle $\alpha = 0^\circ$ ; Clean surface	91
4.11	Sequence of photographs showing the interaction of vortex ring with free surface at an incidence angle $\alpha = 90^\circ$ : (a) Contaminated surface, (b) Cleaner surface	92
4.12	Trajectory of vortex core for the contaminated free surface. ( $\alpha = 90^\circ$ )	94
4.13	Trajectory of vortex core for the cleaner free surface. ( $\alpha = 90^\circ$ )	95
4.14	Nondimensional reconnection time as a function of Reynolds number for several incidence angles $\alpha$ and depth $h/D_0$ .	96
4.15	Cross-section view photograph of vortex ring before interaction with free surface. $\Gamma/v = 5000$ , $\alpha = 20^\circ$ .	97
4.16	Sequence of photographs showing the interaction of a vortex ring with free surface. Top image; Shadow image of surface deformation. Bottom image; Cross section view. $\Gamma/v = 5000$ , $\alpha = 20^\circ$ .	98
4.17	Position of vortex cores in cross-section view as a function of time, $\Gamma/v = 5000$ , $\alpha = 20^\circ$ .	105
4.18	Trajectory of vortex core on the free surface $\Gamma/v = 5000$ , $\alpha = 20^\circ$ .	106
4.19	Sequence of speckle photographs of double reconnection by interaction of a vortex ring with a free surface, $\Gamma/v = 5000$ , $\alpha = 20^\circ$ .	107
4.20	Vector plot of free surface velocity field obtained from speckle photographs in Figure 4.19	113
4.21	Sequence of vector plot and contour plot of free surface strain field obtained from velocity measurements in Figure 4.20. (A) Vector plot of $\epsilon_{11}, \epsilon_{22}$ (B) Contour plot of $\epsilon_{zz}$	119
A.1	Schematic diagram of a small jet tank vortex ring generation facility	127

## NOMENCLATURE

Symbol	Description
$a$	vortex ring diameter
$d$	displacement of tracer particles
$d_f$	fringe spacing
$d_m$	measured fringe spacing
$D$	distance between vortex cores at the free surface
$D_o$	nozzle exit diameter
$f_T$	focal length of Fourier transform lens
$h$	depth of nozzle exit centerline below the surface
$L$	downstream distance from the interaction point to the nozzle exit
$L_o$	slug length
$M$	magnification of the imaging system
$R$	normalized autocorrelation value
$R_o$	initial vortex ring radius
$u$	velocity component of the cartesian coordinate on the free surface
$v$	velocity component of the cartesian coordinate on the free surface
$w$	velocity component of the cartesian coordinate on the free surface
$U_t$	vortex ring propagation velocity
$x$	cartesian coordinate on the free surface in the downstream direction
$y$	cartesian coordinate on the free surface in the downstream direction
$z$	cartesian coordinate on the free surface in the downstream direction

$X$	downstream distance from vortex core to nozzle exit
$Y$	distance from vortex core to the free surface
$\alpha$	incidence angle
$\alpha_f$	fringe orientation angle
$\alpha_m$	measured fringe orientation angle
$\alpha_s$	initial fringe expected angle
$\delta$	core size diameter of vortex ring
$\Delta t$	time between exposures
$\Gamma$	measured circulation at a downstream location
$\Gamma_0$	circulation at the nozzle exit
$\nu$	kinematic viscosity of fluid
$\omega$	vorticity
$\lambda$	wavelength of the laser

## CHAPTER I

### INTRODUCTION

There is considerable interest on the interaction of turbulent shear flow with a free surface. An important aspect of these problems is the characterization of the interaction of the free surface with underwater vorticity associated with the large scale vortical structures in the turbulent flow. A flow visualization study of the interaction of a turbulent axisymmetric jet with a free surface by Bernal and Madnia (1988, 1989) showed a complex pattern of surface waves and surface motions caused by the vortical motions in the jet flow. Distinct dark spots were observed in shadowgraph flow visualization images of the interaction region. These dark spots are associated with vortex lines terminating at the free surface (Berry and Hajnal, 1983, Sterling et al. 1987). Sarpkaya and Henderson (1985) studied the surface signature of trailing vortices generated by a delta wing. They observed the formation of surface scars (features organized along the direction of the wing motion) and striations (features with general orientation perpendicular to the wing motion) on the surface associated with the vortex motion. Dark spots indicating vortex lines terminating at the free surface were observed along the scars. Also when the trailing vortices underwent Crow instability (Crow, 1970) they observed the formation of crude vortex rings with vortex lines terminating at the free surface. An important consideration in the underwater jet and underwater delta wing wake problems is that all the vorticity in the flow is introduced underwater. As the flow evolves vorticity finds its way to the free surface. The flow process responsible for the advection of vorticity to the free surface and generation of vorticity normal to the surface are not understood. The present study of the interaction of an

axisymmetric laminar vortex ring with the free surface was undertaken to gain some insight into these flow processes. The vortex ring is one of the simplest flow configurations in which these processes can be investigated in a fully three-dimensional flow.

A schematic diagram of the flow geometry with definition of parameters is shown in Figure 1.1. The vortex ring is characterized by the circulation,  $\Gamma$ , the ring diameter,  $a$ , and the core size,  $\delta$ . The effect of vorticity distribution within the ring on the speed of propagation has been discussed by Lamb (1945), Saffman (1970) and Widnall and Sullivan (1973) among others. These parameters are determined by the formation process. The effect of various parameters in the formation process on the circulation, diameter, speed of propagation and stability of vortex ring has been investigated by Saffman (1975), Maxworthy (1972,1977), Widnall and Sullivan (1973), Didden (1977,1979) and Glezer (1988) over a wide range of the Reynolds number. It seems reasonable to expect that these vortex ring parameters will influence the interaction with the free surface.

Cerra and Smith (1983) report a limited number of observations in the case of a vortex ring impacting normal to the free surface. They compare these results with the results of similar experiments in which the free surface is replaced by a solid surface. They found that the evolution of the flow in both cases is very similar. This evolution is characterized by generation of opposite sign vorticity at the surface which subsequently rolls-up into secondary and even tertiary vortex rings. The mechanisms of vorticity generation at the surface is not identified although they attribute this behavior to surface tension effects. It should be noted that in Cerra and Smith experiments the Froude number was small. Dahm et al.(1989) investigated the interaction of a vortex ring with a density interface at normal incidence. They identify the proper scaling parameters and show that in the limit of strong interface or weak vortex the deformation of the interface is small yet substantial opposite sign vorticity is generated by baroclinic effects. They also show striking similarity of this limit case with the solid wall case. The interaction of vortex pairs

with the free surface at normal incidence was investigated by Barker and Crow (1977) and more recently by Willmarth et al (1989) at high Froude numbers.

There is no information on the nature of the interaction of a vortex ring with a free surface at incidence angles other than normal incidence. Sarpkaya and Henderson (1985) proposed that vortex lines terminating at the surface are generated by a process similar to the vortex linking observed in the Crow instability (Sarpkaya, 1983). The basis for this argument is that in the case of small Froude number, the free surface can be approximated by a flat nondeformable surface or equivalently a symmetry plane. Thus, in this limit the flow field can be expected to be similar to the flow encountered when two vortex lines interact across a symmetry plane. For vortex rings this type of interaction has been investigated by several authors including: Kambe and Takao (1971), Fohl and Turner (1975), Oshima and Asaka (1977), Schatzle (1987) and Oshima and Izutsu (1988).

One striking phenomenon encountered in these interactions is the vortex reconnection process found when the vortex rings come in contact along intersecting paths. Vortex lines in the incoming rings forming two separate closed loops disconnect and reconnect to form a single closed loop. Under certain conditions, as the reconnected vortex lines move apart, two parts of the distorted vortex lines come into contact again resulting in a second reconnection process and the formation of two vortex rings moving along diverging paths on a plane perpendicular to the initial incidence plane. This interaction process is referred to as a double reconnection. The double reconnection process was first reported by Kambe and Takao (1971) who used smoke flow visualization of vortex rings in air propagating parallel to each other. Double reconnection was found to occur for a narrow range of vortex ring circulations. Fohl and Turner (1975) studied the collision of two identical rings directed toward one another along intersecting axes in water. They found a critical incidence angle for the double reconnection process to occur. This critical incidence angle was attributed to a resonance effect and they showed experimental results for one value of the Reynolds number. A systematic study of the effect of the initial speed

of vortex rings and distance between rings on the interaction of rings moving side by side in air was conducted by Oshima and Asaka (1977). Depending on the initial speed, they classified the interactions into three typical patterns, single reconnection, double reconnection and multiple reconnection. Oshima and Izutsu (1988), and Schatzle (1987) have measured the velocity field during the interaction of colliding vortex rings. Oshima and Izutsu report experimental results of the time dependent vorticity field on two orthogonal planes using x-type hot wires for two vortex rings moving side by side in air. They conclude that each filament in the vortex tubes individually reconnects and moves away quickly in the direction normal to the plane of the filament due to its strong curvature. Schatzle studies the reconnection process by measuring the velocity field on the symmetry plane with a laser-Doppler velocimeter for two vortex rings colliding at a shallow angle in water. He argues the reconnection process results from vorticity cancellation due to the production of out-of-plane strain.

It is apparent that velocity field information is necessary to properly understand these complex vortical interactions. Laser speckle velocimetry (LSV) or laser speckle photography (LSP) is a non-invasive velocity measurement technique capable of measuring the flow field in a planar section at an instant. Stetson (1975), Vest (1979) and Laureborn and Vogel (1984) described this technique in detail. Also Dudderar et al (1986) published an excellent review of the development of laser speckle velocimetry. Barker and Fournay (1977), Grousson and Mallick (1977) and Dudderar and Simpkins (1977) published almost simultaneously successful demonstrations of LSV for Poiseuille flow. From that time, many researchers have been interested in the LSV technique, but manual determination of the velocity required lots of time and lacked accuracy. Meynart (1982,1983) developed the digital image technique to analyze the data. Adrian (1984) and Adrian and Yao (1985) distinguished between the terms 'speckle velocimetry' and 'particle image velocimetry' depending on the seeding density and discussed the optimum tracer particle size. An important limitation of this technique is that it has a  $180^\circ$  ambiguity in the direction of the

measured velocity vector. Lourenco et al (1986) and Adrian (1986) have used image shifting techniques to resolve the directional ambiguity and to increase the velocity dynamic range. The role of photographic parameters in speckle technique are reported by Lourenco and Krothapalli (1987).

In the present study, the interaction of a vortex ring with a free surface is investigated. Experiments were conducted at several vortex ring generation conditions and incidence angles. The effect of surface contamination was also explored. The conditions resulting in the double reconnection process were determined and the flow field of the surface was measured using LSP. In Chapter 2, the experimental apparatus and instrumentation are described. The details of laser speckle photography as implemented in this investigation and the automatic digital image processing technique used are discussed in Chapter 3. The results of the experiments for the various incidence angles and the detail flow field measurements are presented and discussed in Chapter 4. A summary of the main results and conclusions of the investigation is given in Chapter 5.

## CHAPTER II

### FLOW FACILITY AND INSTRUMENTATION

#### 2.1 The Facility

The experiments were conducted in the flow facility shown schematically in Figure 2.1. The facility consists of a free surface water tank and a vortex generator assembly. The free surface water tank is made of glass 76.2cm wide, 76.2cm high and 167.6cm long. The tank was filled with Ann Arbor city water filtered through a 5  $\mu$ m sediment removal filter.

Preliminary experiments showed large sensitivity of the interaction process to the presence of surface active agents in the water as discussed in Section 4.2. Several facility elements were designed and incorporated to minimize the amount of surface active agents in the water. As shown in Figure 2.1, the entire facility was covered with plastic sheet to prevent dust particles and other contaminants from settling on the water surface. Also a stand-up pipe connected to the drain was used to control the water level in the tank. Fine adjustment of the vortex generator depth was obtained by small adjustments of the length of the pipe. To insure a clean surface a continuous flow of water was allowed into the tank which was removed through the stand-up pipe. This technique preferentially removes water from the free surface removing with it the surface active material before it can accumulate.

The continuous flow of water was set up at least one day before the experiments were conducted and throughout the duration of the experiments. This flow was interrupted only a few minutes before the generation of each vortex ring to allow any current in the tank to die out. Under these conditions the water temperature in the tank was maintained at

8.5° C  $\pm$  0.2° C for the duration of the experiments. The surface tension of water in the tank was measured using the capillary tube technique. Typical values measured when these procedures were followed were in the range 71 - 73 dynes/cm which are within 5% of the value for pure water at that temperature.

## 2.2 Vortex Generator

A photograph of the vortex generator used in the investigation is shown in Figure 2.2. As shown in Figure 2.3, the vortex generator consisted of a inlet flow diverter (0.3 cm thick and 5 cm in diameter), a foam section (2.5 cm thick), a honeycomb section (3.8 cm long and 0.4 cm in diameter) and a contraction section. The contraction section consisted of a circular-arc shaped nozzle (17.8 cm radius) with a contraction ratio of 16 to 1. The exit orifice had circular cross-section 2.54 cm in diameter.

The vortex generator was mounted on a support bar which in turn was mounted on a unistrut structure affixed to the top of the tank, as shown in Figure 2.4. The vortex generator coarse depth adjustment was provided by the depth adjustment bar. The vortex ring incidence angle,  $\alpha$ , was adjusted by rotating the vortex generator around a pivot point at the end of the depth adjustment bar. A threaded hole and lock nut were used to secure the vortex generator at the desired angle.

The flow system used to generate the vortex rings is also shown in Figure 2.4. This system consists of a pressurized water reservoir, a solenoid valve and associated control components. In a typical operation water in the reservoir tank is pressurized with shop air using the pressure regulator. The vortex ring is generated by opening the solenoid valve for a short time. The parameters that control the circulation strength of the resulting vortex ring are the reservoir pressure, the water needle valve setting and the solenoid valve open time duration. A submersible solenoid valve (ASCO 8031B43, 4 psi pressure, 1.9 cm orifice size) was mounted just behind the vortex generator (see Figure 2.2) to reduce oscillation

after the solenoid valve was closed. A stainless-steel reservoir, 10 cm in diameter by 42 cm long, was connected to the solenoid valve through the needle valve (1.27 cm orifice) and a flexible tube for setting the arbitrary angle of the vortex generator. The pressurized air was supplied to the reservoir through the pressure regulator and needle valve which were mounted on the top of the reservoir. The reservoir and vortex generator were filled with water supplied through the top of the reservoir, or by the suction of the air inside the reservoir through the shut-off valve. To eliminate air bubbles inside the vortex generator, water was warmed up to room temperature and used to fill the vortex generator in a vertical position. The temperature of the water inside the generator was allowed to equilibrate with the water temperature in the free surface tank by running tap water continuously in the tank through the night with a rubber plug at the exit orifice of the vortex generator.

The solenoid valve opening time was controlled by the timing circuit shown in Figure 2.5. It consists of a timer chip and a solid-state relay to energize the valve. Additional timing components were used as shown in Figure 2.5 to synchronize the generation of the vortex ring with other equipment used for flow visualization as described below.

### 2.3 Flow Visualization

Several flow visualization techniques were used in this investigation. Simultaneous flow visualization of the free surface and of the cross-section of the vortex ring were obtained using the system shown schematically in Figure 2.6. The surface deformation induced by the vortex ring was visualized using a shadowgraph technique. A collimated beam was formed by positioning a mercury arc lamp at the focal point of a 300 mm diameter  $f/5$  spherical mirror. The collimated beam was directed perpendicular to the undisturbed free surface by means of a 30 cm x 30 cm first surface flat mirror. The refracted pattern caused by deformation of the free surface was viewed on a screen

positioned at an angle of  $45^\circ$  with respect to the free surface. Simultaneous visualization of the cross-section of the vortex rings was obtained by adding a fluorescent dye (Rhodamine 6G) at a concentration of 3 ppm to the water in the vortex generator. The flow was illuminated with a laser light sheet. The sheet was formed from the green (514 nm) line of an Argon-Ion laser by means of a collimator and a cylindrical lens (15 cm in focal length). The sheet was positioned along the symmetry plane of the ring perpendicular to the free surface. The thickness of the sheet in the region of interest was approximately 1 mm. Both the vortex ring cross section and surface deformation were simultaneously recorded on the same photographic film or video image.

Experiments using the simultaneous visualization of the cross-section view and free surface deformation (See Section 4.2.1.1) showed that both images could not be simultaneously focused on the film. While slightly out of focus images could be tolerated in the relatively lower resolution video images, it was not acceptable for higher resolution photographic work. A better quality image of the free surface deformation was obtained separately using the imaged shadowgraph system shown schematically in Figure 2.7. In addition to the set up for shadowgraph technique, another first surface flat mirror was installed on top of the free surface tank to direct the beam into another 300 mm in diameter f/5 spherical mirror and a lens located at the focal point of the spherical mirror. This lens focused the shadow image formed 43 cm above the free surface on the film plane. Different magnifications of the image were obtained using different focal length lenses.

The photographs of the vortex ring cross section were obtained using a Nikon 35 mm camera equipped with a motor drive controlled by the timing circuit shown in Figure 2.5. The solenoid valve and motor drive timers were triggered at the same time. The motor drive adjustable timer setting determines the time delay between the formation of the vortex ring and the instant at which the picture was obtained. A 135 mm f/2.8 lens was used with a 31 mm extension ring to provide proper magnification. The camera was located close to the tank to capture the whole evolution of vortex ring during the interaction with the free

surface. The photographs of the free surface deformation using the imaged shadowgraph system were obtained using the same camera body with a lens as indicated above.

#### 2.4 Hot Film Velocity Measurement

Hot film velocity measurements were conducted to determine the circulation strength of the vortex ring and the formation characteristics of the vortices. A constant temperature hot film anemometer with a standard TSI quartz coated cylindrical sensor was used. The sensor frequency response is specified by the manufacturer as 80 KHz. The sensor axis was positioned perpendicular to the exit orifice along the centerline. A block diagram of the electronics and data acquisition system is shown in Figure 2.8. A constant temperature anemometer circuit (TSI model 1750) was connected to the decade resistance box (TSI model 1056) with a resolution of  $0.01\Omega$ . The output of the anemometer was DC shifted and amplified using a Tektronix AM 501 operational amplifier. To digitize the output of the differential amplifier, a LeCroy Model 8210 Transient Digitizer was used at a sampling rate of 1KHz. The hot film probe was mounted on a computer controlled traverse mechanism (Willmarth, 1977). A Transicoil Model U-217094 Gearhead Stepper Motor was used to move the probe.

The probe calibration was performed using the vortex generator and the same free surface tank facility. The probe was located at the vortex generator exit and the exit velocity was determined by measuring the time required to discharge a fixed volume out of the reservoir. The vortex generator exit velocity was varied by changing the reservoir pressure. For each vortex generator exit velocity, the output voltage from the amplifier was recorded. A calibration curve was obtained by a fourth order polynomial fit to the measured data. The estimated error of the calibration curve is 1.7% of the maximum exit velocity. To minimize drift of the velocity signal, the water temperature was maintained within  $0.2^\circ\text{C}$  during the

calibration and the experiment. Also the water was passed through a softener filter in addition to the 5  $\mu\text{m}$  sediment removal filter.

## CHAPTER III

### FREE SURFACE VELOCITY FIELD MEASUREMENT

#### 3.1 General Consideration

In these experiments the free surface velocity field was measured using Laser Speckle Photography. The fundamental concept is to record on the same photographic plate two time-displaced images of the flow. The flow, in this case the free surface, is seeded with small tracer particles. The fluid velocity component on a plane parallel to the photographic plate is determined from the displacement of the tracer particles during the time between exposures. The implementation of the technique can be divided into three separate steps: (1) Photographic Recording, (2) Flow Image Analysis and (3) Velocity Field Analysis. While these three steps are interrelated from the point of view of accuracy, resolution and overall efficiency of the technique, they represent three physically different procedures using different equipment which are better discussed separately. After a brief description below, step (2) is discussed in detail in Section 3.2, step (3) is discussed in Section 3.3 and step (1) is discussed in Section 3.4.

In step (1) a photographic image of the flow seeded with particles is obtained. The details of the technique used for the free surface velocity measurement are described in Section 3.4. Test images were also obtained and used for development and calibration of the software used in steps (2) and (3). For this purpose specklegrams were obtained using the rotating disk set up shown in Figure 3.1. A lucite disk mounted on a dc motor was rotated at an angular velocity of 1000 rpm. A pulsed ruby laser with a typical exposure time

of 20 ns was used to illuminate the disk. Double exposures were obtained with a time between exposure of 60  $\mu$ s. The resulting speckle patterns were recorded on a holographic plate, AGFA-Gevaert 10E75, which has a resolving power of better than 3000 lines/mm.

In step (2) the displacement of the particles is measured by directing a narrow collimated beam of coherent light, typically an unexpanded He-Ne laser beam, through the photographic plate at the point of interest. Young's fringes are formed by interference of the diffraction patterns of the displaced speckles and/or particle images on the film. These interference fringes are aligned perpendicular to the direction of the surface displacement. The fringe image formed at the back focal plane of a lens were analyzed using a digital image analysis system. The displacement of the particles between exposures,  $d$ , is related to the fringe spacing,  $d_f$ , by the equation

$$d = \frac{\lambda f_T}{M d_f} \quad (3.1)$$

where  $\lambda$  is the wavelength of the laser used to form the fringes,  $f_T$  is the focal length of the transforming lens and  $M$  is the magnification of the imaging system used to take the photograph. Then the local flow velocity is given by the relation

$$u = \frac{d}{\Delta t} \quad (3.2)$$

where  $\Delta t$  is the time between exposures.

A typical fringe image is shown in Figure 3.2. Because the fringe image is formed by coherent light a random speckle pattern is superposed on the fringes. The characteristic scale of this speckle pattern is determined by the interrogation beam diameter. It is apparent that the Young's fringes will not form if the particle displacement on the photographic plate is larger than the interrogation beam diameter. In the present system this limitation implies that as the flow displacement increases the fringe spacing decreases until it becomes of the

order of the speckle size and can no longer be measured. The technique is also limited by the fact that the fringe spacing can not be measured when it is comparable to the size of the diffraction halo around the interrogation beam. This limit corresponds to the displacement of the particles on the film being small compared to the resolution of the imaging system since it is these small features on the photographic plate that determine the size of the diffraction halo. An important limitation of the technique is that there is a  $180^\circ$  ambiguity in the direction of the measured velocity vector. A velocity bias technique can resolve this ambiguity (Lourenco et al (1986) and Adrian (1986)) and also improve the dynamic range of the technique. In the present measurements velocity bias was not used. The direction of the velocity vector was determined from global analysis of the flow field. The velocity field was measured over the region of interest by successively scanning the photograph and measuring the fringe spacing and orientation on a point by point basis.

Finally in step (3), the measured velocity vector field is analyzed to determine relevant properties like the component of the vorticity vector normal to the plane of the measurement and the deformation rate tensor components on the plane of the measurement.

## **3.2 Fringe Image Analysis**

### **3.2.1 Image Processing System**

The fringe spacing and direction on the fringe image were measured using a high speed Digital Image Processing System. A schematic diagram of the Image Processing System is shown in Figure 3.3. A CW He-Ne laser (Jodon Inc. Model # HN-10G) is used to interrogate the flow image at a point. The fringe image is formed in the back focal plane of a Fourier transform lens. A beam stop was positioned at the center of the fringe image to block the bright spot due to the undiffracted light. A host computer (ZEOS 286) controls the image processor and a two component traverse system (Newport Corp. Model 855c Programmable Controller and Model 850-series Actuators). A video camera (DAGE-MTI

Inc. Model 65) is used to digitize the fringe image into a 512x512 pixel array with 8 bits density resolution for a total of 1/4 Megabyte. The resulting digital image is stored and analyzed in a Gould FD5000 Image Processing System. The FD5000 contains two channels of image memory. Each channel is divided into four 512x512 pixel banks. Each pixel is stored in memory as a 16 bit value. The upper 8 bits of each pixel are used for graphic overlays or additional image memory. The lower 8 bits give the image density in the range from 0, dark, to 255, white. A real time Feedback Processor (FBP) is the main component in the FD5000. The layout of the FBP is shown in Figure 3.4. The input to the FBP is selected from one of the image memories or a predefined constant. The input data can be modified using a lookup table (LUT). The LUT's are loaded from the computer and replace each input value with a corresponding value in the table. Data is combined in the arithmetic logic unit (ALU) which performs simple arithmetic and logic functions. Data is then sent to an image memory directly or by way of an output LUT. The accumulator can be used to sum the intensities of pixels over the entire image. The image input to the FBP can be modified by the zoom/scroll device. This device controls a window on the image memory and can move the window over the image memory. In addition, the FD5000 has a cursor device and trackball which allow the user to select points on the image.

### 3.2.2 Image Enhancement

As shown by Figure 3.2, the fringes on the fringe image appear superposed on a speckle pattern. From the point of view of measuring the fringe spacing this speckle pattern is noise and must be removed. An image analysis technique was developed to filter the speckle noise. It is convenient to describe this technique on the basis of the spectral content of the fringe image. The power spectral density (PSD) along the horizontal (x axis) and vertical axis (y axis) were obtained using a modified Welch method (Welch, 1967). For the PSD along the horizontal direction, the whole image was first sectioned into 512 segments of 512 pixels length along the horizontal direction. Each segment corresponds to a

horizontal line of this image. A modified periodogram for each segment was computed using the Fast Fourier Transform algorithm. Then the spectral estimate was calculated from the average of these 512 periodograms. The PSD along the vertical direction was also obtained using the same method. In this case each segment corresponds to a vertical line of the image. The measured horizontal and vertical PSDs for the fringe image in Figure 3.2 are shown in Figure 3.5. Throughout this discussion the PSD curves are normalized for unit area under the curve. The PSD curves show the main features of the fringe image that must be considered in the analysis. First, there is considerable energy at low wavenumbers which corresponds to background nonuniformity on the original image. Second, on each PSD there is a distinct spike which corresponds to the fringe pattern. Third, there is significant broadband noise associated with the random speckle pattern. It is the objective of the image enhancement technique to isolate the second feature, the fringe pattern, from the other two which are measurement noise.

To eliminate the random speckle noise while retaining the fringe pattern, the image was averaged along the expected fringe direction characterized by a direction angle  $\alpha_s$ . The direction of the averaging was set manually using two cursors on the TV monitor and the trackball. Figure 3.6 shows the scheme for line averaging. The image was shifted along the desired direction using the scroll device in the FD5000 and stored in another channel. Corresponding pixels on the original image and the shifted image were added and the result divided by two using the FBP. The process was repeated  $N$  times. For each successive iteration the magnitude of the image shift was increased by a factor of 2. Using this scheme an average length of  $2^N$  pixels was implemented with only order  $N$  operations. A photograph of the resulting line averaged image for  $N=5$  is shown in Figure 3.7. The corresponding PSDs are shown in Figure 3.8. Both the line averaged image and the PSD results show that the speckle noise was successfully removed while the fringes were retained. This image is still contaminated with considerable background nonuniformity.

To eliminate the background nonuniformity the original fringe image was low-pass filtered and the resulting background image was subtracted from the line averaged image. The low-pass filter was implemented using an equal weight square window of  $2^N \times 2^N$  pixels. The same averaging scheme used for the line average was utilized which results in  $2^N$  operations. A value of  $N=5$  was found adequate to generate a good background image. A photograph of the image after background subtraction is shown in Figure 3.9 and the results for the corresponding PSDs are shown in Figure 3.10. This image and the PSD show that the background nonuniformity was removed. The spikes in the PSD associated with the fringes are more pronounced in this image with a signal to noise ratio of the order of 100. The width of these spikes however is relatively large. To further sharpen the spikes contrast enhancement was applied to this image. Intensity levels below 120 were set to 0 and above 140 were set to 255. Intensity levels between 120 and 140 were redistributed linearly from 0 to 255. This process increased the visibility of the fringes by sharpening the intensity transitions associated with the fringes. A photograph of the contrast enhanced image is shown in Figure 3.11. The corresponding PSDs are shown in Figure 3.12. This image is now ready for analysis by the autocorrelation technique described below. The width of the spikes in the PSD is of the order of the resolution ( $1/512$  cycles/pixel) of the measurements. This implies that the spatial frequency of the fringes can only be determined within that uncertainty. This corresponds to an uncertainty of the fringe spacing measurement of the order of 20% for the case shown in Figure 3.12. The autocorrelation technique described below was developed to reduce this uncertainty to less than 1%.

### 3.2.3 Autocorrelation Technique

The fringe spacing and orientation were determined from the autocorrelation function of the intensity distribution on the contrast enhanced image along two perpendicular axes. The normalized autocorrelation along each axis was computed from the relation

$$R(\Delta x) = \frac{\frac{1}{L} \int_0^L (I(x) - \bar{I}) (I(x + \Delta x) - \bar{I}_1) dx}{\left( \frac{1}{L} \int_0^L (I(x) - \bar{I})^2 dx \right)^{1/2} \left( \frac{1}{L} \int_0^L (I(x + \Delta x) - \bar{I}_1)^2 dx \right)^{1/2}} \quad (3.3)$$

$$\bar{I} = \frac{1}{L} \int_0^L I(x) dx \quad (3.4)$$

$$\bar{I}_1 = \frac{1}{L} \int_0^L I(x + \Delta x) dx \quad (3.5)$$

where  $L = 200$  pixels. Typical autocorrelation results along two perpendicular axes are shown in Figure 3.13. The first zero crossing in this figure occurs at one fourth of the fringe spacing. Subsequent zero crossings are spaced by one half of the fringe spacing. It should be noted that the amplitude of the fluctuation of the correlation function is large for offsets of the order of 200 pixels (almost half image). This is a direct consequence of improved visibility of the fringes in the contrast enhanced image (Figure 3.11).

The orientation of the fringes,  $\alpha_f$ , was determined by measurement of the fringe spacing along two perpendicular directions. The accuracy of the orientation measurement is improved by selecting the two axes as follows. If the expected fringe angle,  $\alpha_s$ , was within  $-3/8 \pi < \alpha_s < -\pi/8$  or  $\pi/8 < \alpha_s < 3\pi/8$ , then axes parallel to the  $x$  axis and the  $y$  axis were used. If  $\alpha_s$  was in the region as  $-\pi/2 < \alpha_s < -3\pi/8$  or  $-\pi/8 < \alpha_s < \pi/8$  or  $3\pi/8 < \alpha_s < \pi/2$ , then axes oriented at  $45^\circ$  and  $-45^\circ$  with respect to  $x$  axis were chosen. This choice insures that the fringe direction is not parallel to one of the measurement directions.

The fringe spacing along each direction was determined from the first and last zero-crossings of the autocorrelation function within a 200 pixel window. These zero-crossings were determined directly using an efficient algorithm (number of operations  $\approx \log_2$

(offset)). From the location of the first zero crossing  $z_i$  and final zero crossing  $z_f$ , the fringe spacing was determined as

$$d_f = 2 \left[ \frac{z_f}{k + 1/2} \right] \quad (3.6)$$

$$k = \text{Int} \left[ \frac{z_f - z_i}{2 z_i} \right] \quad (3.7)$$

where  $k$  is the number of half cycles of the autocorrelation function between  $z_i$  and  $z_f$ . The value of  $k$  was verified since it must be even for a negative slope of the autocorrelation function at  $z_f$  and odd for a positive slope of the autocorrelation function at  $z_f$ . The uncertainty on the  $d_f$  measurement is determined by the uncertainty on  $z_f$  which is  $\pm 0.5$  pixels. Since  $z_f$  is of the order of 200 pixels. The relative error in  $d_f$  is less than 1%.

### 3.2.4 Sensitivity Study

An important possible limitation of this technique is that it requires an input parameter namely the expected fringe direction  $\alpha_s$ . A sensitivity study was conducted to determine the variation of measured fringe spacing and measured fringe direction as a function of the expected fringe direction. The results for the fringe spacing and fringe direction are shown in Figure 3.14 and Figure 3.15 respectively for a typical image. The expected fringe angle was varied over a range of  $\pm 5^\circ$ . The measured fringe spacing  $d_m$  is within 1% of the actual fringe spacing  $d_f$ . The measured fringe angle  $\alpha_m$  is within  $\pm 0.4^\circ$  ( $\pm 0.01$  rad) of the fringe angle  $\alpha_f$ . The results suggest that if the change of fringe direction between two consecutive points measured on the same flow image is small (within  $5^\circ$ ), the value of the fringe direction measured at the previous point can be used as the expected

fringe angle for the present point. In this case, the expected fringe direction angle was needed only for the first point. The entire flow image can be analyzed without operator interaction.

### 3.2.5 Implementation

A computer program was developed to implement the flow field velocity measurement using this technique. A flow chart for this program is given in Figure 3.16. The program runs in the host computer, see Figure 3.3 and interacts with the Image Processing System. This program automatically scans the flow image with the traverse system. It can operate in automatic mode and manual mode. In automatic mode there is no operator interaction after the initial set up. In manual mode the expected fringe direction at each point must be entered by the operator. To help this process the fringe direction of the previous point is displayed on the current point fringe image. The results of the measurements along with the position information are stored on disk files for subsequent plotting and analysis.

The specklegram obtained in the rotating disk experiment was analyzed with this program operated in automatic mode. The velocity vector was measured in a square matrix of  $32 \times 32$  points spaced 1 mm, for a total of 1024 measurement points. The elapsed time required for the measurement was 6 seconds/point. A significant amount of this time (2.5 seconds/point) was spent traversing the specklegram. The elapsed time per point is larger in manual mode because of the time required to input the expected fringe angle.

### 3.3 Velocity Field Analysis

Several flow properties including the vorticity field and several components of the deformation rate tensor can be calculated from these data. Before calculating these other

properties a vector plot of the velocity field was obtained. Figure 3.17 is the vector plot of the velocity field in the rotating disk experiment. The data was measured in a square region on the disk 31 mm x 31 mm. The accuracy of data throughout this region is better than 1%. Because the disk is in solid body rotation these data can also be used to estimate the errors associated with the determination of the vorticity and deformation rate fields.

The component of the vorticity vector normal to the plane of the measurement,  $\omega$ , was determined using the relation

$$\omega = \frac{1}{A} \oint \vec{u} \cdot d\vec{l} \quad (3.8)$$

where  $A$  is the area of a surface element around the point of interest and the integral represents the circulation around that surface element. The value of  $\omega$  at each point was calculated by considering a surface element bounded by the 8 neighboring points. The line integral along those points was evaluated using Simpson's rule. For the rotating disk experiment the disk is in solid body rotation so that the vorticity at a point equals twice the angular velocity and is uniform across the region. From the data shown in Figure 3.17 the vorticity was evaluated throughout the region. Because the vorticity is uniform in this case a statistical measure of the accuracy of the vorticity measurement is obtained from the mean and standard deviation of the values in the sample. The mean vorticity for the sample is  $\omega = 210.67 \text{ sec}^{-1}$  and the standard deviation is  $48.9 \text{ sec}^{-1}$ . The mean value is in good agreement with the expected value of  $209.44 \text{ sec}^{-1}$  derived from the angular velocity of the disk 1000 rpm. The scatter around this value is consistent with the expected uncertainty of the measurement given by the ratio of the velocity measurement uncertainty divided by the distance between measured points (i.e.  $\approx 50 \text{ sec}^{-1}$  in this case).

From the velocity field measurements the components of the deformation rate tensor,  $E_{xx}$ ,  $E_{yy}$  and  $E_{xy}$ , on the plane of the measurement can be calculated. These

components of the deformation rate tensor were calculated using a second-order central difference scheme. Thus at a point in the sample  $(x_i, y_i)$  the spatial derivatives were calculated using the expression

$$\left(\frac{\partial f}{\partial x}\right)_{i,j} = \frac{f_{i+1,j} - f_{i-1,j}}{2 \Delta x}, \quad \left(\frac{\partial f}{\partial y}\right)_{i,j} = \frac{f_{i,j+1} - f_{i,j-1}}{2 \Delta y} \quad (3.9)$$

where  $f_{i,j}$  can be either the  $u$  or  $v$  component of the velocity at the corresponding point.

The deformation or strain rate information is better expressed in terms of the directions of the principal axes and the principal strain rate values along those axes. The Jacobi method was used to determine one principal axis direction with respect to the  $x$  axis  $\theta$  as

$$\tan \theta = \frac{\pm 2 \epsilon_{xy}}{|\epsilon_{xx} - \epsilon_{yy}| + \sqrt{(\epsilon_{xx} - \epsilon_{yy})^2 + 4 \epsilon_{xy}^2}}, \quad (3.10)$$

with the positive sign used if  $\epsilon_{xx} > \epsilon_{yy}$  and the negative sign otherwise. The magnitude of the strain rate along  $\theta$  is given by

$$\epsilon_{11} = \epsilon_{xx} \cos^2 \theta + \epsilon_{xy} \sin 2\theta + \epsilon_{yy} \sin^2 \theta. \quad (3.11)$$

Of course the other principal axis is perpendicular to the  $\theta$  direction and the corresponding magnitude of the strain rate is given by

$$\epsilon_{22} = \epsilon_{xx} \sin^2 \theta - \epsilon_{xy} \sin 2\theta + \epsilon_{yy} \cos^2 \theta. \quad (3.12)$$

In the case of the rotating disk data shown in Figure 3.17, where the disk is in solid body rotation, all components of the deformation rate tensor are zero everywhere on the disk. Again the mean and standard deviation of the computed values of  $\epsilon_{xx}$ ,  $\epsilon_{yy}$  and  $\epsilon_{xy}$  give a statistical measure of uncertainty for these parameters. The mean and standard deviation for  $\epsilon_{xx}$ ,  $\epsilon_{yy}$  and  $\epsilon_{xy}$  were evaluated for the rotating disk sample. Typical values for the mean,  $\epsilon_{xx}$ , and standard deviation,  $\epsilon_{xx}'$ , of the normal deformation rate along the x axis are  $\epsilon_{xx} = -8.56 \text{ sec}^{-1}$ ,  $\epsilon_{xx}' = 97.88 \text{ sec}^{-1}$  respectively.

These results are consistent with the expected uncertainty of the measurement.

### 3.4 Photographic Recording

The laser speckle photography technique was used to measure the velocity field at a free surface. Preliminary measurements were conducted on the region of interaction of a turbulent underwater jet with the free surface. Typical results will be discussed in this section. The technique was later applied to study the interaction of a vortex ring with the free surface. A schematic diagram of the facility and optical system is shown in Figure 3.18. For the jet experiment a small jet tank (described in Appendix A) located inside the glass tank was used to produce the jet flow. The jet centerline was located one diameter (2.54 cm) below the free surface and the jet exit velocity was 25 cm/sec. Tracer particles which followed the fluid motion at the surface were added to the free surface tank. A Copper Vapor Laser was used to illuminate the particles. The optical system was similar to the one used for the surface imaging shadowgraph flow visualization. A 53 cm focal length lens was used which resulted in a magnification of 0.4. The jet exit velocity used was kept low to minimize the free surface deformation thus reducing the refraction effects on the image.

The surface tracers used in the experiments were glass microballoons. The density of the microballoons was 0.15 g/cc and the mean diameter was approximately 45  $\mu\text{m}$ . The

concentration of microballoons at the free surface was  $5 \times 10^4 \text{ cm}^{-2}$ . A photograph of microballoons is shown in Figure 3.19. The size variation of the microballoons in this picture is typical of the samples used in the experiments. Because of the small size of the microballoons they are expected to cause very small deformations of the surface. An important consideration is the ability of tracers to stay at the free surface and follow the surface motion. The Stokes characteristic time of the microballoons in water is  $8 \mu\text{s}$  so they follow the velocity fluctuations well. The limitation of the technique as implemented in this experiment is the fact that the jet fluid was not seeded with tracer particles. Hence regions in the free surface where the fluid originated from the jet may not have been properly seeded with tracer particles and velocity measurement may not be possible there.

In order to properly expose the film a Copper Vapor Laser was programmed to produce two bursts of light each consisting of five pulses. The time between pulses in each burst was  $100 \mu\text{s}$ . The film used to obtain the flow images was high resolution photographic plate AGFA-Gevaert 10E56. The time between bursts was 5 ms. It is during this time that the significant displacement of the tracer particles occur. The value was determined from consideration of the expected flow velocity, the speckle size and the interrogation beam diameter.

A typical fringe image is shown in Figure 3.20. In addition to the Young's fringes, elliptical fringes are also observed. Because the spacing between these elliptical fringes is comparable to the Young's fringe spacing, the digital image processing program could not be used in some regions. A vector plot of the surface flow velocity field is shown in Figure 3.21. The frame area in this plot corresponds to  $2 < x/D_0 < 9$  and  $-2 < y/D_0 < 2$ , where  $y$  is the coordinate axis perpendicular to the flow direction on the plane of the free surface. At the jet centerline the surface flow velocity increases with downstream distance as a result of the interaction of the jet with the free surface. The maximum velocity measured in this region is  $15.6 \text{ cm/s}$ . In contrast the velocity away from the centerline is quite low and the minimum velocity measured here is  $0.7 \text{ cm/s}$ . The entrained flow moves in the upstream direction as

it approaches the vortical region. Also the velocity vector rotates as the fluid enters the vortical region. The component of the vorticity vector perpendicular to the free surface was evaluated from the measured velocity field using the same method applied to the rotating disk experiment. A contour plot of the vorticity is shown in Figure 3.22. The uncertainty of measurement of  $\omega D_0/U_e$  is estimated as  $\pm 0.07$ . As expected the entrained flow is by and large irrotational. Vorticity at the free surface is introduced by the interaction of the surface with the vortical flow under it. The scale of the vortical features on the free surface is of the order of the jet width. These data clearly show the importance of the large scale structure of the jet in the interaction with the free surface.

To investigate the interaction of the vortex ring with the free surface, the speckle photographs were obtained with the Copper Vapor Laser in the optical configuration shown in Figure 3.23. The vortex generator was inclined  $20^\circ$  with respect to the free surface. The depth of the center of the vortex gun exit cross section was  $h/D_0 = 1.72$  below the free surface. AGFA-Gevaert 10E56 photographic plate was positioned parallel to the free surface 1 cm above the free surface to record the specklegram. The Copper Vapor Laser was programmed to produce two bursts of light each consisting of 5 pulses synchronized with the timing circuit that operated the solenoid valve (Figure 2.5). The time between burst was set at 6 ms. The tracer particles used for this experiment were the same microballoons as used for jet interaction experiment. The surface contaminants at the free surface were removed by a continuous surface current as described above. Prior to the experiment the surface current was turned off. After the water came to rest tracer particles were deposited uniformly on the free surface by tapping a sieve which contained the particles above the region of interest. When tracer particles stopped moving, the vortex ring was generated and the speckle photograph was taken after the proper time delay. When specklegrams were processed using the digital image processing program, different focal length lenses (53.3 cm and 30.5 cm) were used depending on the displacement of the speckle patterns on the specklegram to improve the velocity dynamic range. The results are discussed in Chapter 4.

## CHAPTER IV

### RESULTS AND DISCUSSION

#### 4.1 The Characteristics of the Vortex Rings

Experiments were conducted to determine the characteristics of vortex rings obtained with the vortex generator. In these experiments the vortex rings were formed in an effectively unbounded fluid by locating the generator a long distance away from the free surface and the walls of the facility. The main parameters of interest are the propagation speed,  $U_t$ , the circulation strength,  $\Gamma$ , and the vorticity distribution within the vortex. Of these parameters the propagation speed and circulation are relatively easy to measure. The vorticity distribution on the other hand is very difficult to determine. It is convenient to introduce two parameters associated with the vorticity distribution in the ring: the vortex ring core diameter,  $a$ , and the core size,  $\delta$ , as the simplest characterization which still retains the most important dynamics of the ring.

Five experimental conditions are considered in this investigation. They were selected based on the data by Glezer (1981,1988) and after an extensive flow visualization study. In all these cases the vortex rings were laminar at formation and remained laminar over the region of interest. The various conditions are: (1) the reservoir pressure  $p=2$  psig, needle valve opening  $N=3/4$  turns and solenoid valve opening time  $T_0=0.2$  sec. (2)  $p=1.5$  psig,  $N=3/4$  turns,  $T_0=0.6$  sec. (3)  $p=4$  psig,  $N=3/4$  turns,  $T_0=0.2$  sec. (4)  $p=4$  psig,  $N=1$  turn,  $T_0=0.2$  sec. Finally, (5)  $p=4$  psig,  $N=3/4$  turns,  $T_0=0.6$  sec.

To obtain the propagation speed and circulation of the vortex ring, hot film velocity measurements were conducted at several locations along the axis of symmetry of the generator. A typical velocity time history for condition (4) is shown in Figure 4.1. The hot film probe was located 5 nozzle exit diameters from the generator exit plane. The time origin corresponds to the opening of the solenoid valve. It can be seen that the velocity is very small up to 1.7 seconds after the generation of the vortex ring. The flow velocity is maximum at 2.15 seconds after generation and then decreases. The flow velocity is effectively zero after 2.7 seconds. Similar velocity traces were obtained at several downstream locations and for the selected vortex ring generation conditions. For the purpose of determining the velocity of propagation of the vortex ring, the arrival time of ring at the probe location is defined as the time at which the velocity is maximum. A plot of the position of the vortex ring as a function of arrival time is presented in Figure 4.2. The data at each operating condition is well approximated by a straight line. A least square fit to the data was used to determine the speed of propagation of the vortices given in Table 4.1. The uncertainty of the measurement is  $\pm 3\%$ . The propagation speed was also measured from video recordings of the evolution of the vortices. The results give a slightly higher value than the one obtained by hot film measurements. This discrepancy is attributed to the uncertainty of the video system frame rate.

The circulation strength was determined from the velocity measured along the centerline using two different techniques. First, the velocity measured at the center of the exit orifice on the exit plane was used. In order to determine the circulation it is necessary to assume a uniform velocity profile at the exit except for a thin boundary layer at the wall. The circulation,  $\Gamma_o$ , is determined from the total flux of vorticity through the exit plane as

$$\Gamma_o = \int_0^{r_o} dt \int_0^{\frac{D_o}{2}} u \left( \frac{\partial u}{\partial y} \right) dy = \int_0^{r_o} \frac{U_o^2}{2} dt \quad (4.1)$$

where  $y$  is the radial coordinate measured from the wall,  $D_0/2$  is the value of  $y$  at the orifice center,  $U_0(t)$  is the velocity at the centerline and  $T_0$  is the duration of the water pulse (Note: it is assumed  $U(t) = 0$  for  $t < 0$  and  $t > T_0$ ). The values of  $\Gamma_0$  determined from the velocity traces measured at the exit plane of the vortex generator are presented in Table 4.1.

The second technique used to determine the circulation is based on the velocity traces measured downstream along the axis of the flow. At an instant the circulation of the ring is given by,

$$\Gamma = \oint \bar{\mathbf{u}} \cdot d\bar{\mathbf{l}}, \quad (4.2)$$

where the contour includes the ring axis of symmetry and is closed at infinity. If the circulation can be assumed constant as the vortex ring convects pass a fixed downstream location then

$$dl = U_t dt, \quad (4.3)$$

and therefore

$$\Gamma = U_t \int_0^{\infty} U(t) dt. \quad (4.4)$$

The values of  $\Gamma$  calculated using this expression are plotted in Figure 4.3 as a function of downstream position. These results show that the measured circulation of the ring decreases with downstream distance for cases (2) and (4) while is constant for the other two cases. In all cases  $\Gamma$  reaches a constant value further downstream. The decrease of the measured circulation with downstream distance indicates that the vortex ring generation process is not completed. Downstream of  $X/D_0 = 3$  the measured circulation is constant

which indicates a well formed vortex. The measured values of  $\Gamma/v$  after formation are given for all conditions in Table 4.1. The uncertainty of these values is estimated as 4%.

Equation 4.1 is based on the simple model of the generation process which characterizes the exhaust of fluid from the generator as a cylindrical slug of length  $L_o$  and diameter  $D_o$  (Saffman, 1975). If we define a mean velocity as

$$\overline{U_o} = \frac{1}{T_o} \int_0^{T_o} U_o(t) dt \quad (4.5)$$

where  $U_o(t)$  is assumed uniform over the orifice area, the equivalent length of the slug is

$$L_o = \int_0^{T_o} U_o(t) dt = \overline{U_o} T_o \quad (4.6)$$

Following Glezer (1981, 1988) the impulse associated with the slug is given by

$$I = \rho A \int_0^{T_o} U_o^2(t) dt = 2\rho A \Gamma_o \quad (4.7)$$

where  $A$  is the cross-section area at the exit of the generator. The nondimensional slug length  $L_o/D_o$  is an important parameter of the formation process (Glezer, 1988). The values of  $L_o/D_o$  were determined from the velocity traces at the exit. The results are given in Table 4.1.

It is apparent that the values of the circulation obtained from the velocity measured downstream differs from the values obtained for the velocity measured at the exit plane of the generator. Figure 4.4 is a plot of the normalized circulation of the well formed vortex  $\Gamma/v$  as a function of the circulation determined from the generator exit velocity  $\Gamma_o/v$ . Also plotted in this figure are the results of Didden (1977). The results at low values of  $\Gamma_o/v$  indicate an excess circulation of the well formed vortex compared to the value

determined from the velocity at the exit. Case (4) at a larger value of  $\Gamma_0/v$  shows a lower value of  $\Gamma/v$  compared to  $\Gamma_0/v$ .

This discrepancy between the values of  $\Gamma$  and  $\Gamma_0$  clearly indicates that equation 4.1 does not provide an accurate estimate of vortex ring circulation. Further the observation that at some conditions  $\Gamma > \Gamma_0$  while at other  $\Gamma_0 > \Gamma$  suggest that competing mechanisms which tend to increase or decrease the circulation of the vortex ring are at work during the formation process.

In an experimental investigation Didden (1979) showed that there are two different mechanisms which are not accounted for in the slug model. First, the velocity distribution across the exit plane is not uniform. The velocity outside the internal wall boundary layer is larger than at the centerline. This effect is very strong during the initial stages of deformation. This increased velocity is the result of streamline curvature at the exit of the nozzle. It follows that the vorticity flux is considerably larger than what could be expected from the velocity measured at the centerline. The second mechanism is the flux of vorticity associated with the boundary layer on the external surface of the generator induced by the vortex ring. This vorticity is of opposite sign compared to the vorticity in the ring and results in a reduction of the circulation of the ring. It should be noted that the first mechanism is dominant in the initial stages of formation while the second mechanism will be stronger in the later stages of formation. Thus, it can be expected that the circulation ratio  $\Gamma/\Gamma_0$  will depend on  $L_0/D_0$ . To examine the effect of  $L_0/D_0$ , the circulation ratio  $\Gamma/\Gamma_0$  is plotted in Figure 4.5 as a function of  $L_0/D_0$  for the present data and Didden's (1977) data. It is apparent that as the length of the slug is increased the circulation ratio approaches unity. These results are in agreement with Didden's data and are consistent with Didden's (1979) detailed study of the formation process.

The initial vortex ring diameter,  $a$ , was measured on video recordings of only the nozzle exit region using a zoom lens. The vortex core size,  $\delta$ , could not be measured

directly. It was computed from the measured values of  $U_t$ ,  $a$  and  $\Gamma$  using the theoretical result for a constant vorticity core (Lamb, 1932)

$$U_t = \frac{\Gamma}{2\pi a} \left\{ \ln \left( \frac{8a}{\delta} \right) - \frac{1}{4} \right\} \quad (4.8)$$

The calculated values of  $\delta$  are also given in Table 4.1.

## 4.2 Vortex Ring Interaction with Free Surface

The interaction of a vortex ring with the free surface was investigated as a function of incidence angle  $\alpha$  (See Figure 1.1). The case of the vortex ring moving parallel to the free surface ( $\alpha=0^\circ$ ) was investigated first. The initial results suggested a significant impact on the evolution of flow by the presence of surface active agents. These results as well as experiments with a cleaner surface are discussed in Section 4.2.1. The effect of surface contamination was investigated in more detail at normal incidence ( $\alpha=90^\circ$ ). These results are discussed in Section 4.2.2. The general features of the interaction at other values of  $\alpha$  are discussed in Section 4.2.3.

### 4.2.1 Vortex Ring Parallel to the Free Surface

#### 4.2.1.1 Contaminated Free Surface

Several experiments were conducted using the jet tank apparatus described in Appendix A which generated vortices propagating parallel to the free surface,  $\alpha=0^\circ$ . No special care was taken to reduce contamination of the free surface. All the experiments were conducted with the exit orifice centerline located at  $h/D_0 = 1.25$  below the free surface. The photographs of a typical evolution of the vortex ring at a Reynolds number  $\Gamma_0/\nu = 7.4 \times 10^3$  and Froude number  $\Gamma_0/(ga^3)^{1/2} = 0.41$  are shown in Figure 4.6. In these photographs

the cross-sectional view and surface deformation are simultaneously visualized (See Appendix A). Figure 4.6 (a) shows the initial evolution of the vortex ring. A small depression of the free surface is observed above the vortex ring. In Figure 4.6 (b),(c) the upper part of the vortex ring interacts with the free surface. As a result of the interaction the closed vortex lines in the ring open and are now terminated at the free surface. Figure 4.6 (d) shows that as the lower part of the vortex ring interacts with the free surface, opposite sign vorticity is generated at the surface which rolls up in a secondary vortex. The vortex core then rebounds away from the free surface.

From video recordings of the vortex ring evolution, several measurements were obtained to characterize the interaction process. The free surface influences the evolution of the vortex ring causing a small deflection of the vortex axis towards the free surface. The extent of interaction was characterized by measurement of the downstream location of the upper vortex core when the vortex ring outline first reached the free surface,  $L_U$ , and the downstream location of the lower vortex core at the point of closest proximity to the free surface,  $L_L$ . The results for  $L_U/a$  and  $L_L/a$  as a function of  $a/h$  for several Reynolds numbers are presented in Figure 4.7. While these results suggest an exponential dependence of  $L/a$  as a function of  $a/h$ , a Reynolds number effect can not be ruled out from these data. A more detailed study of this effect was conducted with a clean surface. Further discussion of this result is presented in Section 4.2.1.2.

Detailed data on the evolution of vortex rings were obtained at a Reynolds number of  $7.4 \times 10^3$  and Froude number 0.41. The normalized downstream location of the vortex ring cores as a function of nondimensional time are shown in Figure 4.8. The path of the lower vortex core can be approximated by two straight lines of different slope. The slope change occurs at a nondimensional time of 20. A least square fit to the data gives a nondimensional velocity  $U_1 a / \Gamma_0 = 0.36$  before the interaction and  $U_1 a / \Gamma_0 = 0.066$  after the interaction. The large reduction in propagation speed can be attributed to the combined

effect of the change in radius of curvature of the vortex lines as well as the clockwise vorticity generated at the free surface.

In Figure 4.9, the normalized distance of the vortex cores to the free surface,  $Y/a$ , and normalized distance between vortex cores measured on the free surface,  $D/a$ , are plotted. The vortex cores were first observed on the free surface at a nondimensional time of 13.0, after the vortex tube reconnection process is completed. The distance between vortex cores on the free surface and the distance of the lower vortex core to the free surface oscillate after the interaction. The two oscillatory motions are out of phase suggesting an oscillation of the opened vortex ring eccentricity with a period of approximately  $\Gamma_0 t_p / a^2 = 50$ . This value compares well with the theoretical calculation (Widnall and Sullivan, 1973) for small amplitude oscillations (mode  $n=2$ ) of a thin cored vortex ring having the initial circulation and the measured diameter and propagation speed after the interaction,  $\Gamma_0 t_p / a^2 = 41$ .

#### 4.2.1.2 Clean Free Surface

The experiments with contaminated surface suggest that vorticity generation at the surface can play an important role in the interaction of a vortex ring with a free surface at an incidence angle of  $\alpha=0^\circ$ . Similar experiments were conducted with the vortex generator and a clean surface obtained as described in Section 2.1. These experiments were conducted at several Reynolds numbers and initial vortex ring depths to clarify the role of these parameters on the extent of the interaction.

The experiments with a clean surface showed an evolution of the vortex rings similar to the contaminated surface case (Figure 4.6). The interaction of the upper core with the free surface always resulted in vortex line reconnection as with a contaminated surface. The main difference was in the interaction of the lower core with surface which did not result in opposite sign vorticity generation. The vortex core did not rebound. It appeared to break down as a result of the interaction. As for the clean surface the extent of the

interaction was determined from video recordings for the flow evolution at three different depths  $h/D_0 = 1.25, 1.5, 1.75$  and the five Reynolds numbers ( $\Gamma_0/\nu$ ) in Table 4.1. The results are shown in Figure 4.10 using the same notation as for the contaminated free surface. These results confirm that the normalized extent  $L/a$  depends exponentially on  $a/h$ , and is independent on Reynolds number. Also comparing these results to the results in Figure 4.7 for a contaminated free surface, it appears that the interaction occurs further downstream for a clean surface at low values of  $a/h$ .

#### 4.2.2 Normal Incidence to the Free Surface

The experiments at  $\alpha=0^\circ$  showed significant vorticity generation at a contaminated free surface. In a related investigation Willmarth and Hirs (Private Communication, 1989) studied the interaction of a vortex pair with the free surface, and also found significant effects attributed to the presence of surface active agents at the surface.

To examine the effect of surface active agent on the interaction of vortex rings with the surface the normal incidence ( $\alpha=90^\circ$ ) was chosen. This incidence angle was selected to avoid vortex line reconnection processes during the interaction, thus focussing these experiments on vorticity generation at the free surface. The vortex generator was positioned  $90^\circ$  to the free surface and the nozzle exit was at  $h/D_0=3.5$  below the free surface. For the experiments with a contaminated free surface, the water was left in the tank overnight without a surface cover and without surface current flow. The clean surface was obtained as described in Section 2.1.

Photographs of the evolution of the vortex ring cross-section were obtained at a Reynolds number ( $\Gamma_0/\nu$ ) of 3800 and Froude number of about 0.2 for both a contaminated and a cleaner free surface. Photographs are shown in Figure 4.11. Each photograph was obtained on a different realization of the flow. The location of the free surface is indicated on each photograph. Figure 4.11 (A) shows the interaction of the vortex ring with a contaminated surface. During the interaction secondary and tertiary vortex rings are formed

having vorticity opposite to that of the incoming vortex ring. This evolution of the vortex ring is very similar to the evolution at a solid surface (Cerra and Smith, 1983). This observation suggests that the water on the free surface did not move during the interaction. Observations of small particles on the free surface confirmed this conjecture indicating that capillary forces prevented fluid motion at the surface. A sequence of photographs of the vortex ring interaction with a cleaner free surface is shown in Figure 4.11 (B). The evolution of the vortex ring is closer to what would be expected in the absence of capillary forces at the surface. The self-induced outward motion of the vortex core persists for a longer time. Also the vortex core size is significantly reduced due to stretching.

Figure 4.12 and 4.13 are plots of the trajectory of the vortex ring core for the contaminated and cleaner surfaces respectively. In the case of a contaminated surface, the formation of the secondary and tertiary vortex rings limits the outward motion of the primary vortex to two and a half times the initial radius. Also the induced velocity field of these vortices causes the primary vortex core to rebound, i.e. it moves away from the surface. For the cleaner surface case shown in Figure 4.13 the outward motion persists to a radius of three and a half times the initial radius. Although there is dye left behind the primary vortex core, the amount of vorticity associated with this fluid should be small because the trajectory of the primary vortex core is not altered. A secondary vortex ring is formed similar to the one found in the contaminated surface case which causes the trajectory of the primary vortex to bounce away from the surface.

In summary these results show that surface contamination can have a profound effect on the interaction of vortex rings with the surface. Vorticity generation at the free surface and the subsequent roll up into secondary and tertiary vortices causes a very large change of the evolution of the ring. Even in the case of very small amounts of surface contaminants, like in the clean surface case, they eventually accumulate to generate a secondary vortex ring.

#### 4.2.3 Inclined Incidence to the Free Surface

The observations at  $\alpha = 0^\circ$  showed vortex line reconnection to occur as a result of the interaction of the vortex ring with the free surface. It was expected on the basis of this result and existing evidence on the interaction of colliding vortex rings that the interaction at an inclined incidence angle will also result in vortex lines reconnection. An extensive flow visualization study was conducted to determine the general features of the interaction in the range  $0^\circ < \alpha < 50^\circ$  at vortex ring generation conditions (1) to (4) in Table 4.1 and with a clean surface. A second objective of the study is to gain some understanding of the reconnection process. In all cases considered the Froude number of the interaction,  $\Gamma/(ga^3)^{1/2}$ , given in Table 4.1 is small which indicates small surface deformations during the interaction.

Simultaneous flow visualization of the underwater flow and of the free surface deformation was conducted at incidence angles  $\alpha = 5^\circ, 10^\circ, 15^\circ, 20^\circ, 30^\circ, 40^\circ, 45^\circ$  and  $50^\circ$ , for several vortex generator depths and operating conditions (1) to (5) in Table 4.1. The evolution of the vortices was recorded on video tape. The results show that the interaction of the upper vortex core with the surface always results in vortex line reconnection up to the maximum incidence angle tested of  $\alpha = 45^\circ$ . The interaction of the lower vortex core with the surface was a sensitive function of the vortex incidence angle and generation conditions. For incidence angle  $\alpha \leq 5^\circ$  the lower core interaction resulted in vortex breakdown at all Reynolds numbers. For incidence angles in the range  $40^\circ \leq \alpha \leq 45^\circ$  there was also vortex breakdown after the lower core interaction except the case (3) ( $\Gamma/\nu = 4960$ ). For  $10^\circ \leq \alpha \leq 30^\circ$  cases (1), (2), (4) and for  $10^\circ \leq \alpha \leq 45^\circ$  case (3) the interaction of the lower core with the free surface also results in vortex line reconnection. In these cases where the upper and lower core reconnect at the surface the vortex ring splits into two half rings each having vortex lines starting and terminating at the free surface (A detailed sequence of flow visualization pictures of this type of interaction is described

below in Section 4.3.1). These two half vortex rings propagate independent of each other after the interaction. The direction of propagation depended on the flow conditions. For case (3)  $15^\circ \leq \alpha \leq 30^\circ$  and case (4)  $15^\circ \leq \alpha \leq 30^\circ$  the half vortex rings propagate away from each other after the interaction. For case (1)  $15^\circ \leq \alpha \leq 30^\circ$ , case (2)  $15^\circ \leq \alpha \leq 30^\circ$  and case (3)  $40^\circ \leq \alpha \leq 45^\circ$  the half vortex rings propagate parallel to each other after the interaction. For case (1)  $\alpha = 10^\circ$  the half vortex rings propagate towards each other after the formation is completed.

One important parameter of the vortex line reconnection phenomena is the time required for the process to be completed. It could be argued that the vortex reconnection time should scale with the local vortex properties. On the other hand global parameters like the vortex ring incidence angle,  $\alpha$ , and the Reynolds number may also play a role. The reconnection time,  $t_r$ , was defined for the purpose of this study as the time elapsed from the initial contact of the vortex ring outline with the free surface to the time when the vortex cores are first observed as distinct dark spots on the free surface. The measurements were limited to the reconnection time of the upper vortex core. The nondimensional time  $\Gamma t_r / \delta^2$  is plotted as a function of Reynolds number  $\Gamma / \nu$  in Figure 4.14 for several vortex ring conditions. These results show that the nondimensional reconnection time is independent of the Reynolds number. The effect of incidence angle is significant and results in an increase of the normalized reconnection time with reduced incidence angle. At  $\alpha = 0^\circ$  there is somewhat more scatter in the results. The effect of increasing initial depth is to reduce the reconnection time. In any case the reconnection time at  $\alpha = 0^\circ$  is longer than the reconnection time for  $\alpha > 0^\circ$  in all cases investigated.

Schatzle (1987) argued that vorticity cancellation during the reconnection can only be attained by viscous diffusion and therefore the viscosity coefficient must appear on the proper normalization of the reconnection time. Our measurements do not support this conjecture since the vortex reconnection time at fixed incidence angle is independent of Reynolds number. This inviscid scaling was proposed by Ashurst and Meiron (1987). The

free surface velocity field measurements and detailed visualizations described in the next section provide some insight on this result.

### 4.3 The Double Reconnection Process

The double reconnection process was studied in detail for vortex ring generation conditions corresponding to case (3) in Table 4.1, i.e.  $\Gamma = 49.6 \text{ cm}^2/\text{s}$ ,  $a = 3.13 \text{ cm}$ ,  $\delta = 1 \text{ cm}$ . The vortex generator was positioned at  $h/D_0 = 1.72$  below the surface and the incidence angle was  $\alpha = 20^\circ$ . The corresponding Froude number  $\Gamma/(ga^3)^{1/2}$  is 0.29. Although double reconnection were observed at other conditions, these particular conditions were selected because they resulted in a highly reproducible evolution of the vortex rings. Figure 4.15 is a cross-section picture of the vortex ring as it approaches the surface, before any significant interaction with the surface has occurred.

#### 4.3.1 Flow Visualization

Figure 4.16 (a) to (g) is a sequence of photographs showing the double reconnection process. The photographs were obtained on different realizations of the flow at nondimensional times  $\Gamma t/a^2 = 4.56, 5.57, 6.58, 7.59, 8.61, 9.62$  and  $10.63$  as indicated. At each instant a cross-section view of the underwater flow and a shadowgraph image of the surface are presented. These were also obtained on different realizations of the flow. The two views are arranged in the proper relative downstream position in Figure 4.16. The shadowgraph system was imaged 43 cm above the surface to obtain a better quality image and to increase the sensitivity in order to detect possible surface waves generated during the interaction.

The vortex line reconnection process of the upper vortex is already started at  $\Gamma t/a^2 = 4.56$  in Figure 4.16 (a). This reconnection process is completed at  $\Gamma t/a^2 = 6.58$ , Figure 4.16 (c). An interesting observation is the generation of surface waves during the

reconnection process  $\Gamma t/a^2 = 5.57$  to  $6.58$ . These waves which are not present before the interaction appear to emanate from the interaction region and radiate away from it (cf. Figure 4.16 (b) and (c)). Note that there is no dye associated with the upper vortex core left on the visualized plane after the reconnection process.

The vortex line reconnection process of the lower core of the ring occurs between  $\Gamma t/a^2 = 7.59$  to  $9.62$  (Figure 4.16 (d) to (f)). As the vortex line reconnection process develops dye in the cross-section plane is removed. Also two additional dark spots appear on the surface signature indicating the presence of vortex lines terminating at the surface. After the double reconnection process is completed, Figure 4.16 (f) and (g), the upper two dark spots on the surface are interconnected by underwater vortex lines. Similarly the lower two dark spots on the surface are also interconnected by vortex lines below the surface. The two sets of dark spots propagate away from each other as shown in Figure (f) and (g). Again during the second reconnection process, Figure 4.16 (f), there are surface waves generated although the propagation pattern is more complicated than in the first reconnection. In contrast to the first reconnection, some dye is left on the visualized cross-section after the second reconnection. Further the cross-section view of Figure 4.16 (g) shows evidence of counterclockwise vorticity to the left side of the remaining dye. This counterclockwise vorticity must be left behind by the lower vortex core. This vorticity must interconnect the diverging pair of half vortex rings. The total amount of vorticity in this vortex appears to be small.

Detailed data on the vortex core evolution of the double reconnection process were measured from the video recordings. Simultaneous visualization of the underwater flow and surface deformation were obtained using the technique described in Section 2.3. Figure 4.17 is a plot of the downstream location of the vortex ring cores and the distance of the vortex ring cores to the free surface normalized by the initial vortex ring diameter,  $X/a$  and  $Y/a$  respectively, as a function of the nondimensional time ( $\Gamma t/a^2$ ). The speed of propagation of the upper vortex core is essentially constant until it disappears from the

cross-section. The lower vortex core also moves with constant speed during most of the interaction. Only in the later stages of the interaction, it slows down significantly. A least square fit to the data gives a nondimensional propagation speed  $U_1 a / \Gamma = 0.477$ .

The trajectories of the vortex cores on the free surface in normalized coordinates are plotted in Figure 4.18. In this figure the straight lines join the locations of the upper and lower vortex cores on the surface at the indicated nondimensional time. The nondimensional propagation speed of the upper vortex core at the initial state after reconnection is 0.532 and the propagation angle with respect to the centerline is  $54.3^\circ$ . For the lower vortex core, a nondimensional propagation speed of 0.334 and a propagation angle of  $20.4^\circ$  are measured at opening time. For the steady state downstream of  $X/a \approx 6$ , the measured nondimensional speed and propagation angle are 0.280 and  $21.2^\circ$  respectively. After the interaction the diameter of the resulting half vortex rings is increased by 19% compared to the initial diameter. The propagation speed is reduced by about 38%. This is due to the loss of vorticity during the interaction as well as increased vortex diameter.

#### 4.3.2 Free Surface Velocity Field

The velocity field at the surface was measured using the Laser Speckle Photography technique discussed earlier. As described earlier the optical system used was a shadowgraph system with the photographic plate positioned 1 cm above the surface (See Figure 3.23). The specklegrams obtained in this manner contain not only the particle displacement information, but also they provide a low sensitivity shadowgraph visualization of the surface. Although the simultaneous visualization provides very useful information on the interaction process, the intensity nonuniformity caused by surface deformation prevented recording of the speckle pattern in several regions of the flow. In these experiments fluid in the generator was not seeded with particles. Therefore regions on

the surface where the fluid originated in the generator were not seeded and consequently the velocity could not be measured there.

Specklegrams of the interaction were obtained at nondimensional times  $\Gamma t/a^2 = 4.56, 5.57, 7.09, 8.10, 9.62$  and  $10.63$ . Contact prints of these specklegrams are reproduced in Figure 4.19 (a) to (f) respectively. The vortex ring motion is from right to left. In Figure 4.19 (a) at  $\Gamma t/a^2 = 4.56$  a curved dark region indicates a surface depression caused by the underwater vortical flow. This region is preceded by a wide region of surface elevation and followed by a much narrower elevated region. In Figure 4.19 (b) at  $\Gamma t/a^2 = 5.57$  the first reconnection process has been completed as indicated by the presence of two distinct dark spots on either side of the centerline. The dark spots are connected by a sharply defined line. This line separates the microballoon containing region of the surface from the clean region of the surface produced by upwelling of fluid from below the surface. A similar but more diffused transition from clean surface to microballoon containing surface is observed on the upstream side of the ring. The same general features are observed in Figure 4.19 (c) at  $\Gamma t/a^2 = 7.09$ , the main difference being the increased distance between the cores. Figure 4.19 (d) and (e) obtained for  $\Gamma t/a^2 = 8.10$  and  $9.62$  respectively show the surface deformation as the lower vortex core approaches the surface. Comparison with Figure 4.19 (a) shows the same local features except that in this case the surface deformation region is curved downstream instead of upstream. Also, in these two images the transition from fluid with particles to fluid without particles upstream of the interaction region is sharp while downstream it is more diffused. Finally in Figure 4.19 (f) at  $\Gamma t/a^2 = 10.63$  when the double reconnection process is completed two additional dark spots are observed on the surface.

Vector plots of the surface velocity field measured on the specklegrams in Figure 4.19 (a) to (f) are given in Figure 4.20 (a) to (f). As expected the velocity could not be measured in very dark or very bright regions of the specklegrams as well as in regions where there are no particles. Unfortunately these regions include the vortex cores

themselves. Each specklegram was interrogated in a square region 8 x 8 cm at 0.25 cm intervals. The velocity scale is the same in all the plots and is shown in Figure 4.20 (a). For  $\Gamma/a^2 = 4.56$  to 8.10, Figure 4.20 (a) to (d), the vector plots show the velocity field induced by two vortex cores. At  $\Gamma/a^2 = 9.62$  and 10.63 the measurements show the induced velocity field of the counter rotating vortices. The presence of this vortex results in a stagnation point and reverse flow in a region on the symmetry plane.

#### 4.3.3 Deformation Rate Field Analysis

From the measurements of velocity field at the surface the components of the deformation rate tensor in the plane of the free surface and the component of the vorticity normal to the free surface were calculated using the methods described in Section 3.3. In addition, the component of the deformation rate normal to the surface was calculated from the continuity equation

$$\epsilon_{zz} = 2 \frac{\partial w}{\partial z} = -2 \left( \frac{\partial u}{\partial x} + \frac{\partial v}{\partial y} \right) \quad (4.9)$$

where  $\partial w/\partial z$  is gradient of the velocity component normal to the surface in the direction normal to the surface. A positive value of  $\epsilon_{zz}$  indicates that fluid below the surface and close to it moves away from the surface. Similarly a negative value of  $\epsilon_{zz}$  indicates motion of the fluid below the surface toward the surface.

The results for the vorticity field showed very small amounts of vorticity throughout the measured region. This is consistent with the fact that the vorticity is concentrated in the vortex cores where measurements could not be conducted due to large surface deformation.

The results for the deformation rate are presented in Figure 4.21. At each point the measured  $\epsilon_{xx}$ ,  $\epsilon_{yy}$  and  $\epsilon_{xy}$  were used to determine the principal axes and corresponding

deformation rates. It should also be noted that at a free surface in the absence of capillary effects and neglecting the effect of air above the surface, the components of the deformation rate tensor on the plane of the free surface are zero. It follows that the local normal to the free surface is a principal axis of the deformation rate. Thus for small surface deflections  $\epsilon_{zz} = \epsilon_{33}$  the deformation rate along the third principal axis. The results are presented in Figure 4.21 in the form of a vector plot, labeled (A) at each flow condition. At each point the two principal axes are indicated by two perpendicular vectors in the directions of the principal axes. The magnitude of each vector is proportional to the magnitude of the corresponding deformation rate value. An arrowhead on each vector is used to indicate the direction of the deformation rate. An arrowhead pointing away from the measurement point indicates an extensional (positive) deformation rate. An arrowhead pointing towards the measurement point indicates a compressional (negative) deformation rate. Also shown in Figure 4.21 are contour plots of the  $\epsilon_{zz}$  deformation rates, labeled (B) at each flow condition. The contour values plotted are  $\epsilon_{zz} = -6, -4, -2, -1, 1, 2, 4, 6$  with the region for  $\epsilon_{zz} > 1$  (downward flow) indicated by cross lines in each plot. General examination of the data shows that the deformation rate  $\epsilon_{xx}$ ,  $\epsilon_{yy}$  and  $\epsilon_{xy}$  are very sensitive to the uncertainty of the velocity measurements. The uncertainty of the  $\epsilon_{zz}$  deformation rate is believed to be slightly higher than the x-y plane components. At  $\Gamma/a^2 = 4.56$ , Figure 4.21 (a), there is stretching in the direction perpendicular to the plane of symmetry accompanied by upwelling ( $\epsilon_{zz} < 0$ ) just upstream of the interaction region near the symmetry plane. There is a region of positive  $\epsilon_{zz}$  and consequently downward flow behind the interaction. At  $\Gamma/a^2 = 5.57$ , Figure 4.21 (b), after the first reconnection the deformation rate shows the same basic features as at  $\Gamma/a^2 = 4.56$ . At  $\Gamma/a^2 = 7.09$ , Figure 4.21 (c), the deformation rate pattern changes to downward motion upstream of the interaction. There is also a region of upwelling to the side of the interaction in front of the vortex core. At  $\Gamma/a^2 = 8.10$ , Figure 4.21 (d), the regions of upwelling and downward motion continue to extend laterally following the lateral motion of vortex core. Upstream of the interaction a region of

downward motion is closely followed by a region of upwelling. The magnitude of the deformation rate is small throughout the entire image. At the beginning of the second reconnection,  $\Gamma t/a^2 = 9.62$ , Figure 4.21 (e), there are regions of strong upwelling and lateral straining just upstream of the interaction. Finally at  $\Gamma t/a^2 = 10.63$ , Figure 4.21 (f), the contour plot of  $\mathcal{E}_{zz}$  shows a larger region of upwelling upstream of the vortex cores. Also bands of downward motion followed by upwelling are observed. These are believed to be associated with surface waves. The wavelength 1 cm is in agreement with the wavelength measured on the photographs in Figure 4.16 and also they are of the order of vortex core size.

The combination of flow visualization pictures, Figure 4.17 and 4.19, surface velocity field, Figure 4.20, and deformation rate field provide a detailed characterization of the vortex reconnection process. If we focus on the reconnection of the upper vortex core, Figure 4.17 (a), 4.19 (a), 4.20 (a) and 4.21(b) suggest a slightly different dynamics that proposed by Schatzle (1987). At  $\Gamma t/a^2 \approx 4.56$ , the surface velocity field and surface visualization indicate that in a stationary frame of reference there are two stagnation points on the surface. One is located in front (to the left) of the vortex core in the light region on the shadow images (Figure 4.17(a) and 4.19(a)) the other is located behind the vortex core (to the right) in the narrow bright region on the shadowgraph behind the kidney shaped dark surface depression. These two stagnation points are within the region where velocity measurements could not be obtained in the velocity field plot in Figure 4.20 (a), however, they are consistent with the overall flow pattern. The kidney shaped dark region between the two stagnation points indicates that the surface velocity there must be large and directed upstream to be consistent with the cross-sectional view. The deformation rate field further shows that in the neighborhood of the front stagnation point there is upwelling, a small compressional deformation rate in the flow direction and a large extensional deformation rate in the direction perpendicular to the symmetry plane. Therefore, near this stagnation point the component of vorticity parallel to the surface and perpendicular to the symmetry

plane is enhanced by stretching as described by Schatzle (1987). In contrast the flow near the stagnation point behind the vortex core shows a downward motion which will result in enhancement of the vorticity component perpendicular to the surface. The velocity vector plot suggests compressional deformation rates on the free surface. Due to the limited number of point measurements of the deformation rate were not obtained in this region. Such a compressional deformation rate would result in an exponential reduction of the vorticity components parallel to the surface.

It is apparent that deformation rate near the stagnation point behind the vortex core will result in the generation of vorticity perpendicular to the free surface. As this vorticity is generated the induced velocity field reduces the upstream velocity between the two stagnation points and moves the stagnation points closer to each other until they merge. At  $\Gamma t/a^2 = 5.57$  the surface visualization pictures and surface flow field indicate that the flow has reached this state.

## CHAPTER V

### SUMMARY AND CONCLUSIONS

Perhaps the most striking result of this investigation is the detailed documentation of the double reconnection process occurring in the interaction of a vortex ring with the free surface. In this type of interaction the initially axisymmetric vortex ring splits into two "half" rings each consisting of semicircular vortex lines beginning and terminating at the surface. These two "half" rings propagate along diverging paths parallel to the surface. It was found that surface waves are generated during each of the two reconnection processes. The phenomenon was observed over a range of vortex ring Reynolds number from 2000 to 7000 and incidence angles from  $10^\circ$  to  $45^\circ$ . The first reconnection process, that of the upper core was always observed up to an incidence angle of  $45^\circ$ . At low Reynolds number, short slug length and small incidence angle the "half" vortices formed by double reconnection merged again after a short distance. These results are in general agreement with observation of colliding vortex rings by Kambe and Takao (1971), Fohl and Turner (1975), Oshima and Asaka (1977), Schatzle (1987) and Oshima and Izutsu (1988).

A systematic study of the vortex reconnection process indicates that the reconnection time normalized by core parameters is independent of Reynolds number. The reconnection time does depend on the incidence angle of the vortex ring. A detailed analysis of the reconnection process using flow visualization and surface velocity field data indicates that the deformation rate field in the neighborhood of an stagnation point formed behind the vortex lines is responsible for the rapid decay of the vorticity component parallel to the free

surface and the rapid increase by stretching of the vorticity component perpendicular to the free surface, characteristic of the reconnection process. Viscous diffusion does not play an determining role on the vortex reconnection.

At zero incidence angle, when the vortex ring moves initially parallel to the free surface, the distance from the vortex generator to the interaction point and the extent of the interaction were found to depend only on the normalized depth of the vortex generator. They are independent of the vortex ring Reynolds number.

Surface contamination by surface active agents was found to strongly influence the interaction of vortex rings with the free surface. At an incidence angle of  $\alpha = 0^\circ$  with a contaminated free surface the upper vortex core reconnection process was still observed. The interaction of the lower vortex core resulted in significant generation of opposite sign vorticity and rebounding of the core away from the surface. At an incidence angle of  $\alpha = 90^\circ$ , normal incidence, the interaction with a highly contaminated surface resulted in significant opposite sign vorticity generation at the free surface. This vorticity rolled up into secondary vortices in a manner similar to the interaction with a solid surface. With a cleaner surface the results showed significantly reduced generation of opposite sign vorticity and a delay on the formation of the secondary vortex. A more systematic study of the effect of surface contamination is necessary to clarify these interaction processes. In particular the effect of surface contamination on the double reconnection of vortex rings at a free surface need to be systematically investigated.

A new technique based on Laser Speckle Photography was used to measure the velocity field at the surface. The main limitation of the technique as implemented in this study was the effect of surface deformation and seeding which limited the region where velocity measurements could be obtained. The advantage in this configuration is that in addition to the velocity field a simultaneous visualization of the free surface deformation is obtained. A new digital image analysis technique was developed to determine the velocity from the speckle photographs. This technique was tested and found to have an accuracy

better of 1% in the determination of the velocity field. From the velocity field the components of the vorticity and the deformation rate tensor normal and in the plane of the free surface, respectively, were determined. The principal axes and associated principal values of the deformation rate tensor were also determined as well as the deformation rate in the direction normal to the surface.

**FIGURES**

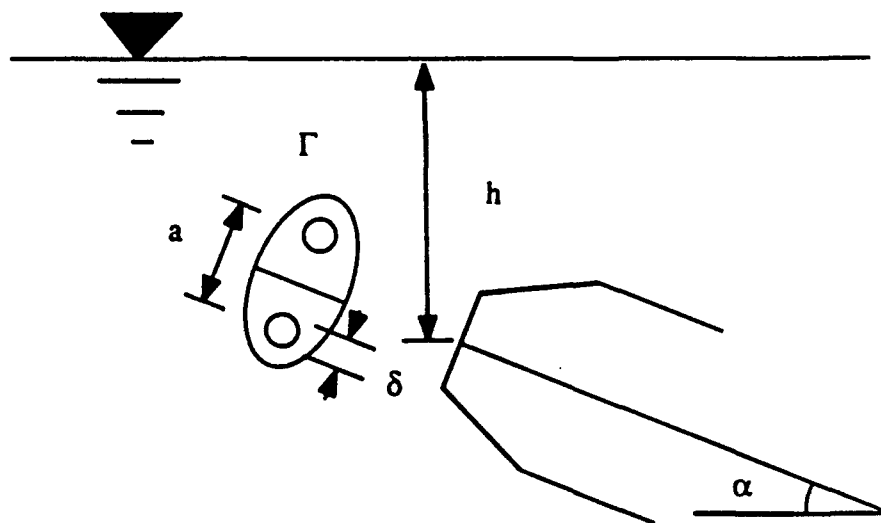


Figure 1.1 Schematic diagram of the flow geometry.  
 $\Gamma$ , Circulation;  $a$ , Ring diameter;  $\delta$ , Core size;  
 $\alpha$ , Incidence angle;  $h$ , Depth.

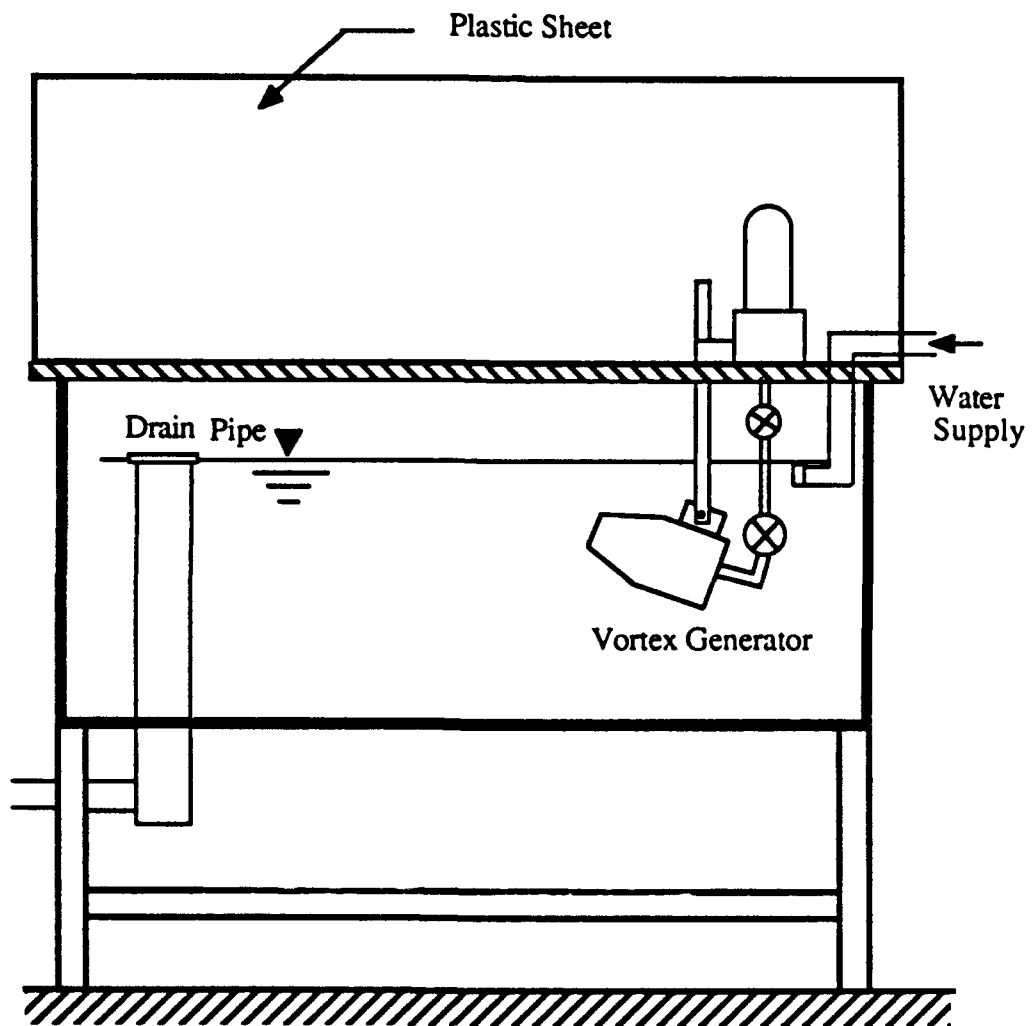


Figure 2.1 Schematic diagram of the facility.

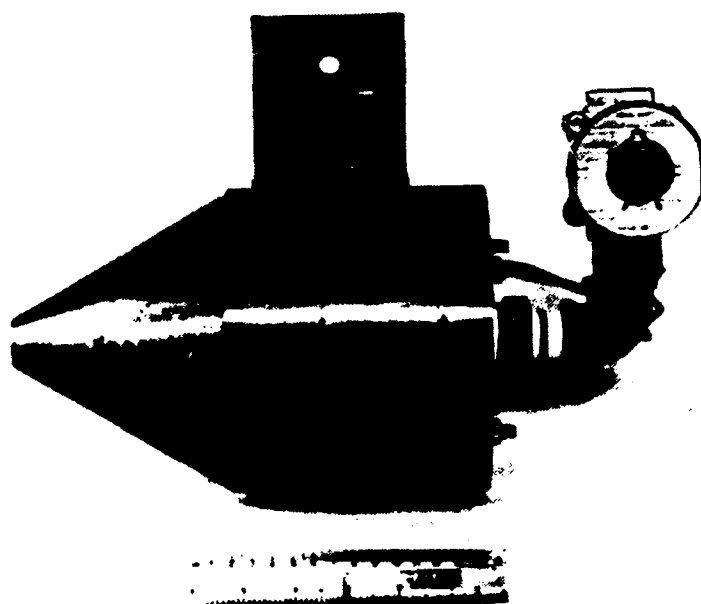


Figure 2.2 Photograph of the vortex generator.

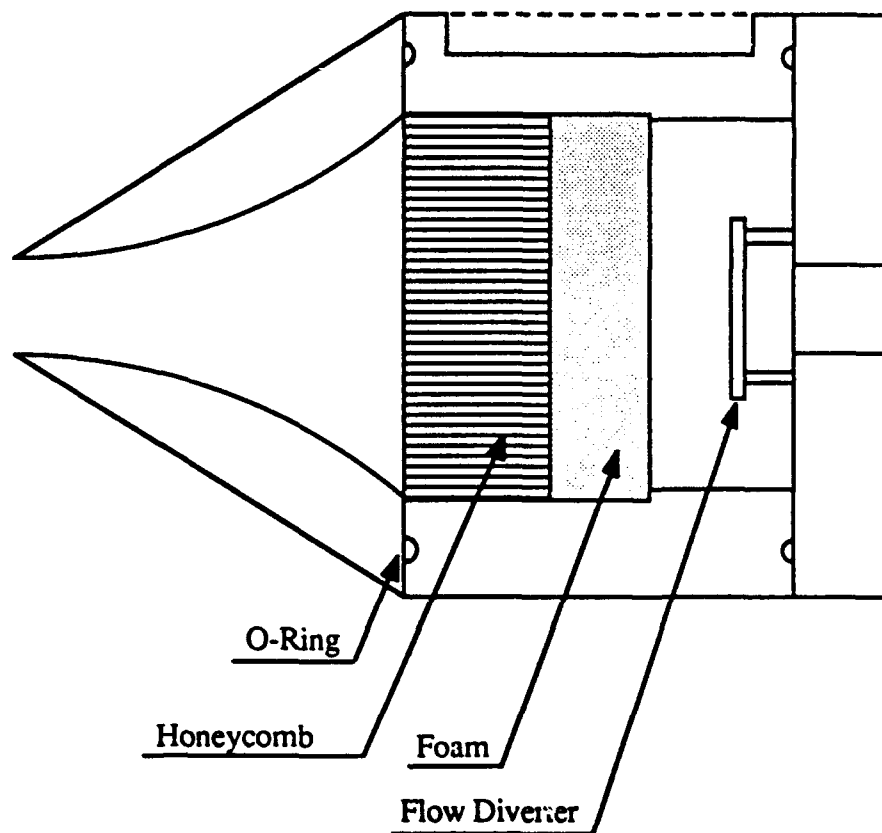


Figure 2.3 Detail of the vortex generator assembly.

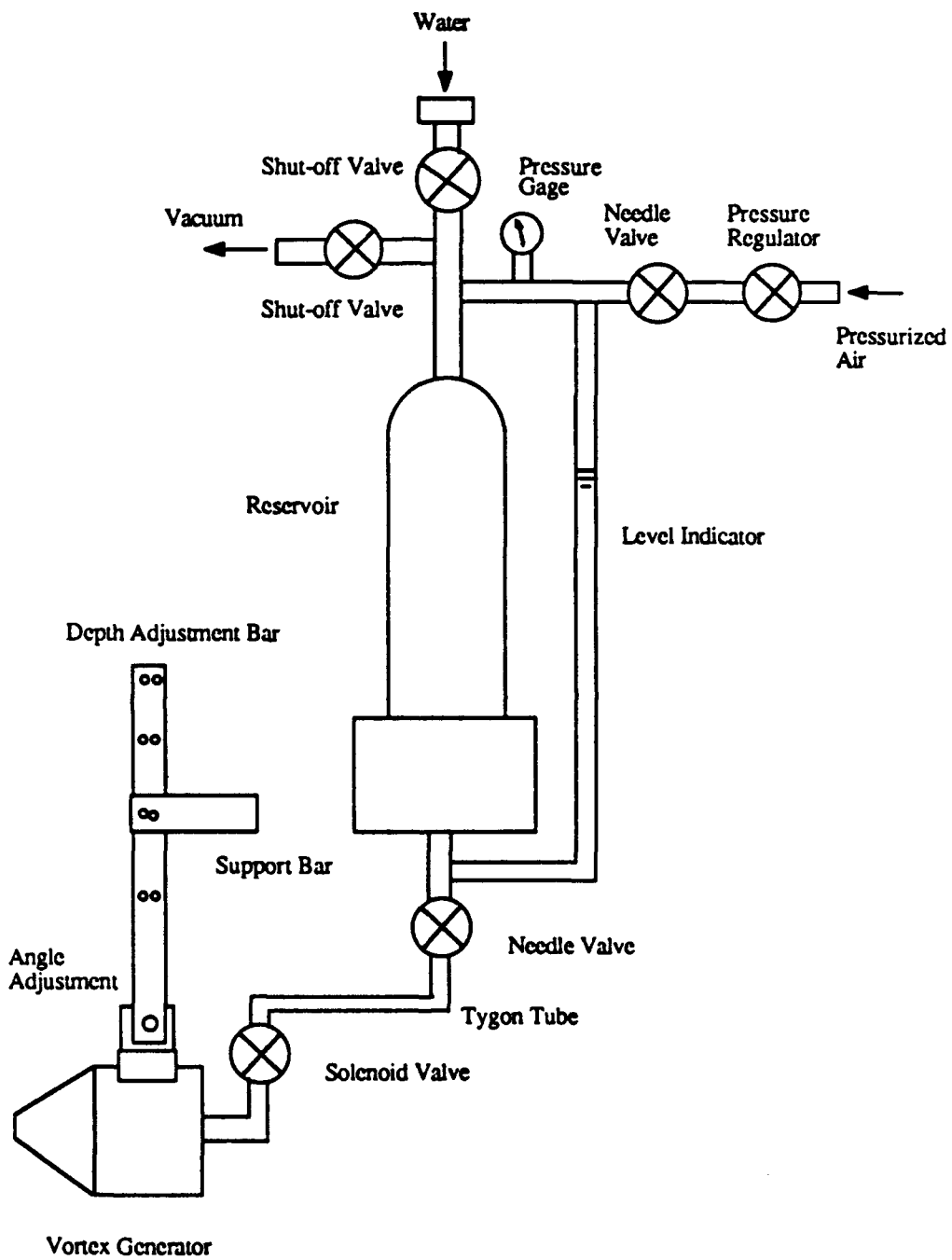


Figure 2.4 Vortex generator apparatus.

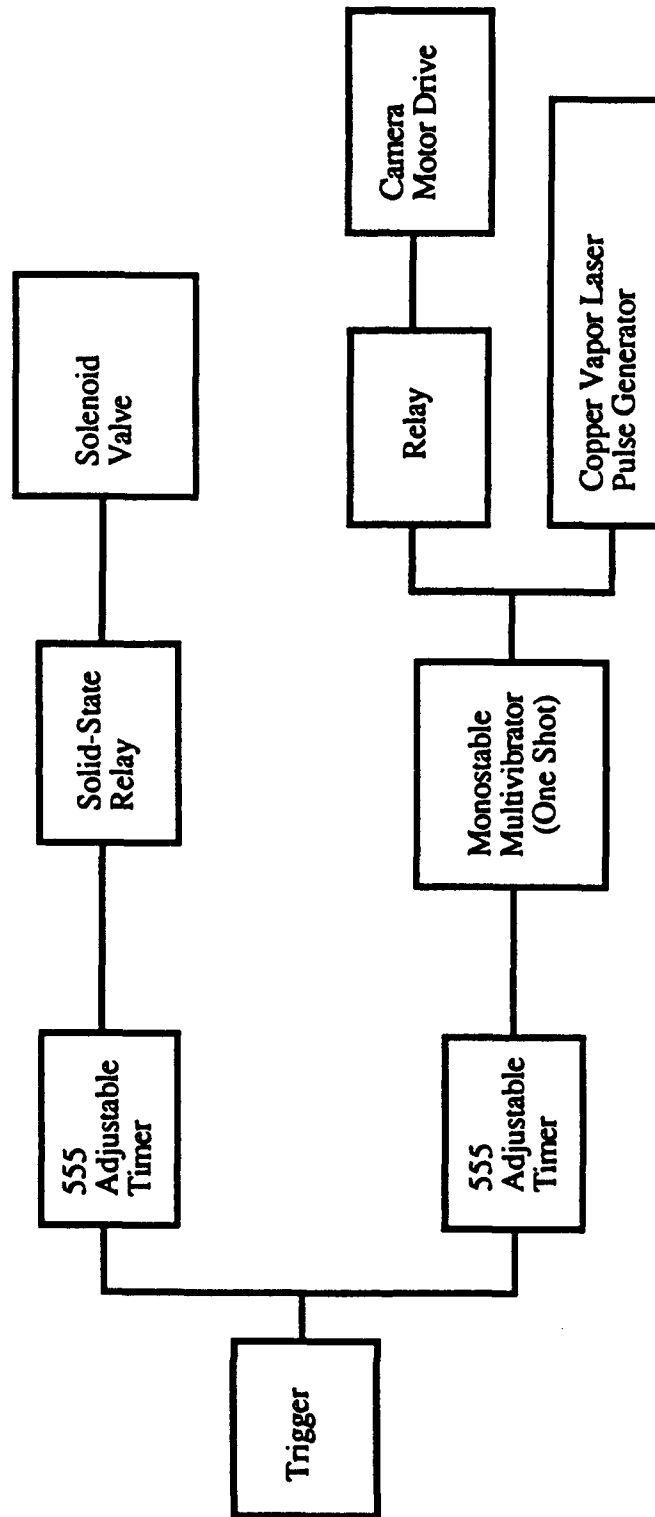


Figure 2.5 Block diagram of votex generator driving circuit.

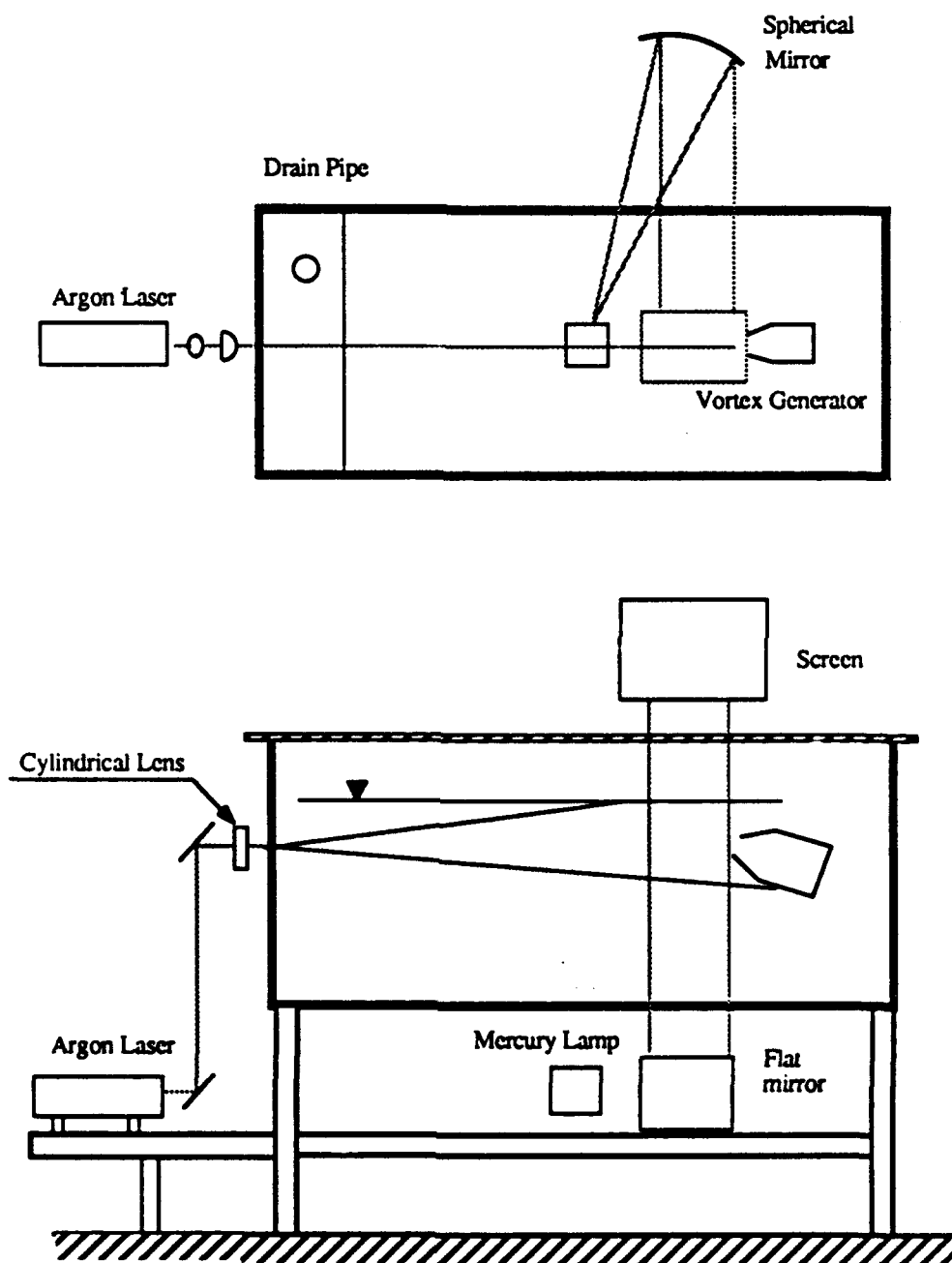


Figure 2.6 Schematic diagram of simultaneous flow visualization.

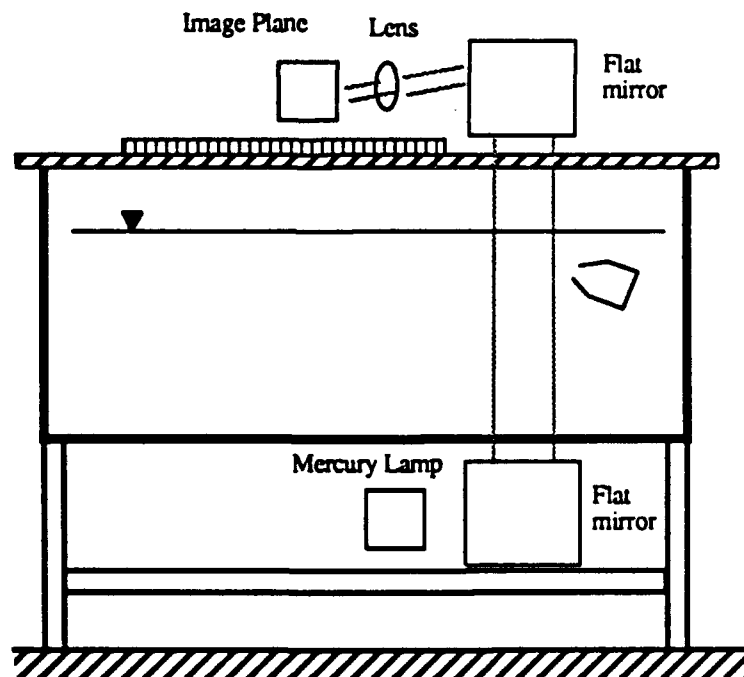
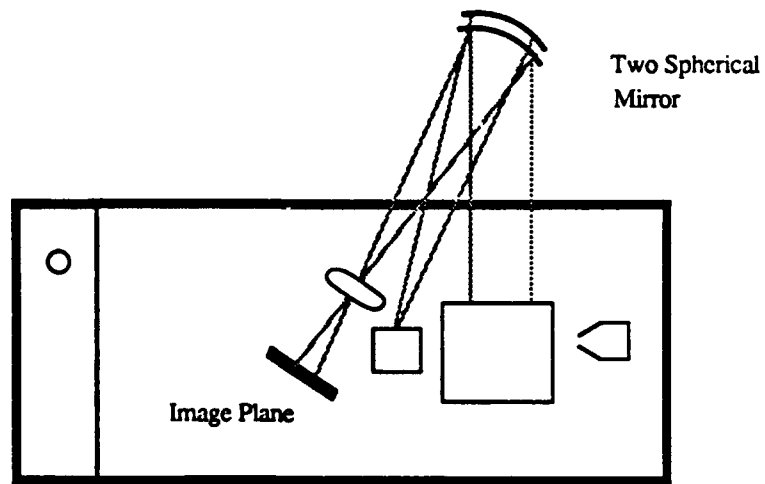


Figure 2.7 Schematic diagram of imaging system.

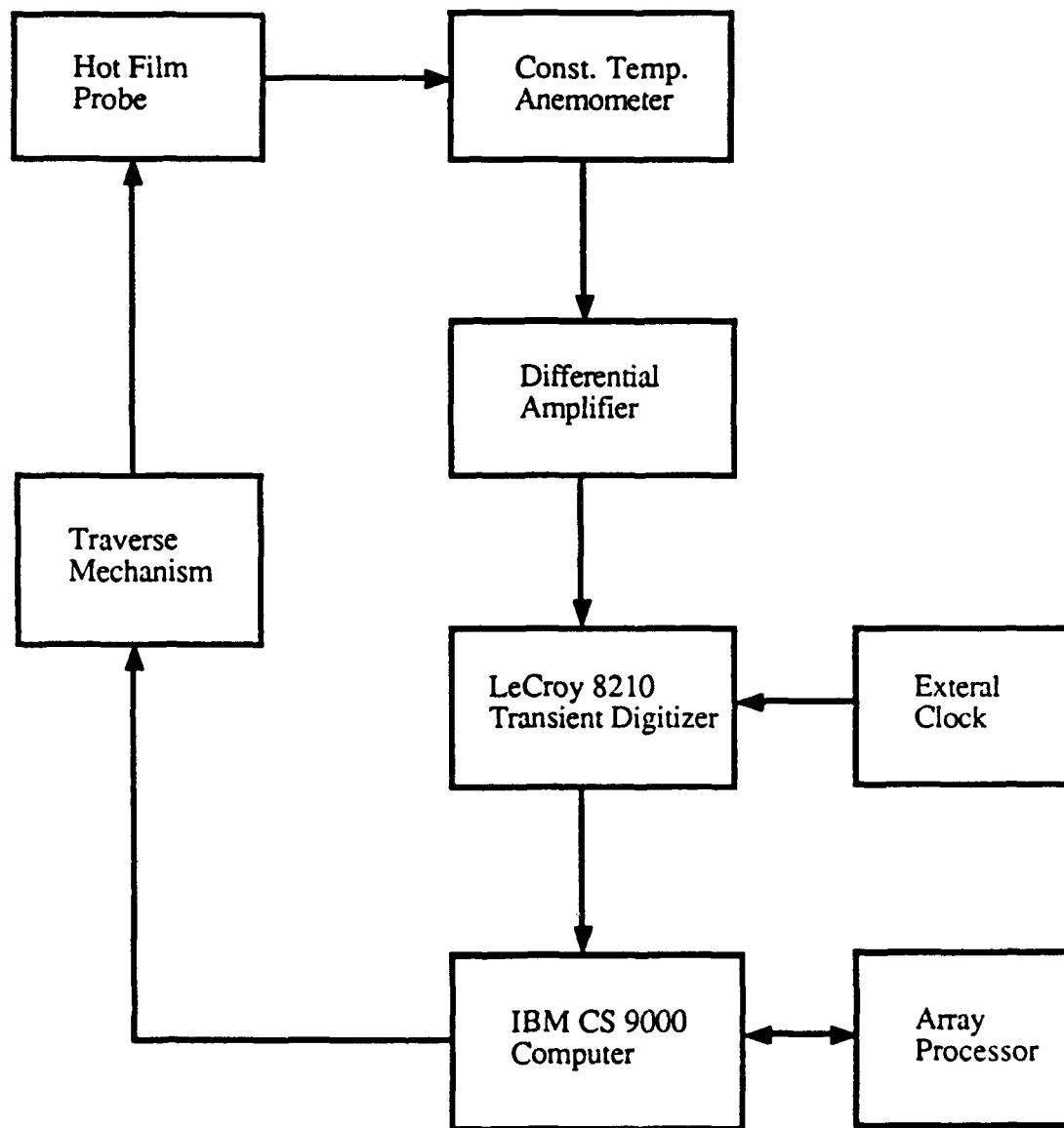


Figure 2.8 Block diagram of hot film velocity measurement system.

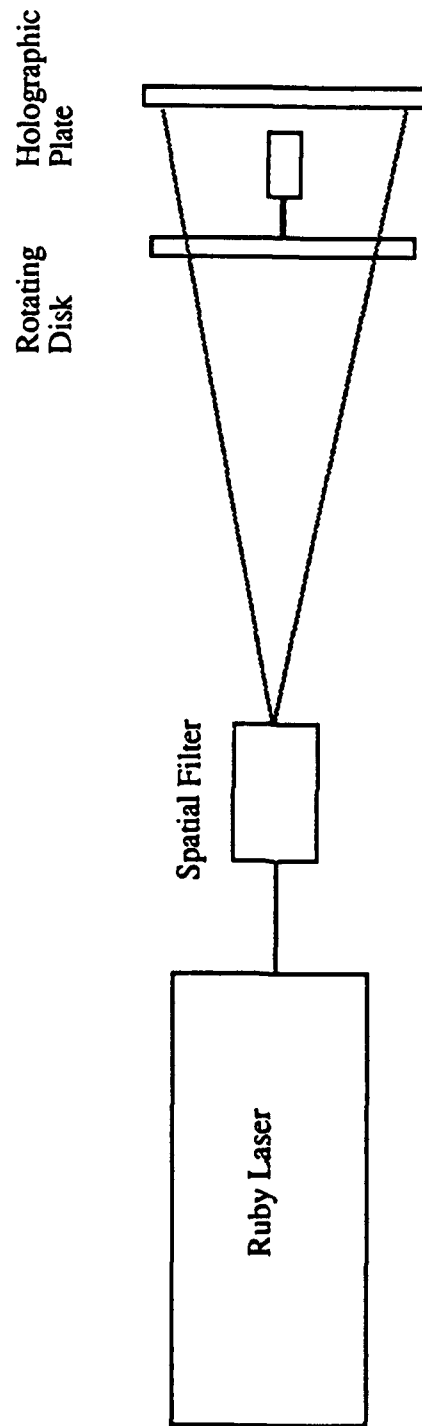


Figure 3.1 Schematic diagram of the rotating disk experiment.

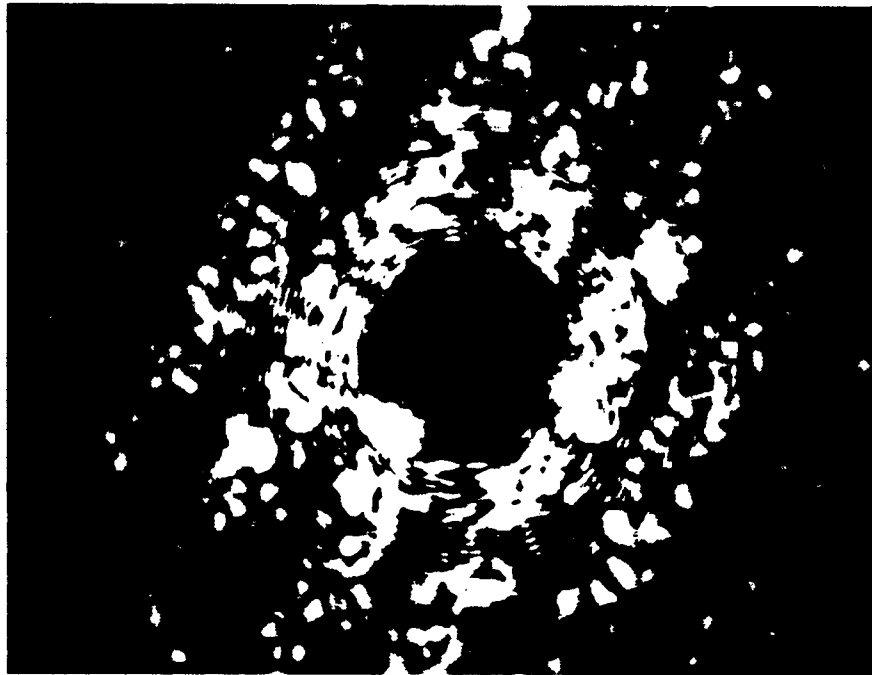


Figure 3.2 Photograph of a typical fringe image.

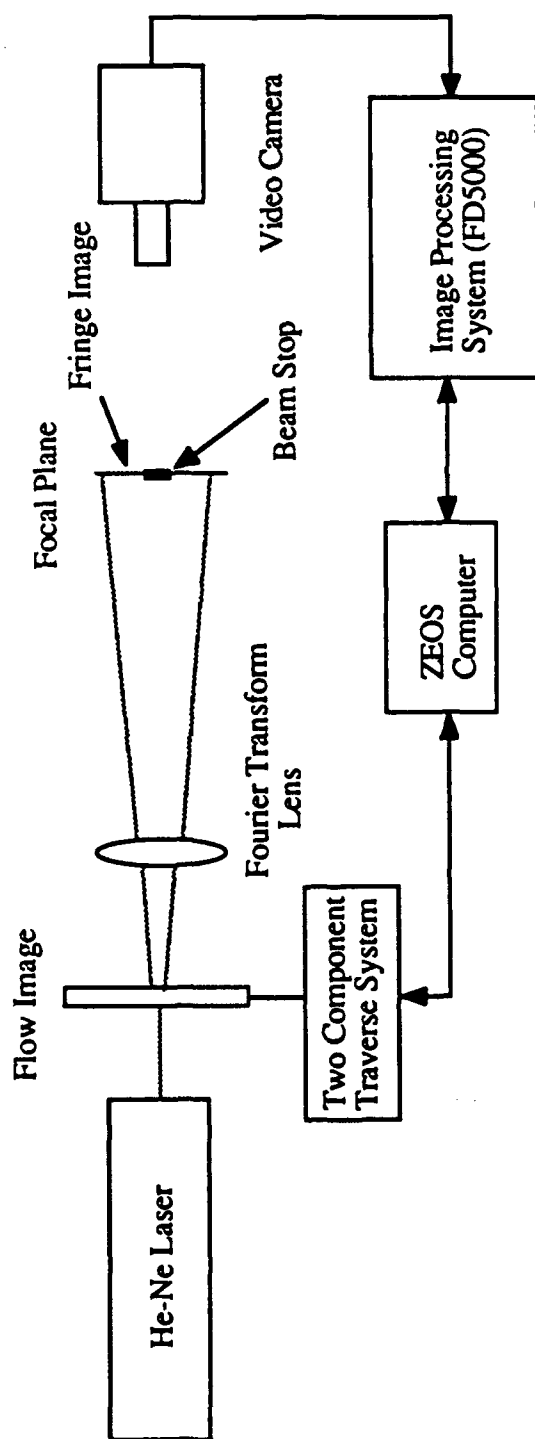


Figure 3.3 Schematic diagram of the digital image processing system.

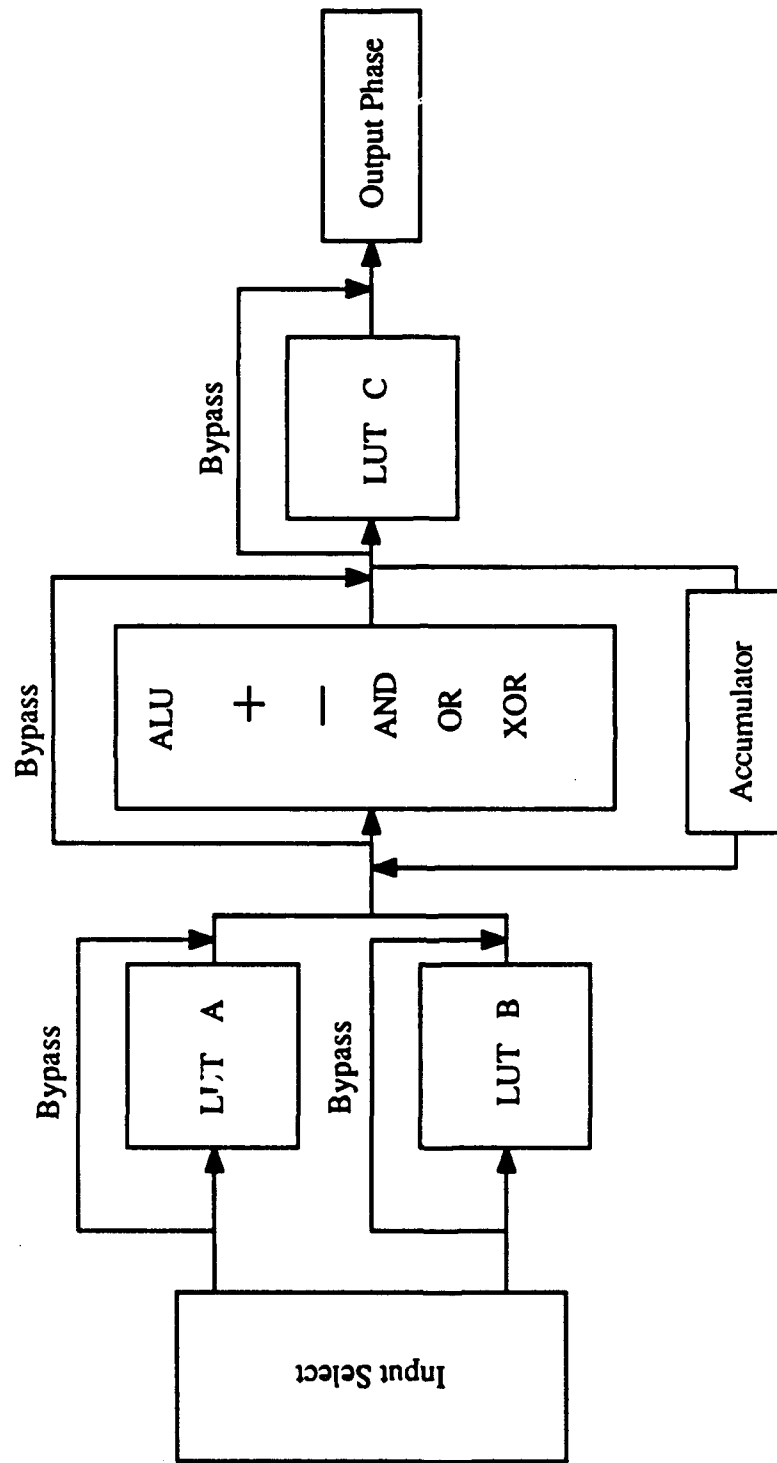


Figure 3.4 Block diagram of the Feedback Processor.

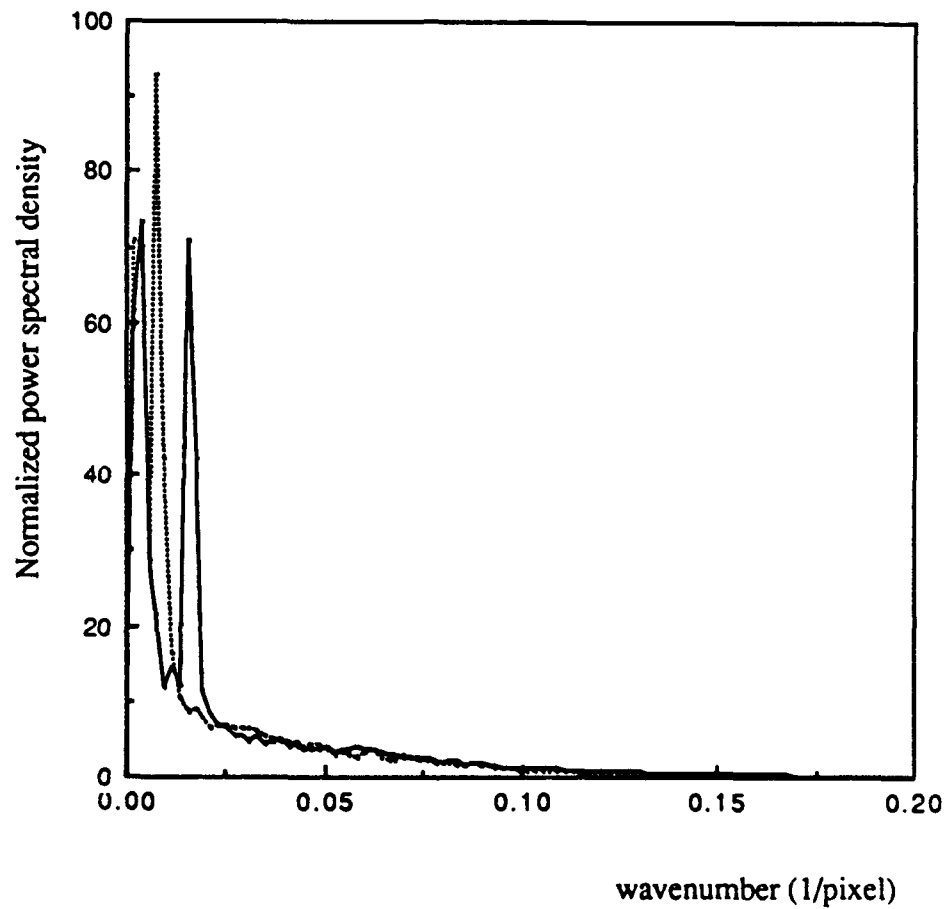


Figure 3.5 Power spectral density normalized to unit area vs. wavenumber of fringe image. —, Horizontal spectrum; ·····, Vertical spectrum.

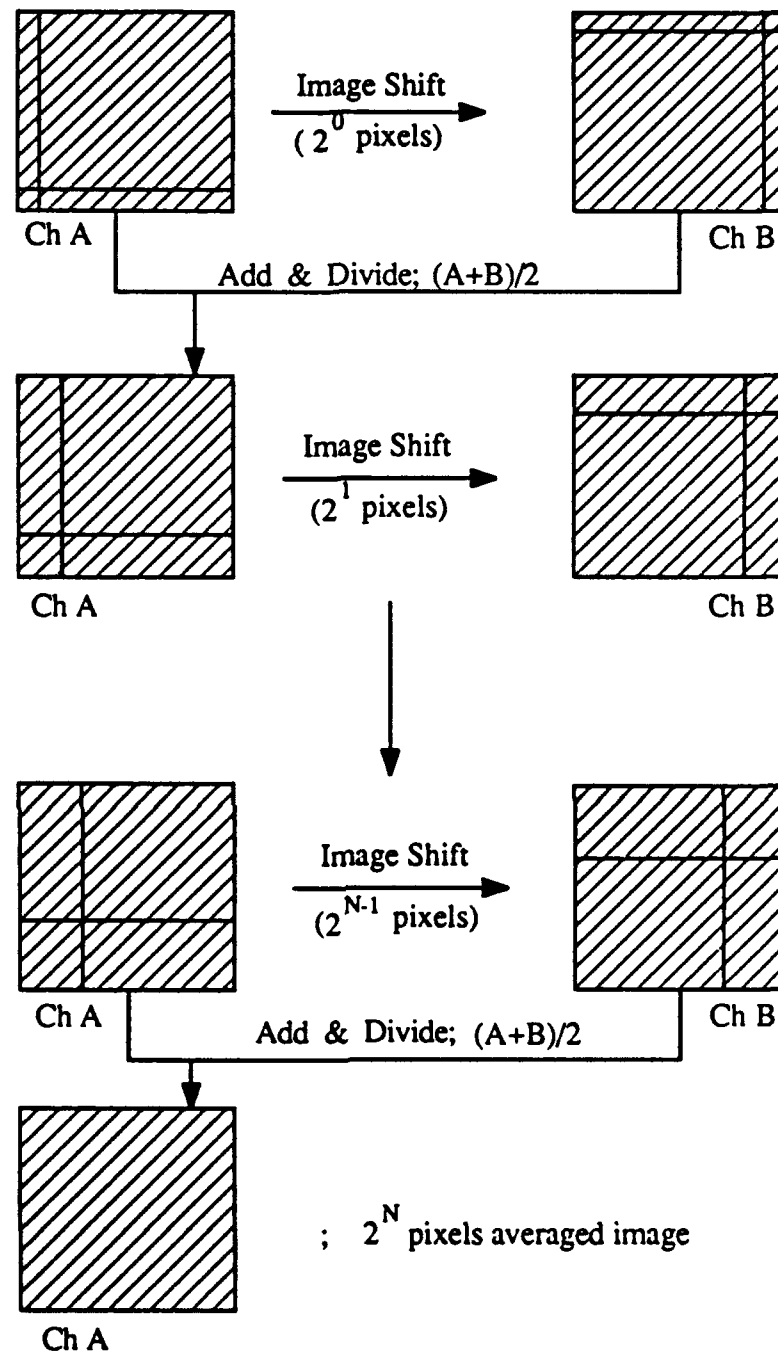


Figure 3.6 Schematic diagram of the line averaging technique.



Figure 3.7 Photograph of line averaged image for fringe image in Figure 3.2.

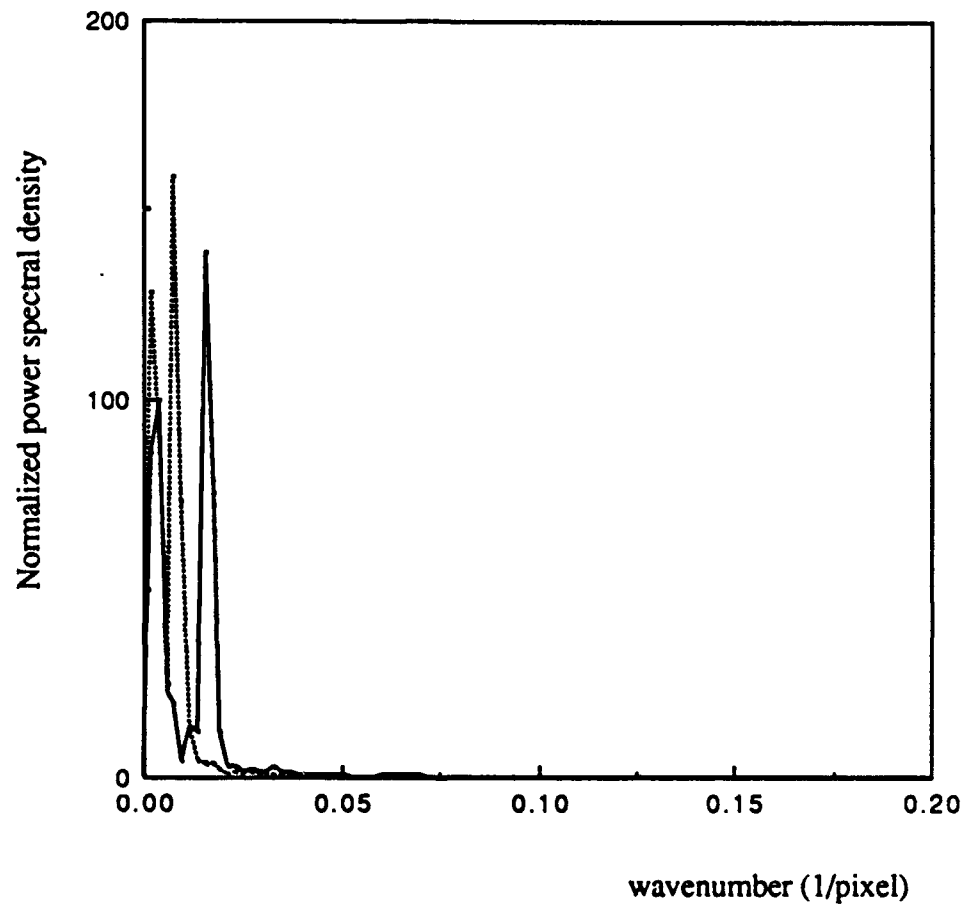


Figure 3.8 Power spectral density vs. wavenumber of the line averaged image.  
——, Horizontal spectrum; ....., Vertical spectrum.

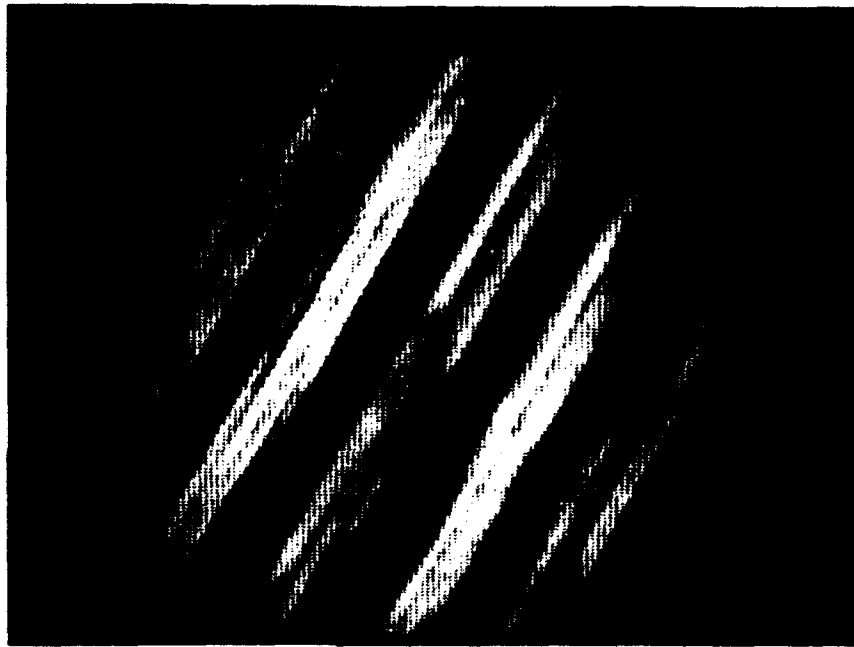


Figure 3.9 Photograph of image after background subtraction.

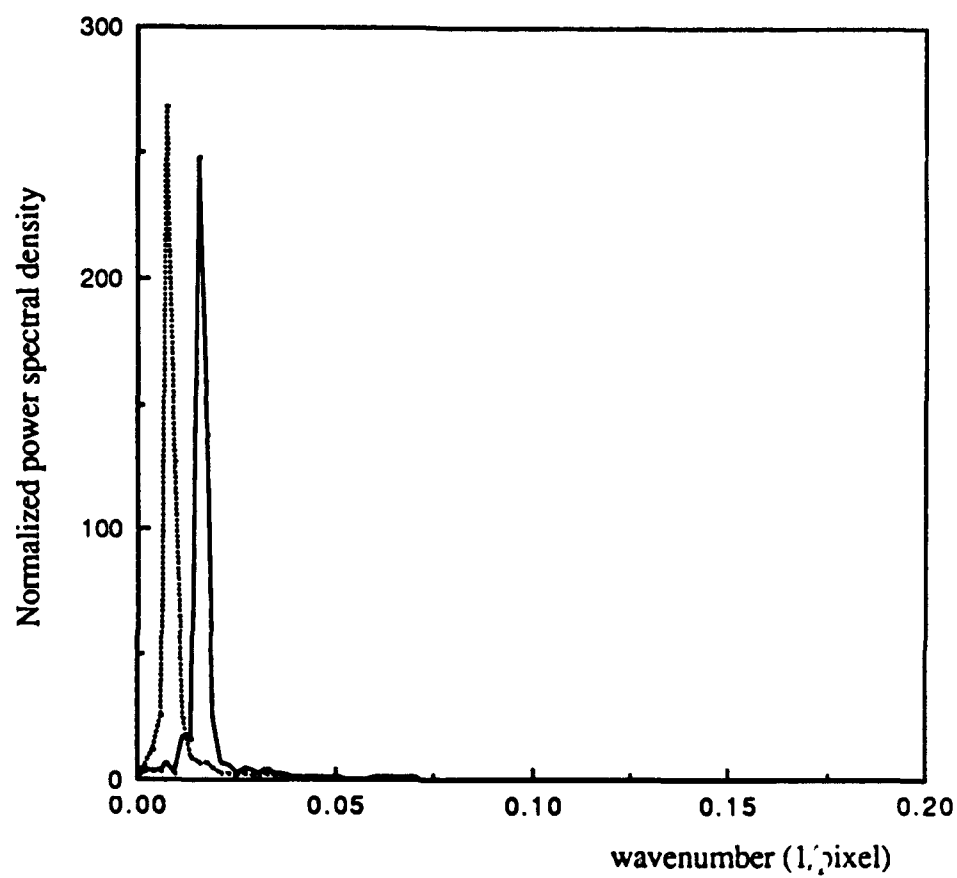


Figure 3.10 Power spectral density vs. wavenumber of the image after background subtraction. \_\_\_\_\_, Horizontal spectrum; ....., Vertical spectrum.



Figure 3.11 Photograph of image after contrast enhancement.

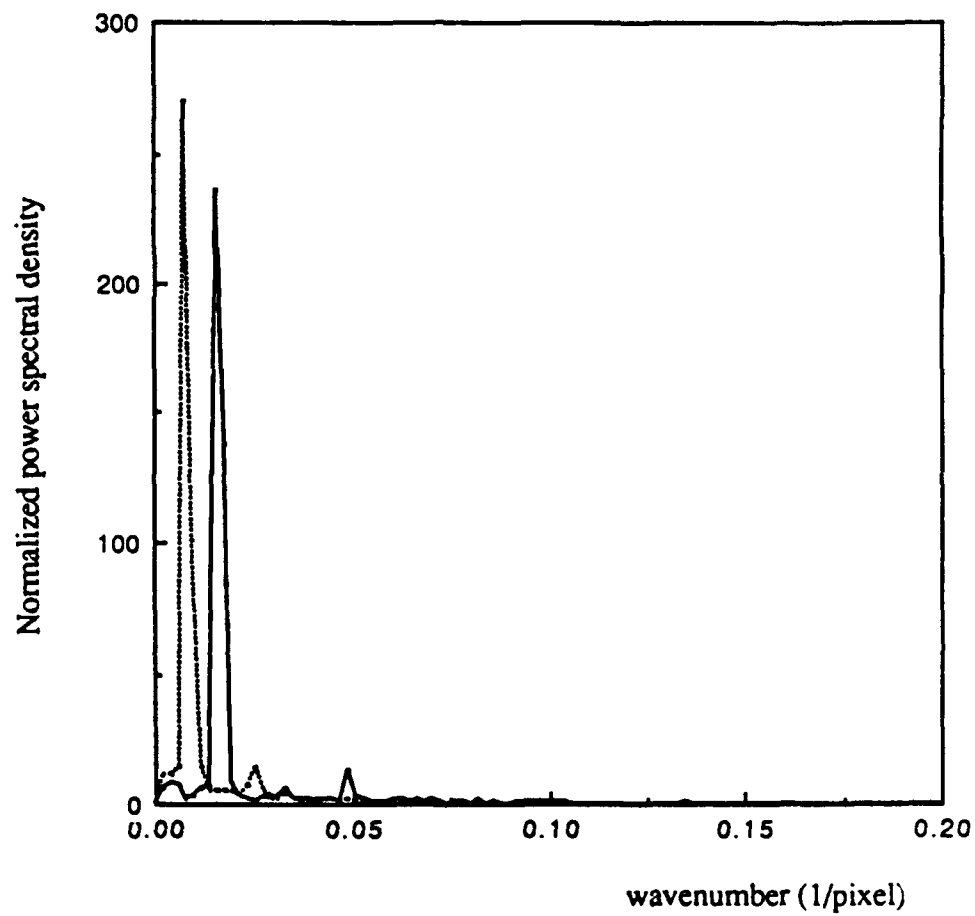


Figure 3.12 Power spectral density vs. wavenumber of image after contrast enhancement. \_\_\_\_\_, Horizontal spectrum; ....., Vertical spectrum.

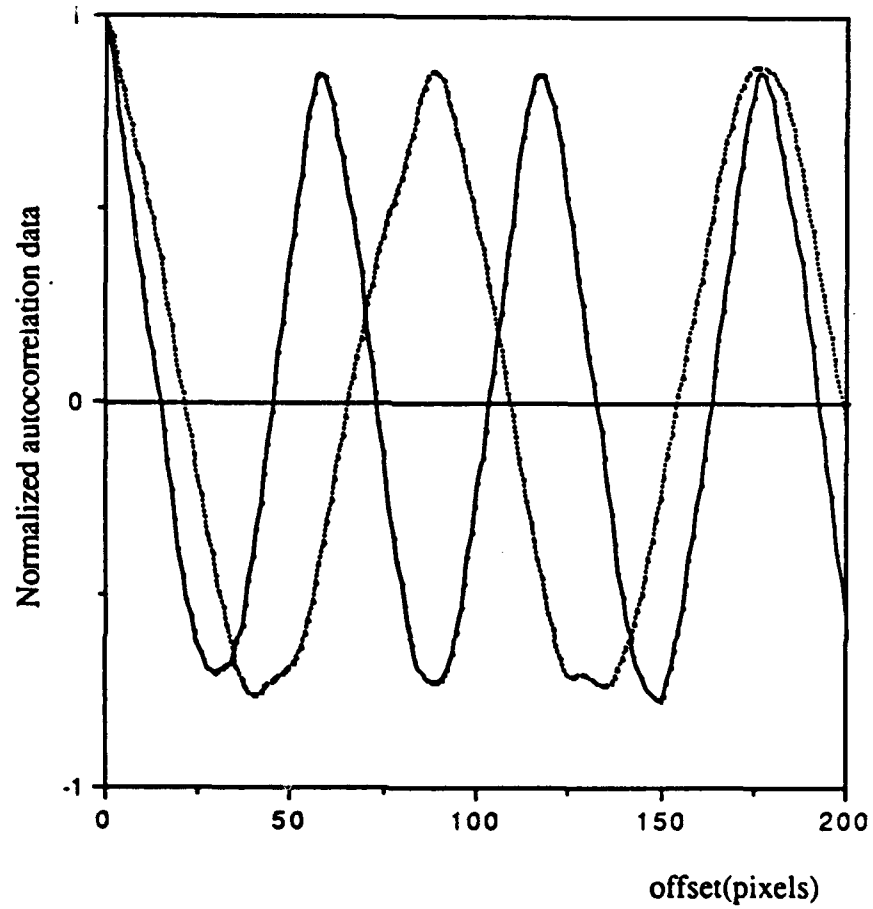


Figure 3.13 Autocorrelation vs. offset for image after contrast enhancement.  
——, Horizontal autocorrelation; ....., Vertical autocorrelation.

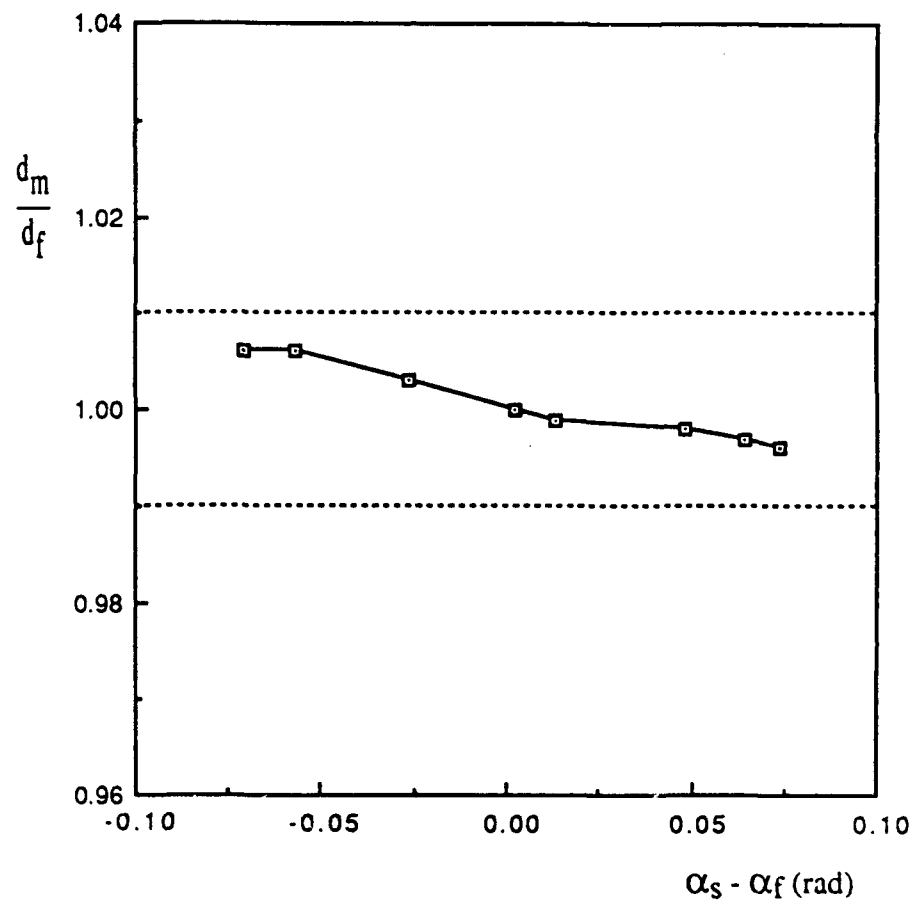


Figure 3.14 Fringe spacing error as a function of initial expected fringe angle.  
..... ;  $\pm 1\%$  error boundary.

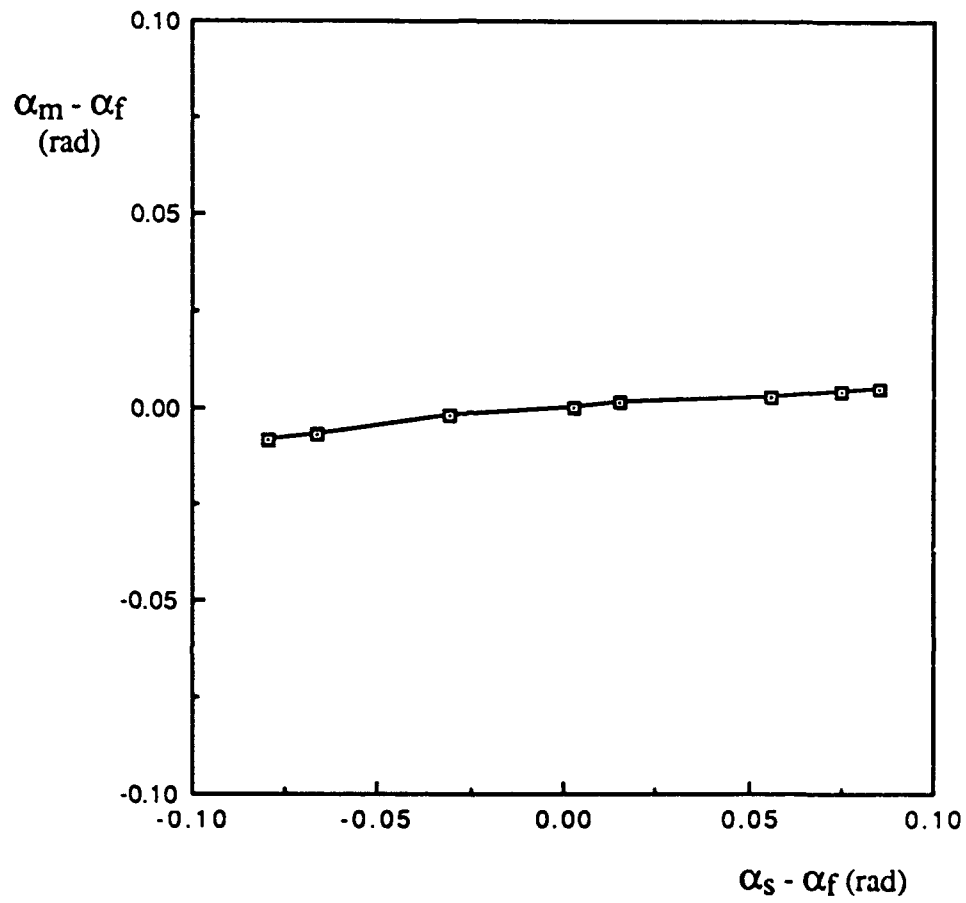


Figure 3.15 Fringe direction error as a function of initial expected fringe angle.

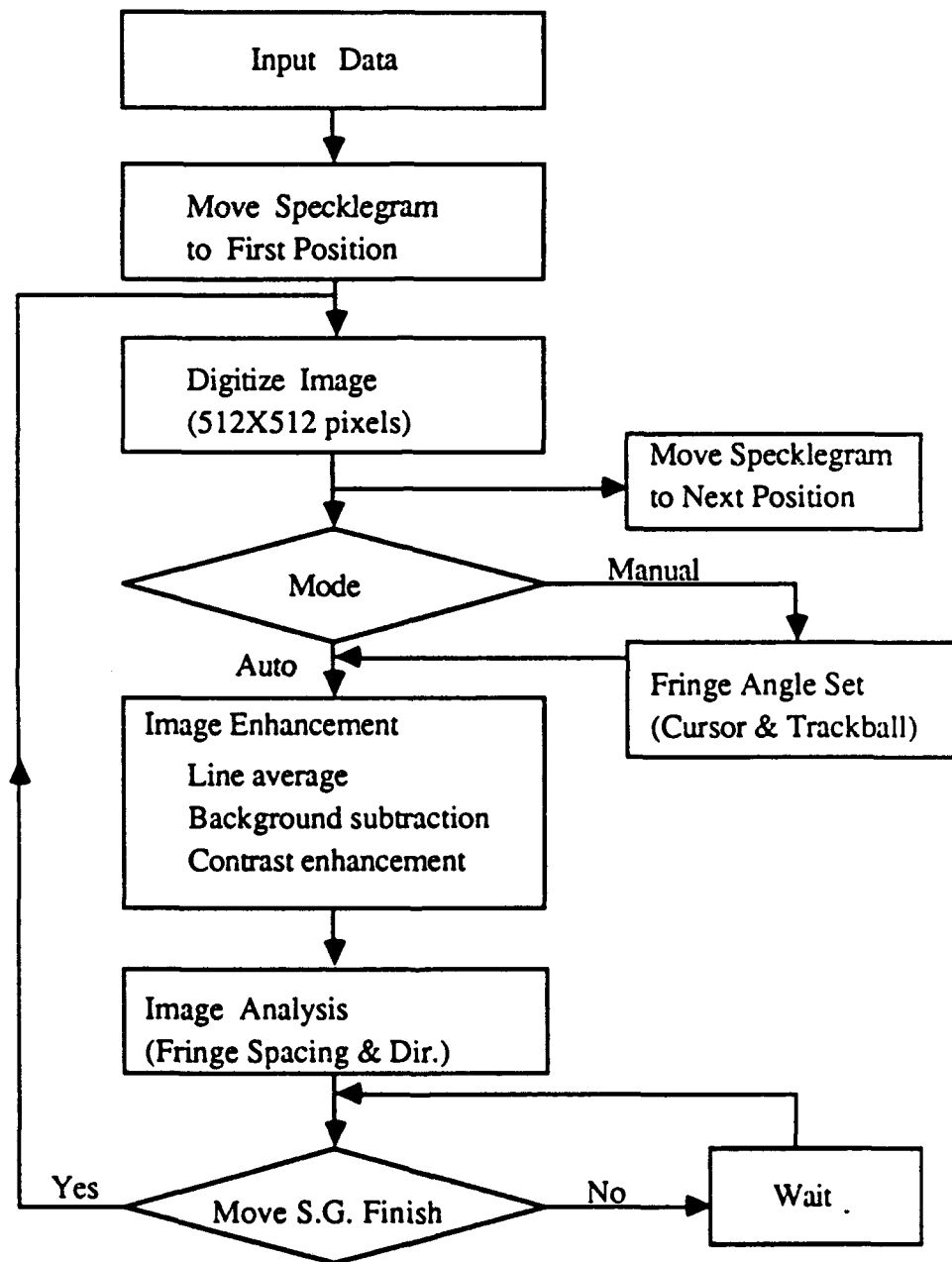


Figure 3.16 Flow chart of digital image processing program.

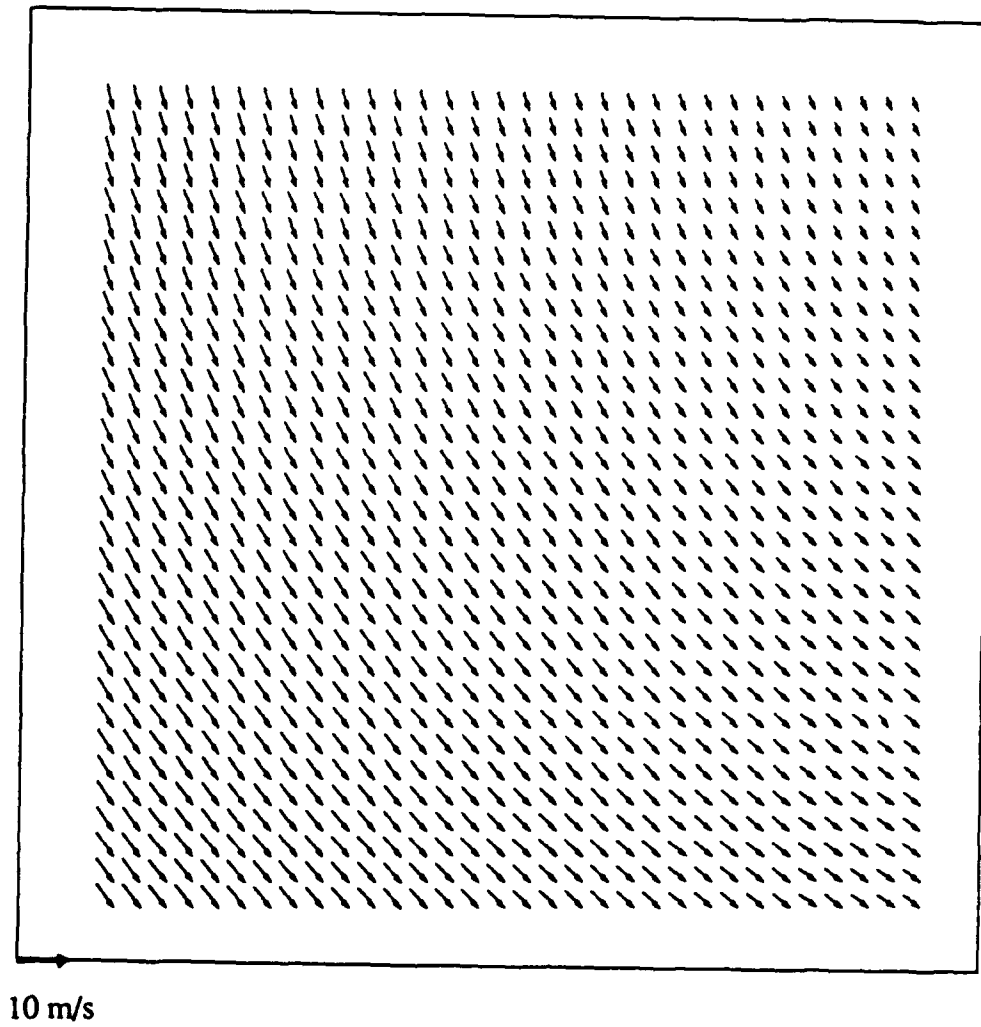


Figure 3.17 Vector plot of the velocity field measured in the rotating disk experiment.

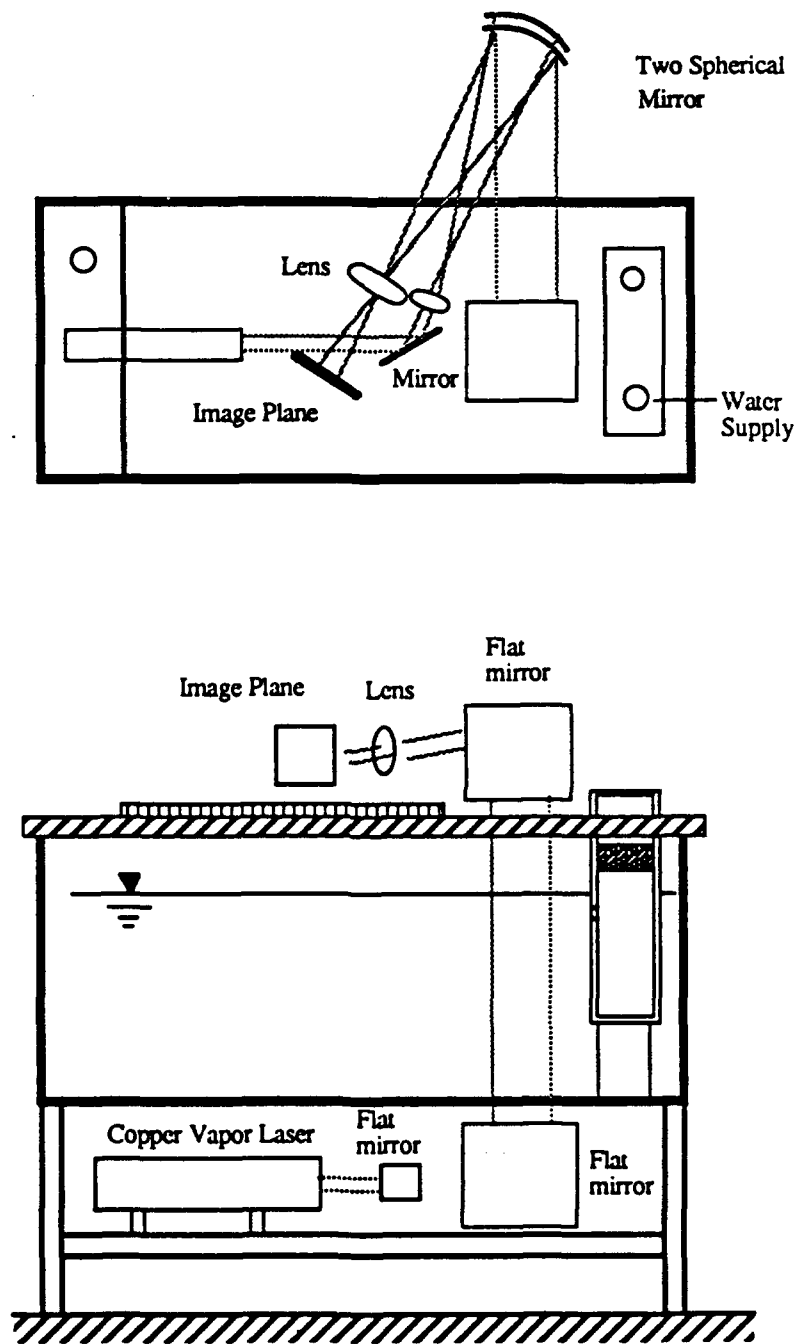


Figure 3.18 Schematic diagram of CVL free surface imaging system.



Figure 3.19 Photograph of the microballoons. Scale: full width 1mm.

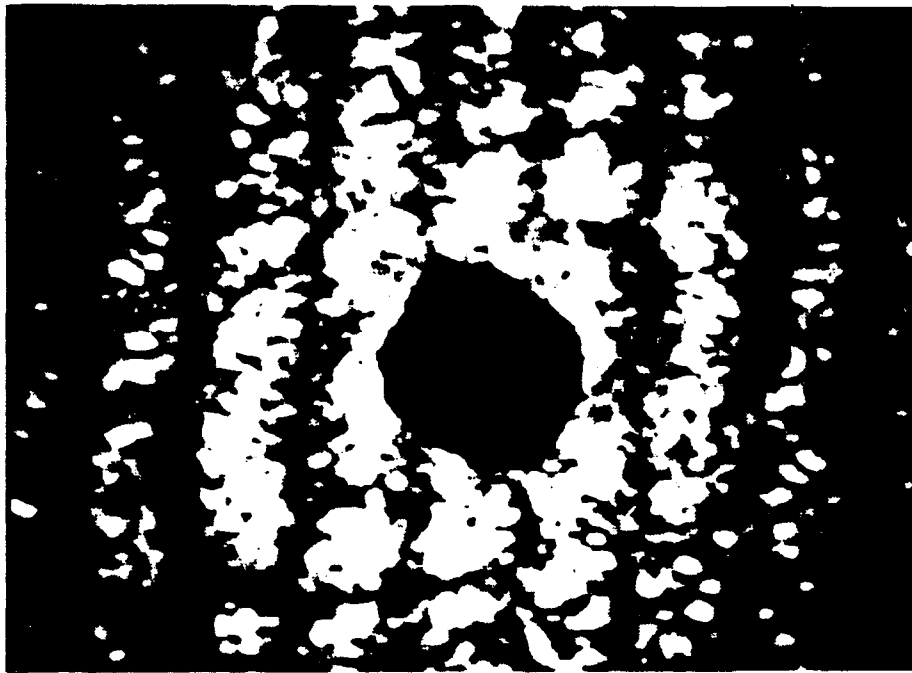


Figure 3.20 Fringe image obtained with the surface imaging optical system.

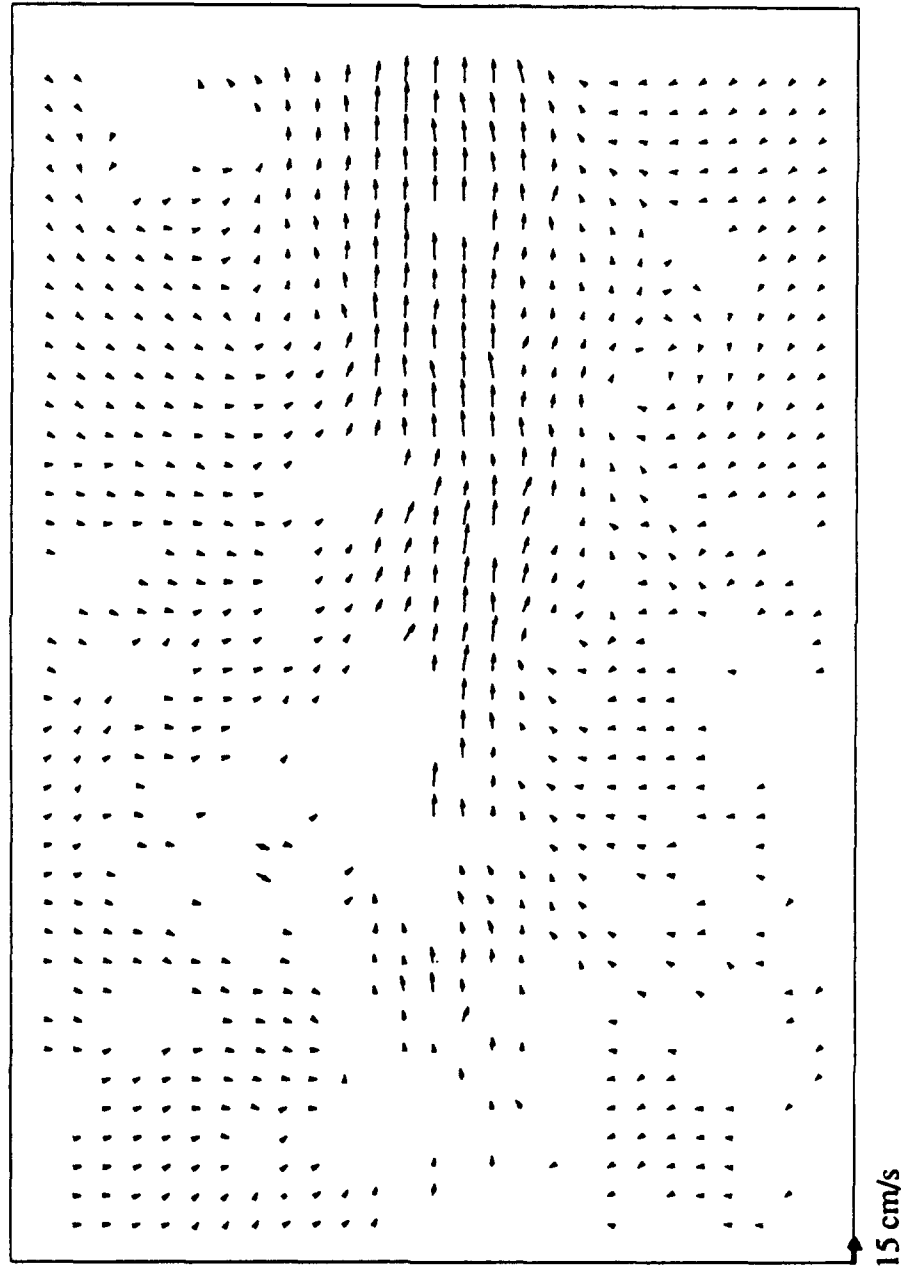


Figure 3.21 Vector plot of the velocity field at the free surface. Jet depth  $h/D_0 = 1.0$ .  
 Jet exit velocity 25 cm/s. Framed area corresponds to  $2 < x/D_0 < 9$  and  $-2 < y/D_0 < 2$ .

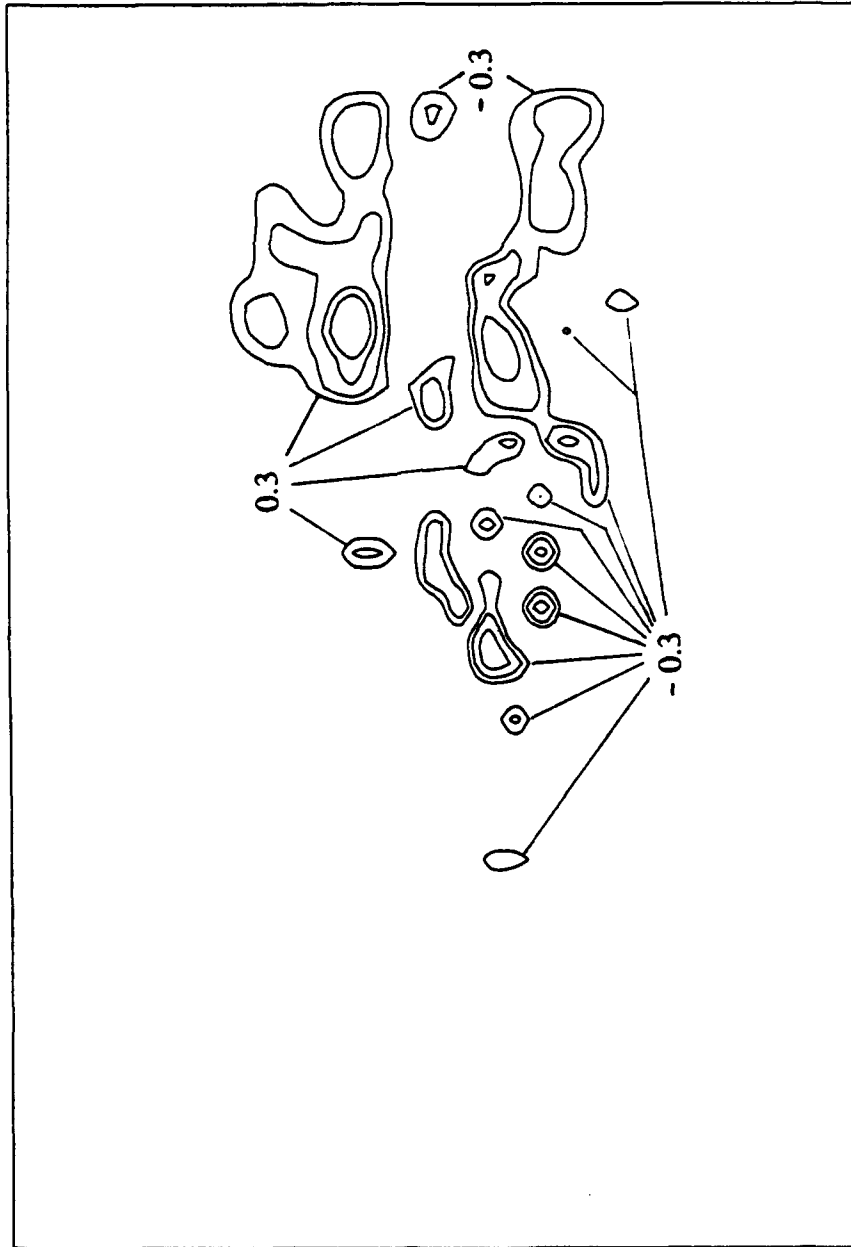


Figure 3.22 Contour plot of the vorticity at the free surface derived from the results plotted in Figure 3.21.  
 Contour values plotted  $\omega D_0 / U_e = -0.8, -0.5, -0.3, 0.3, 0.5, 0.8, 1$ .

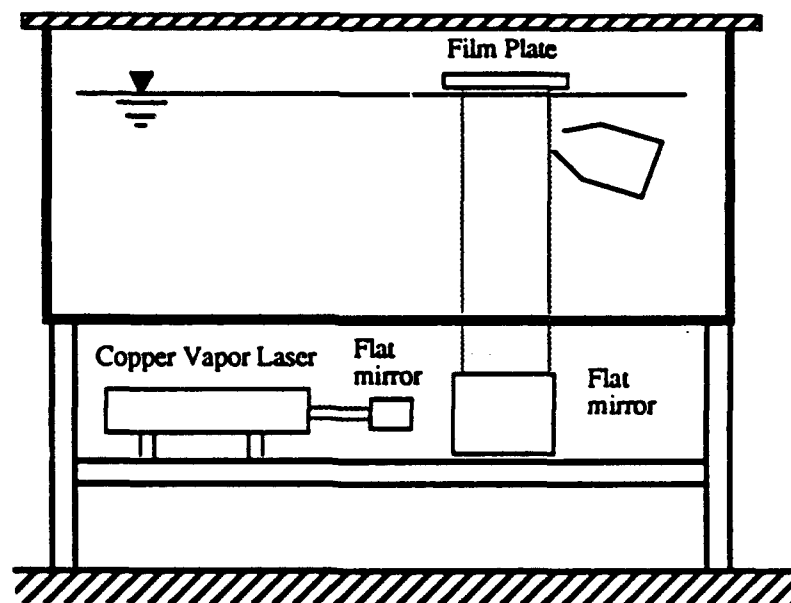
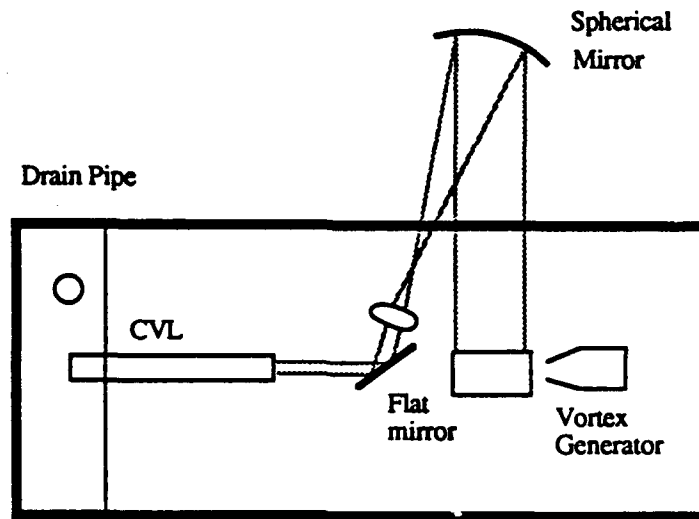


Figure 3.23 Schematic diagram of CVL shadowgraph system used to obtain the speckle photographs.

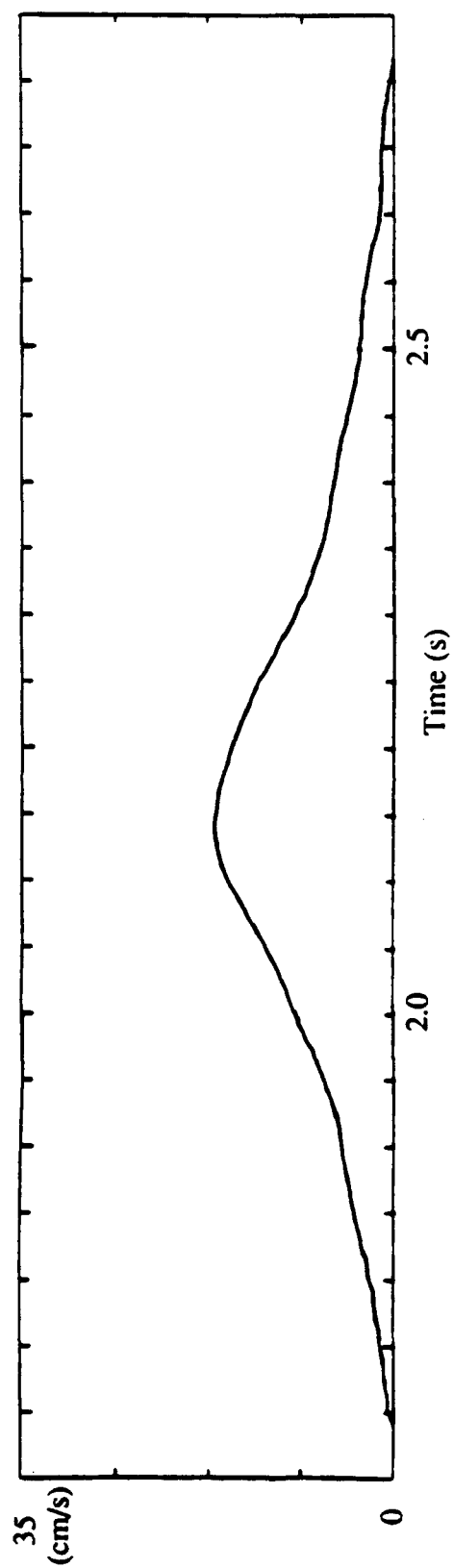


Figure 4.1 Velocity trace measured on the centerline at  $X/D_0 = 5$  for  $\Gamma = 64 \text{ cm}^2/\text{s}$ .

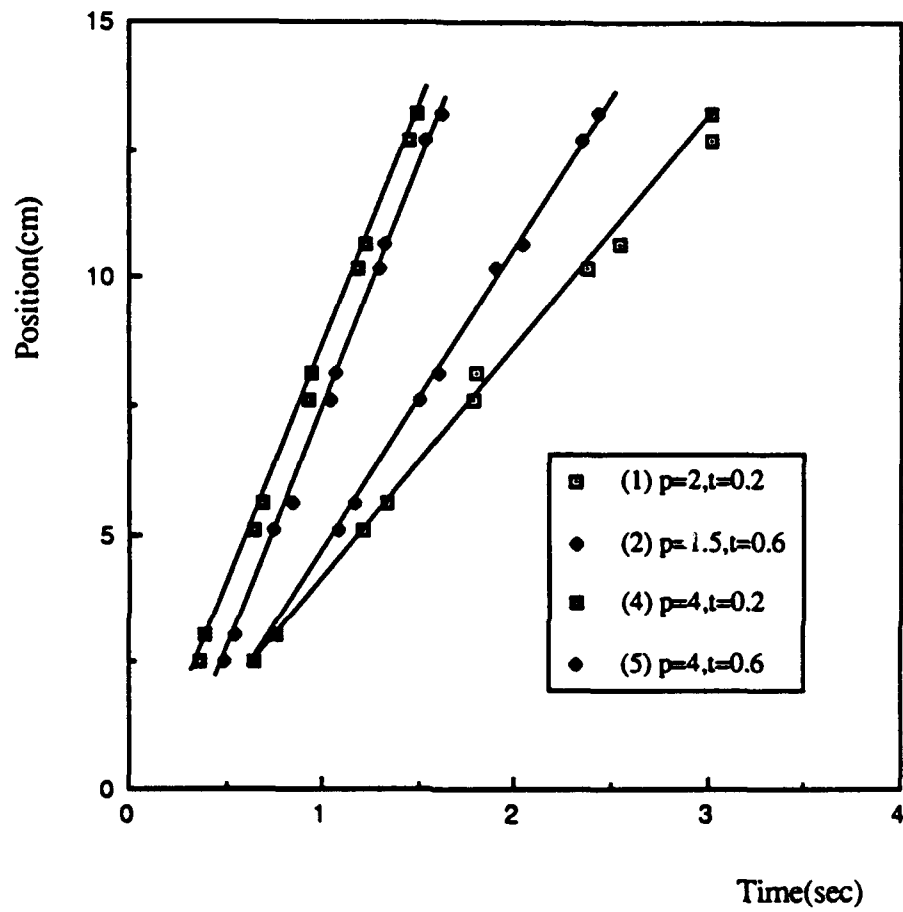


Figure 4.2 Measured vortex ring position as a function of time for several generator operating conditions.

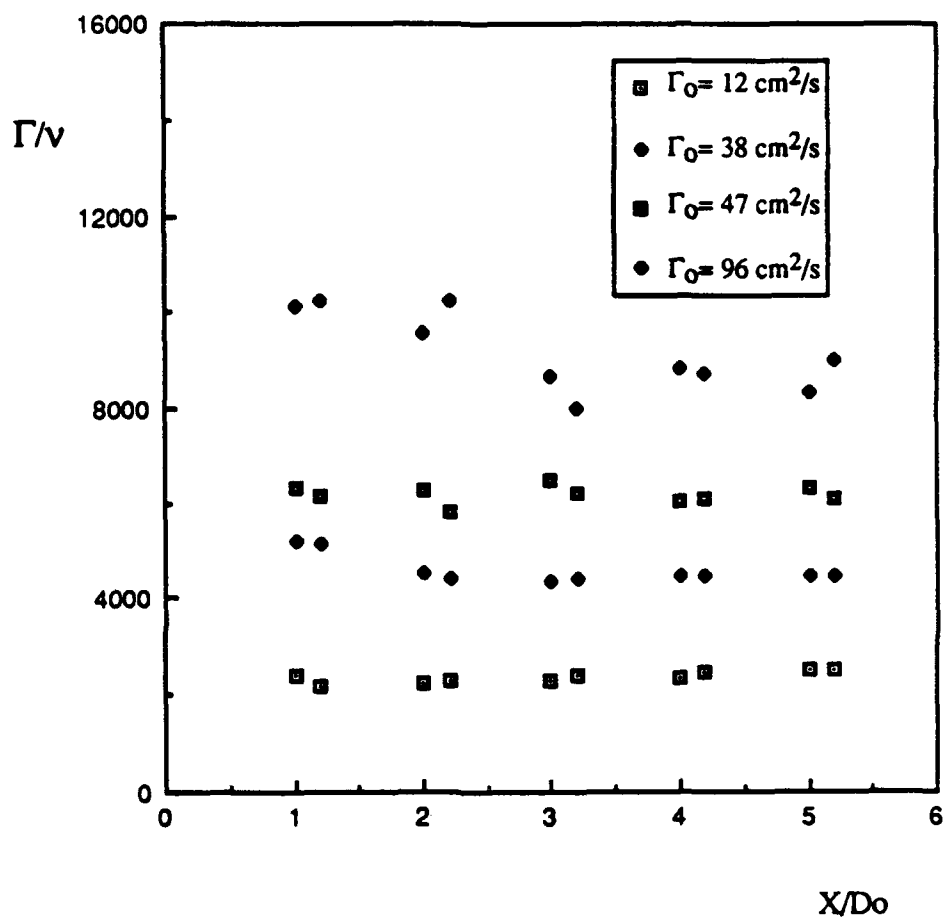


Figure 4.3 Measured Reynolds number as a function of nondimensional downstream position for several generator operating conditions.

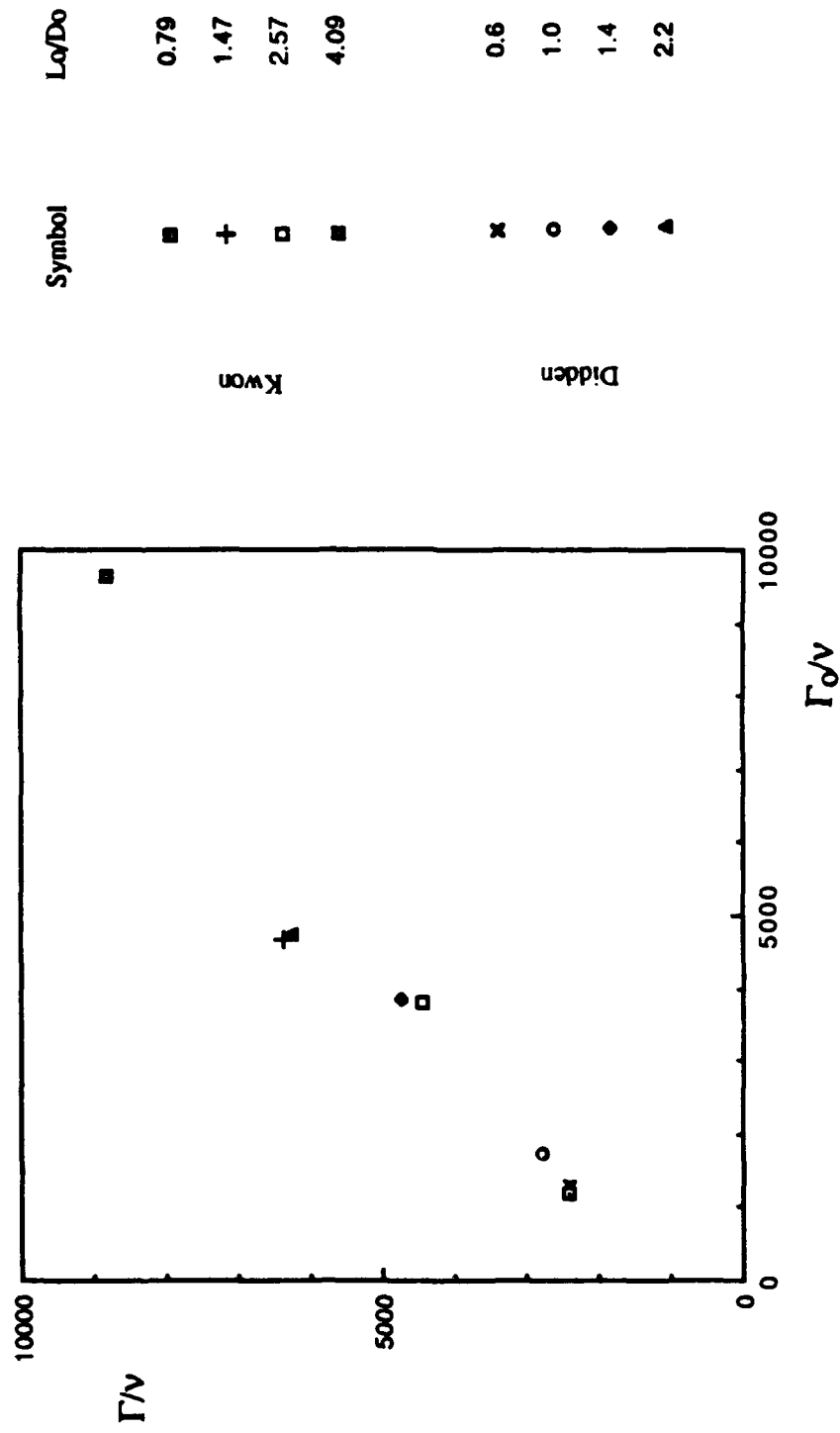


Figure 1.4 Measured Reynolds number after vortex ring formation vs. measured Reynolds number at the exit.

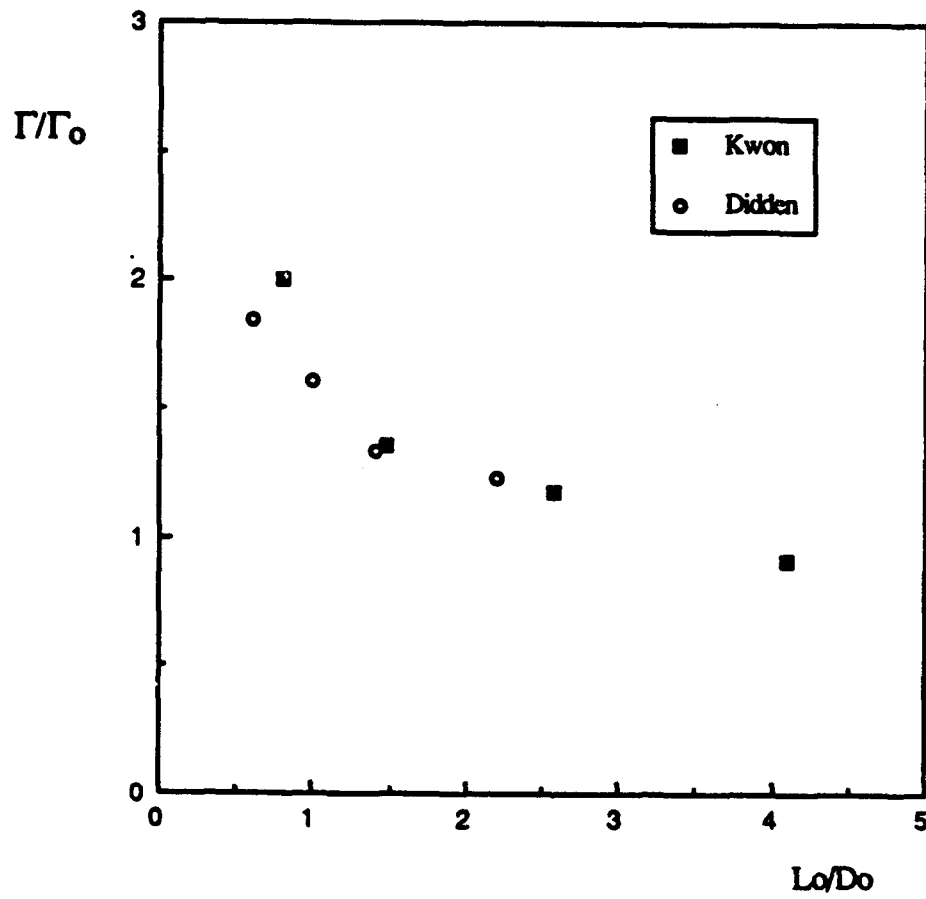


Figure 4.5 Circulation ratio as a function of slug length.

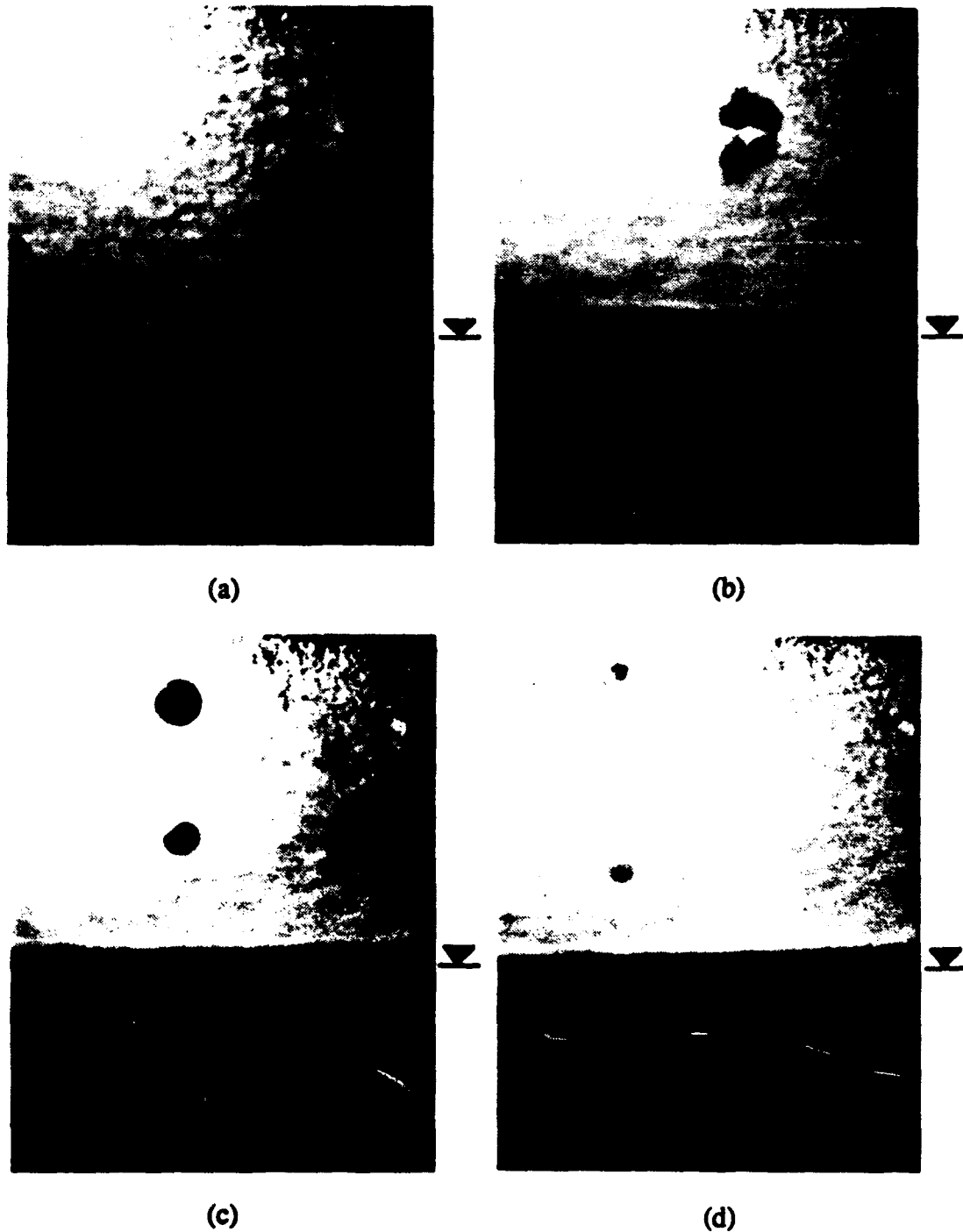


Figure 4.6 Sequence of photographs showing simultaneous views of the vortex ring evolution: (a)  $\Gamma_0/a^2=5$ , (b)  $\Gamma_0/a^2=13$ , (c)  $\Gamma_0/a^2=20$ , (d)  $\Gamma_0/a^2=25$ ,  $\alpha = 0^\circ$ , contaminated surface.

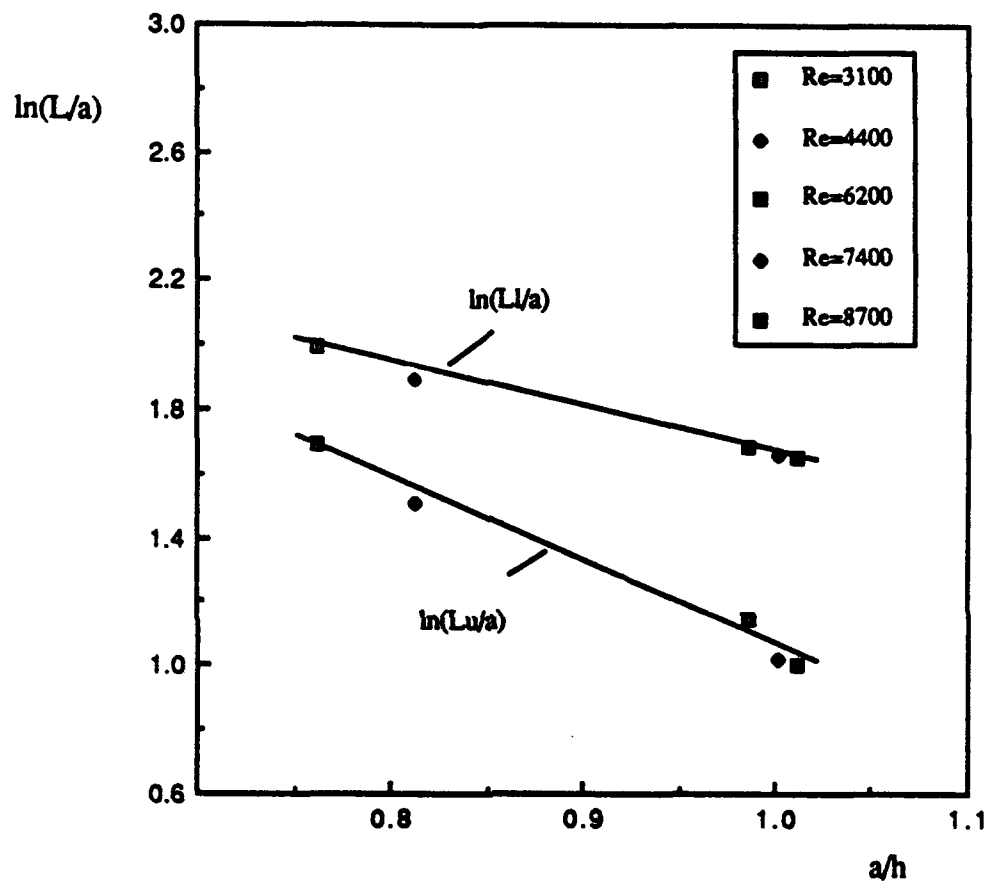


Figure 4.7 Effect of depth on the extent of interaction for vortex rings formed at an incidence angle  $\alpha = 0^\circ$  ; Contaminated surface.

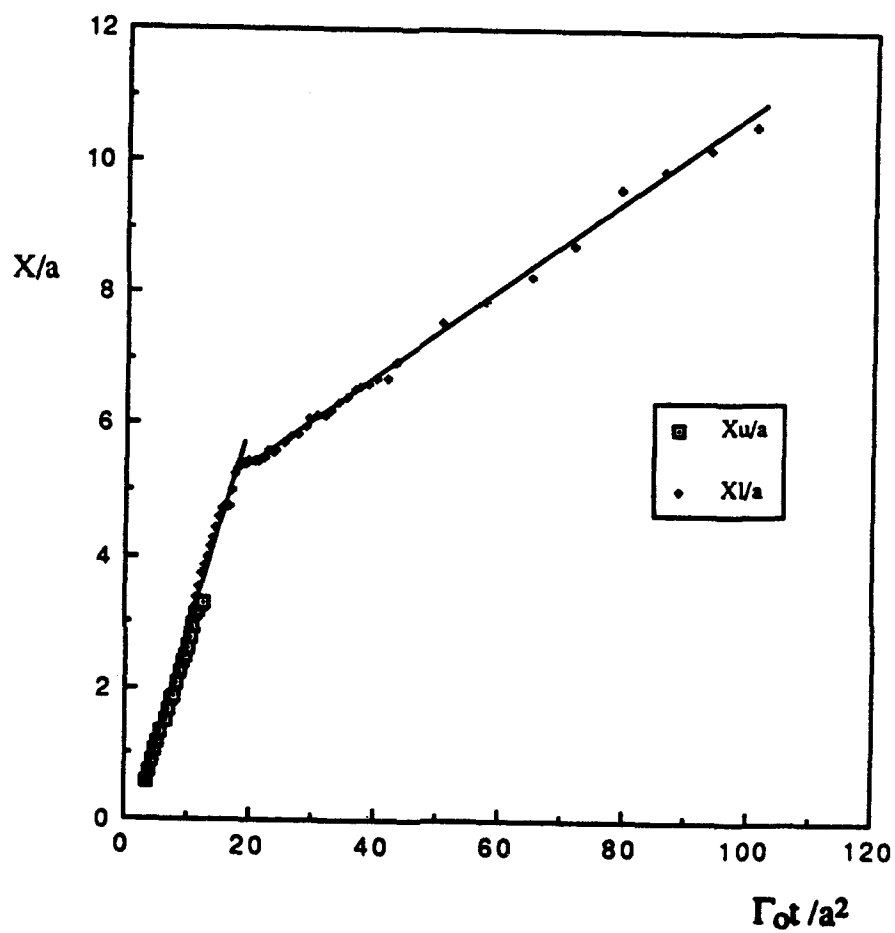


Figure 4.8 Downstream location of vortex cores as a function of time for a contaminated surface.  $\alpha = 0^\circ$

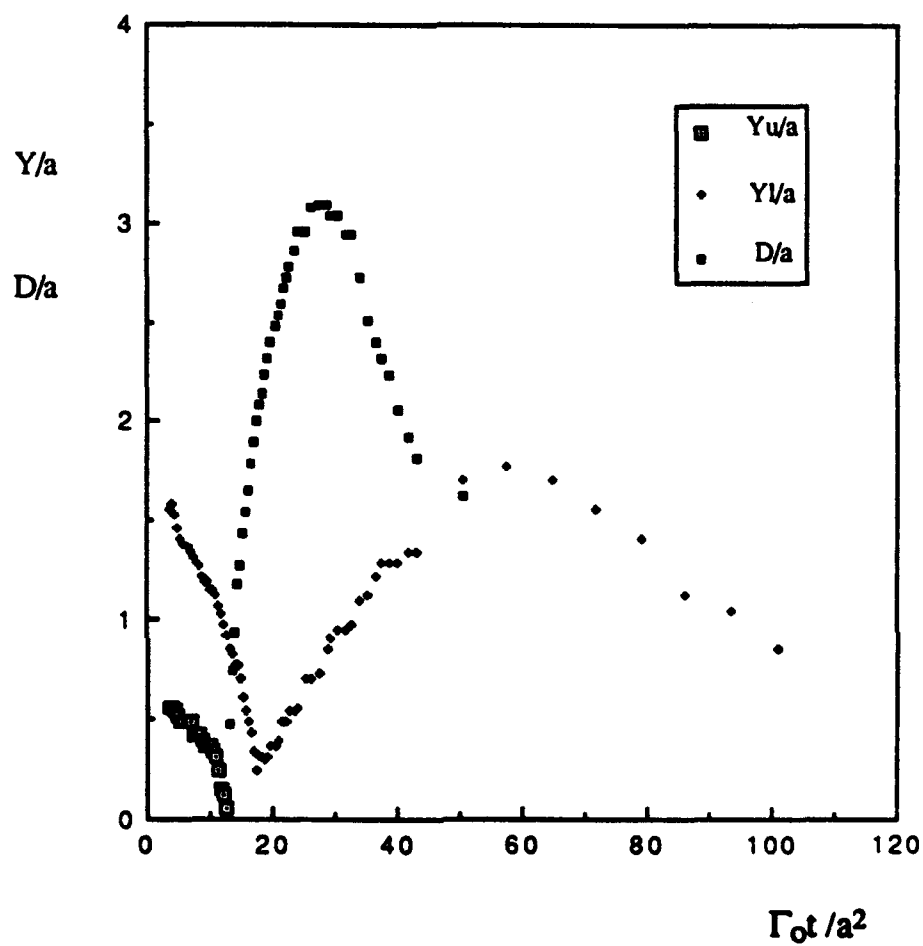


Figure 4.9 Distance of vortex core to the free surface and at the surface as a function of time for a contaminated surface  $\alpha = 0^\circ$

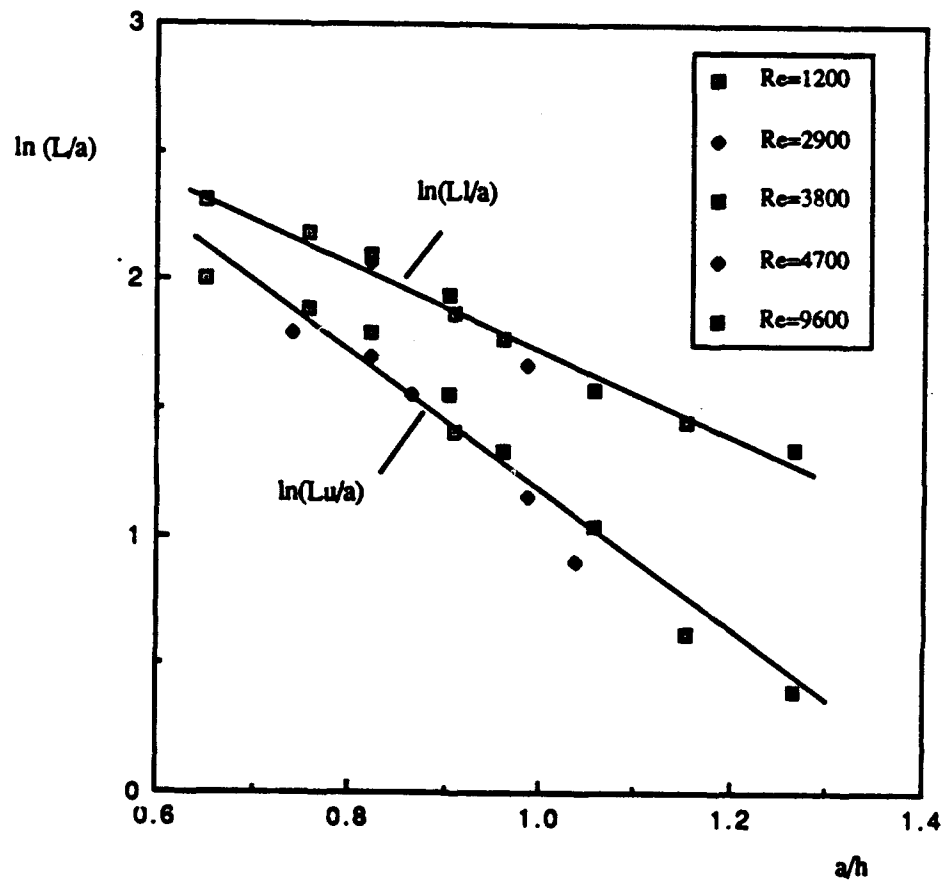


Figure 4.10 Effect of depth on the extent of interaction for vortex rings formed at an incidence angle  $\alpha = 0^\circ$ ; Clean surface.

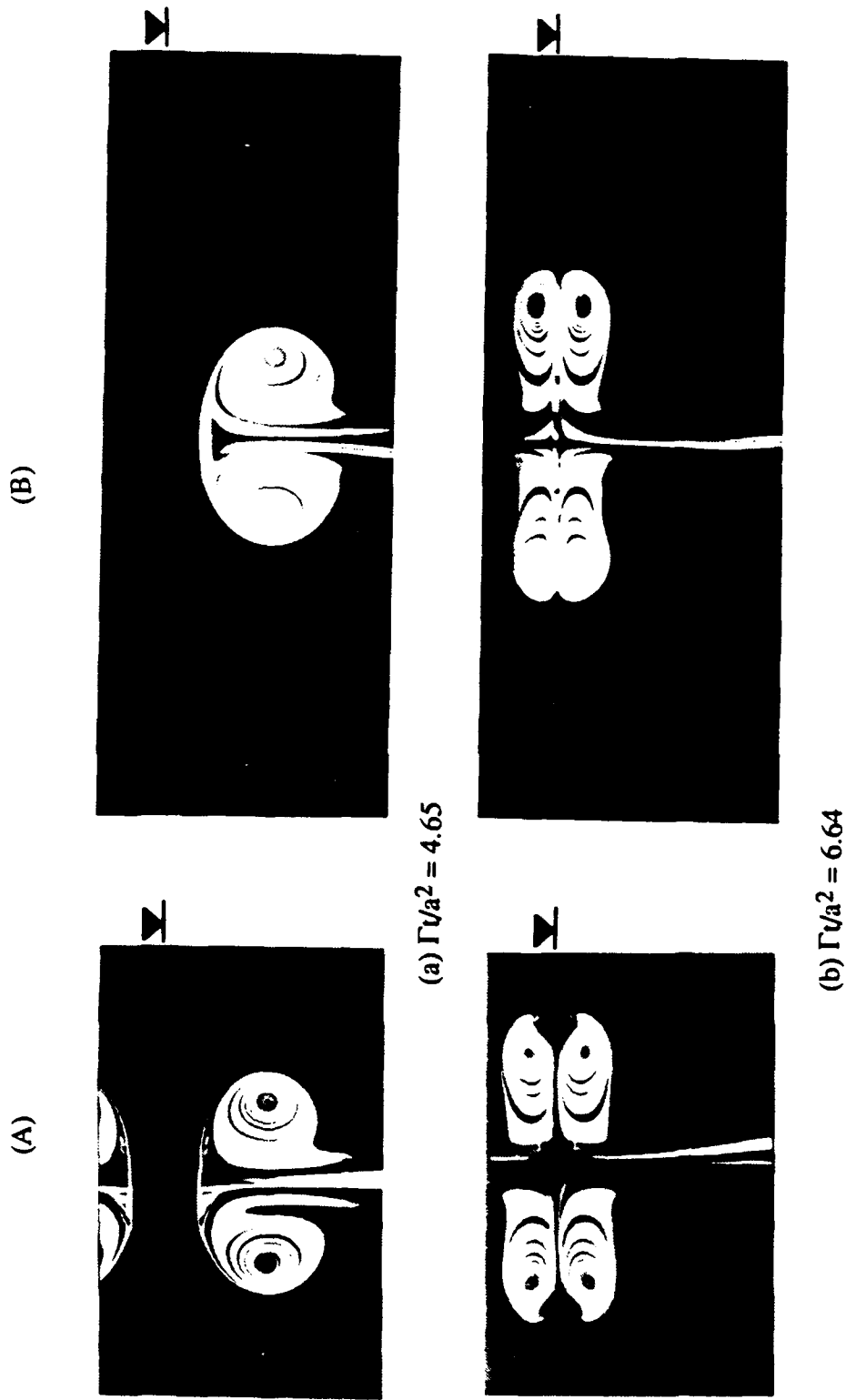


Figure 4.11 Sequence of photographs showing the interaction of a vortex ring with a free surface at an incidence angle  $\alpha = 90^\circ$ . (A) Contaminated surface, (B) Cleaner surface.

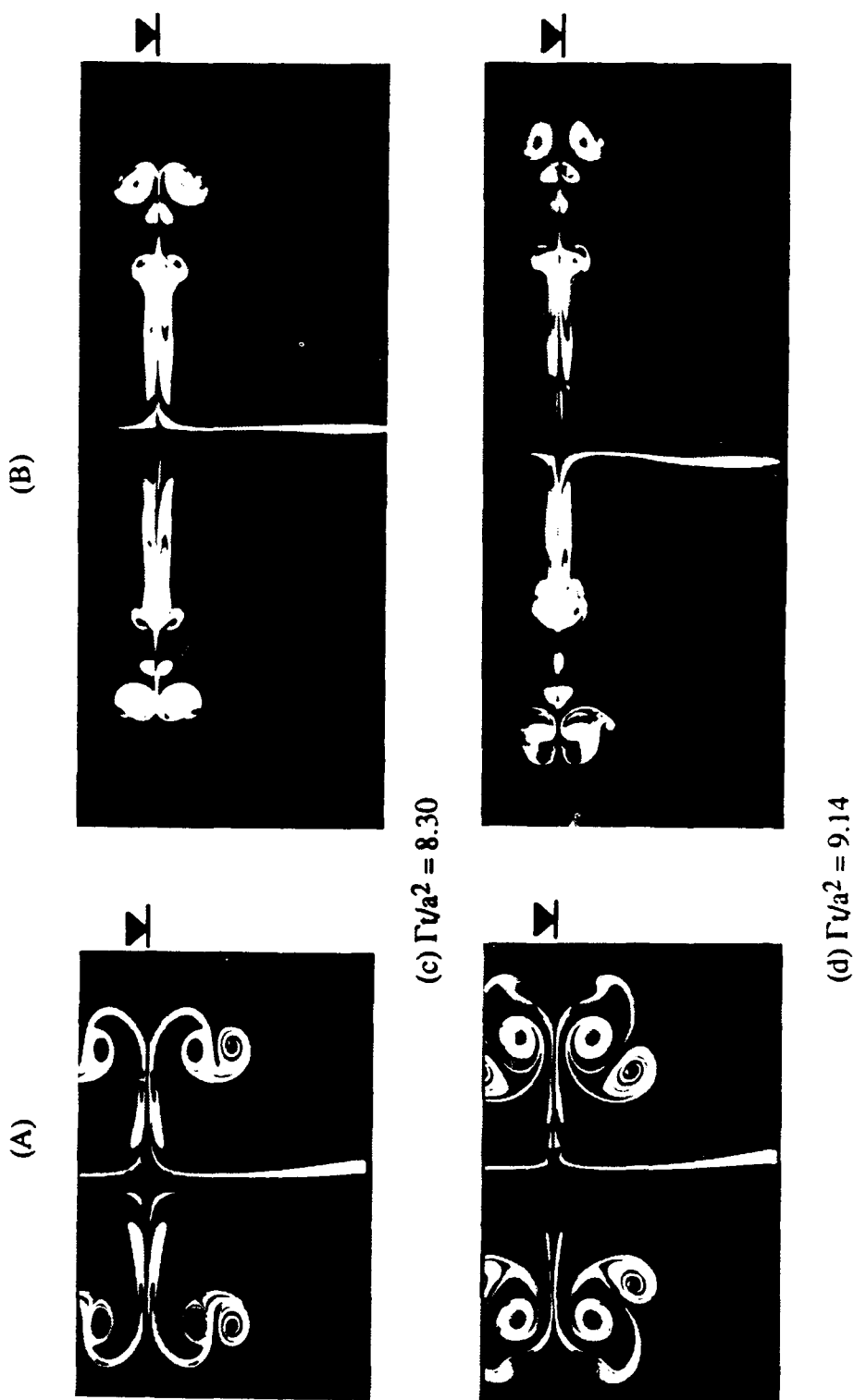


Figure 4.11 Concluded.

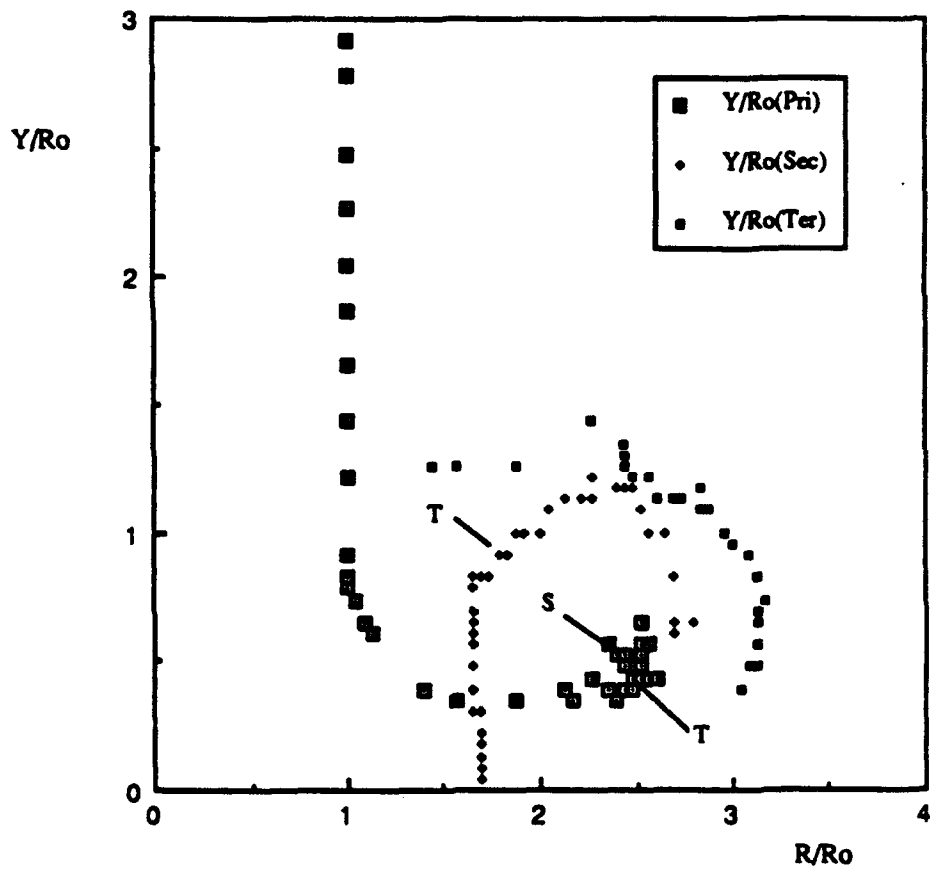


Figure 4.12 Trajectory of vortex core for the contaminated free surface. ( $\alpha = 90^\circ$ )  
 S: Location of primary vortex when secondary vortex is first observed.  
 T: Location of primary and secondary vortex when tertiary vortex is first observed.

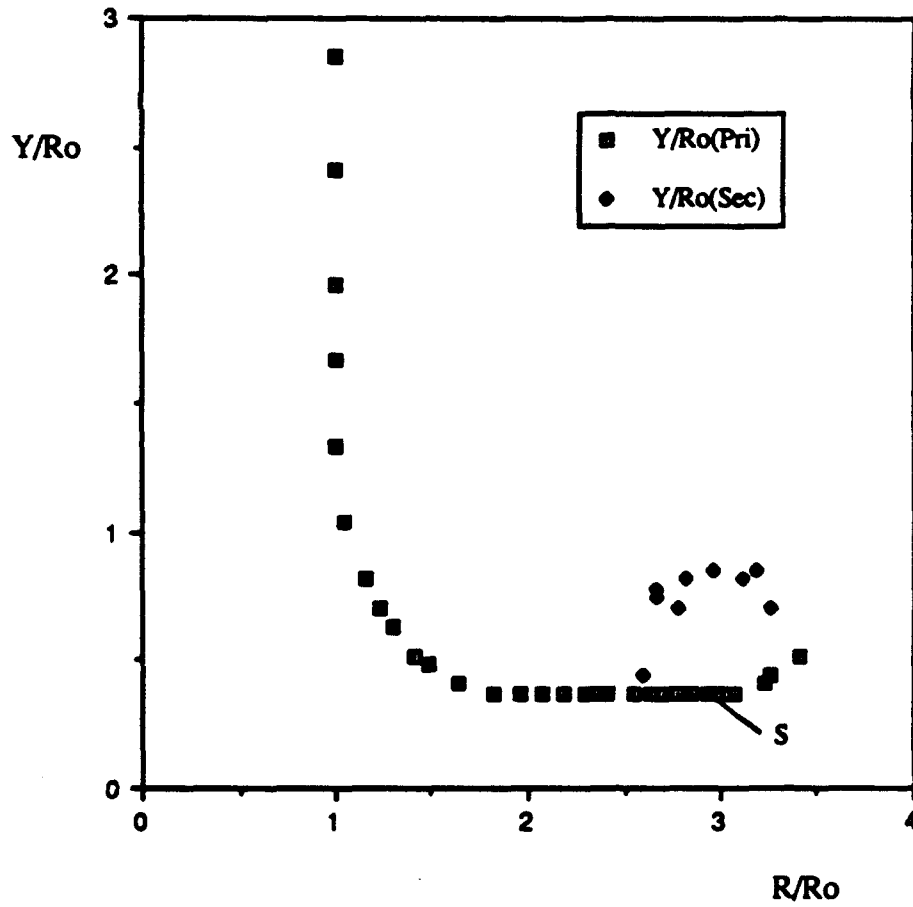


Figure 4.13 Trajectory of vortex core for the cleaner free surface. ( $\alpha = 90^\circ$ )  
 S: Location of primary vortex when secondary vortex is first observed.

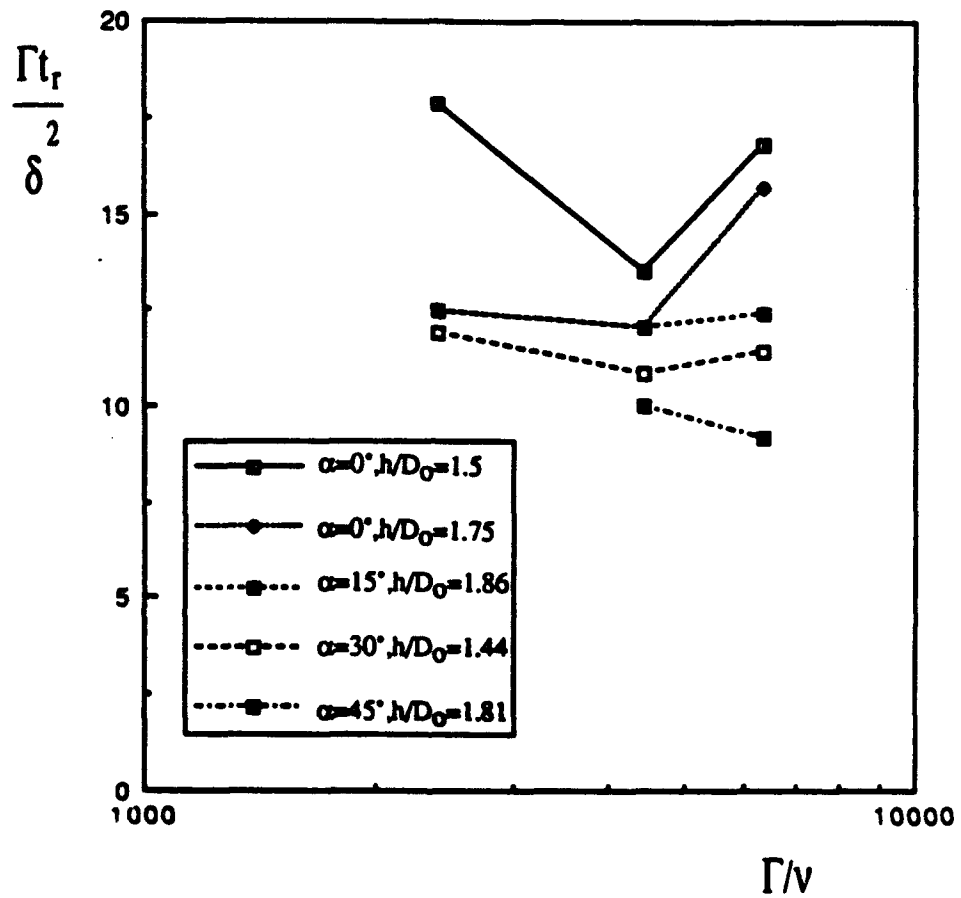


Figure 4.14 Nondimensional reconnection time as a function of Reynolds number for several incidence angles  $\alpha$  and depth  $h/D_0$ .

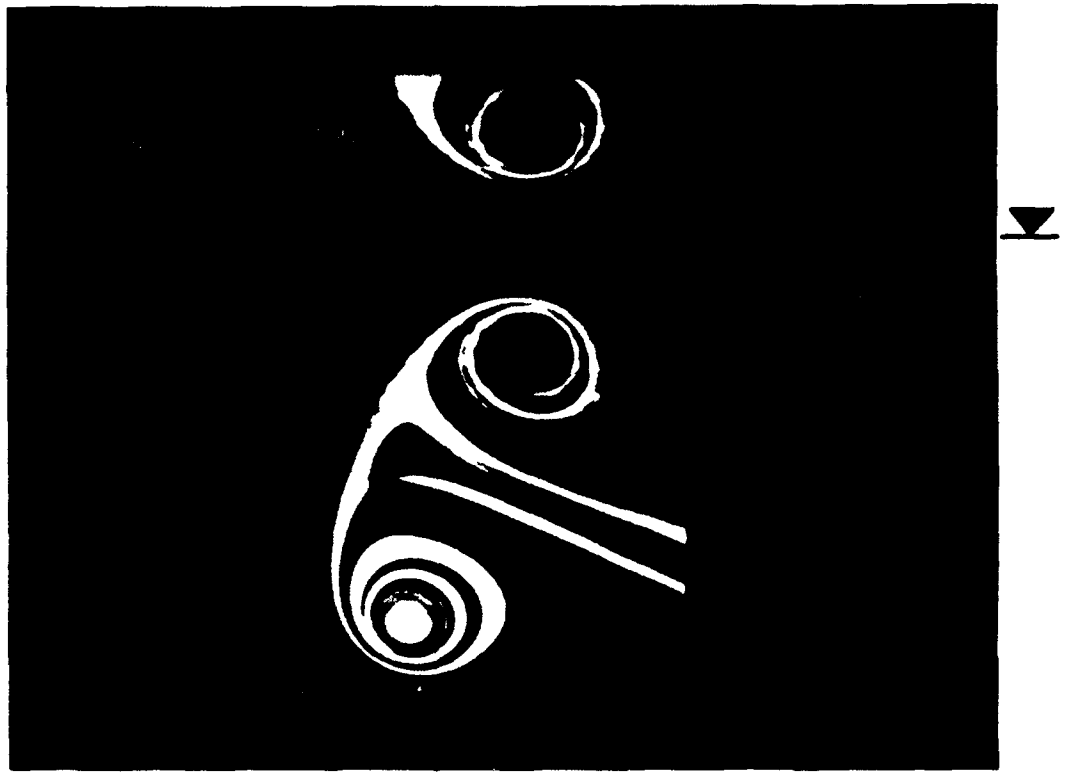


Figure 4.15 Cross-section view photograph of a vortex ring before interaction with a free surface.  $\Gamma/\nu = 5000$ ,  $\alpha = 20^\circ$ .

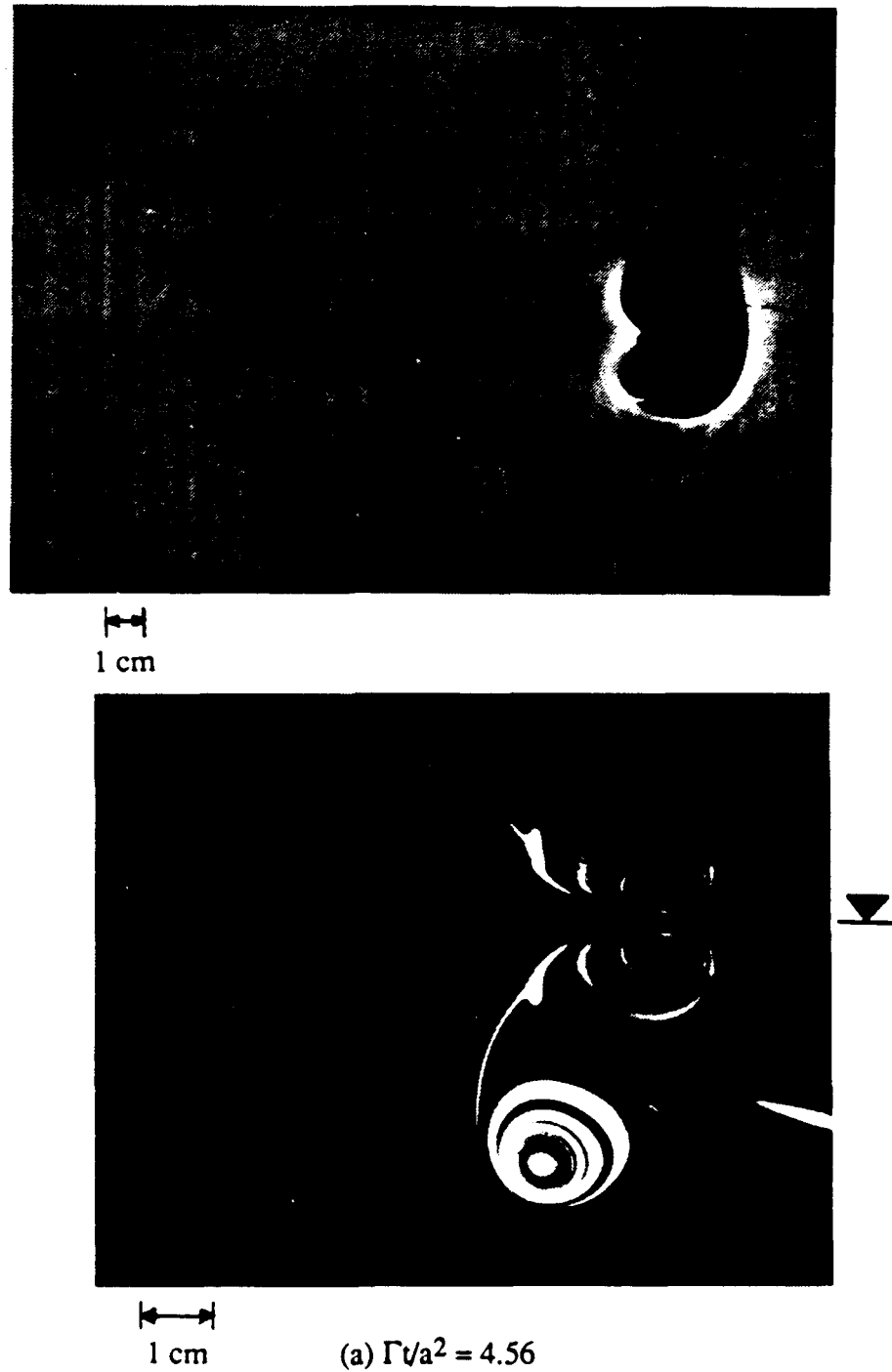
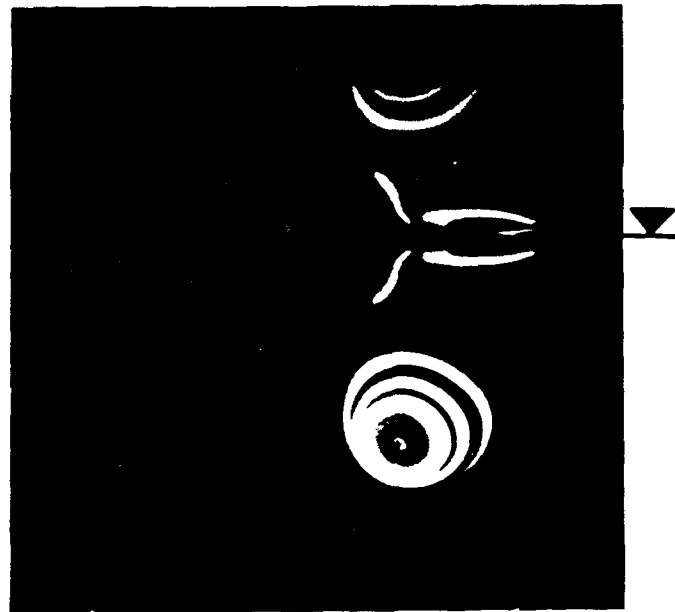
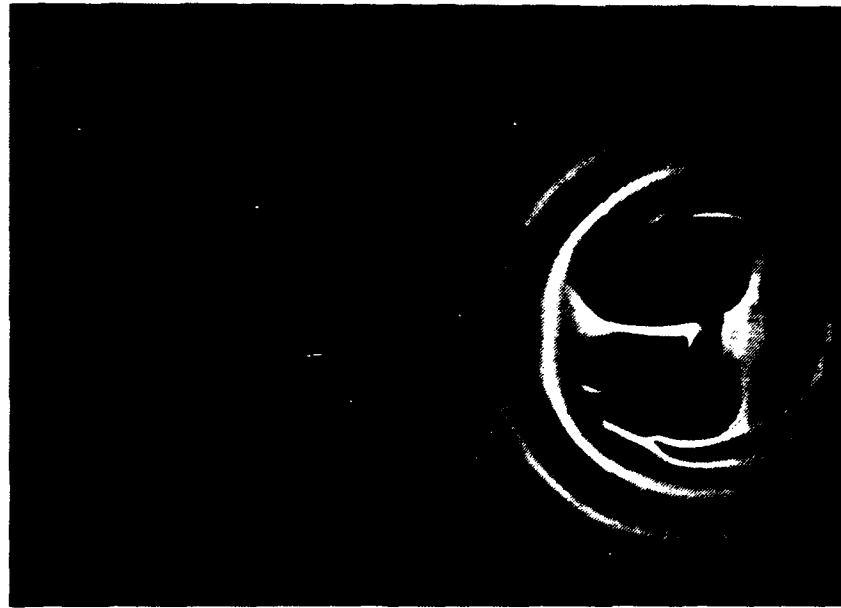
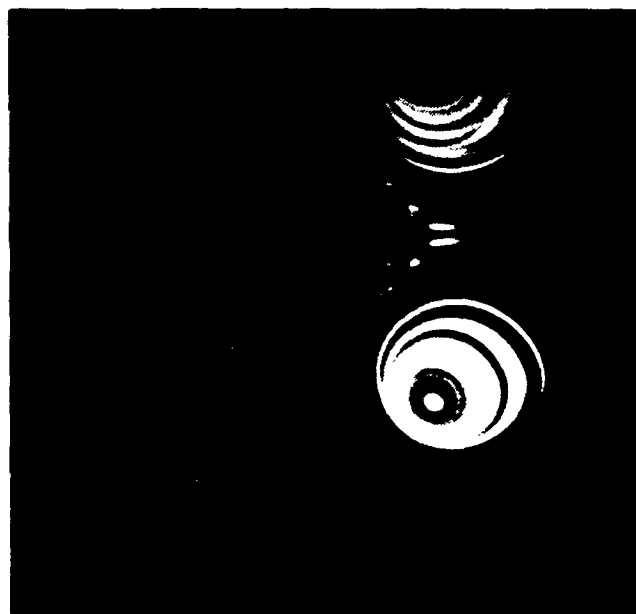


Figure 4.16 Sequence of photographs showing the interaction of a vortex ring with a free surface. Top image : Shadow image of surface deformation. Bottom image : Cross section view.  $\Gamma/v = 5000$ ,  $\alpha = 20^\circ$ .



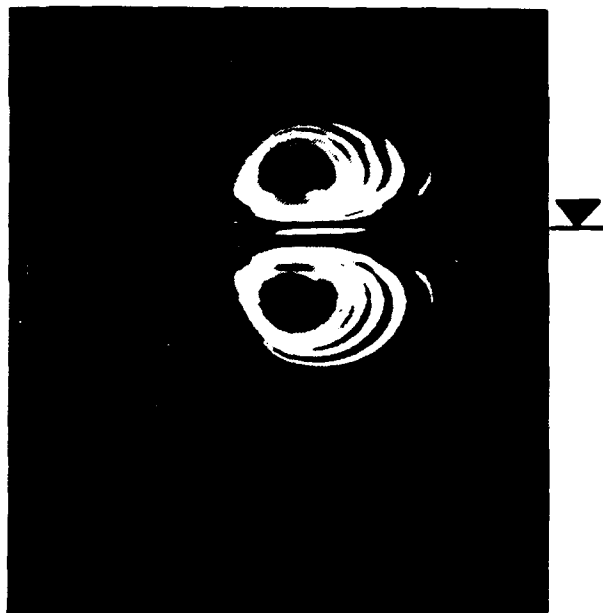
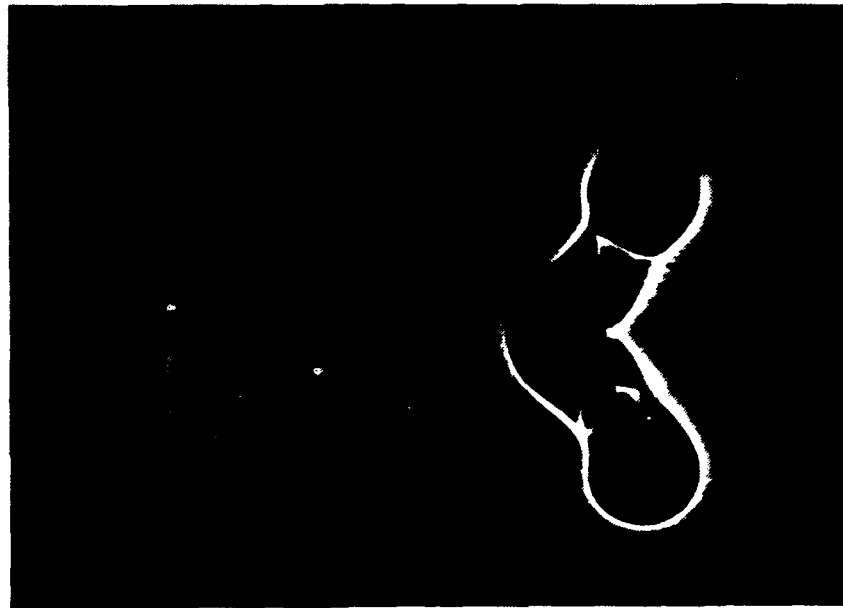
(b)  $\Gamma t/a^2 = 5.57$

Figure 4.16 Continued.



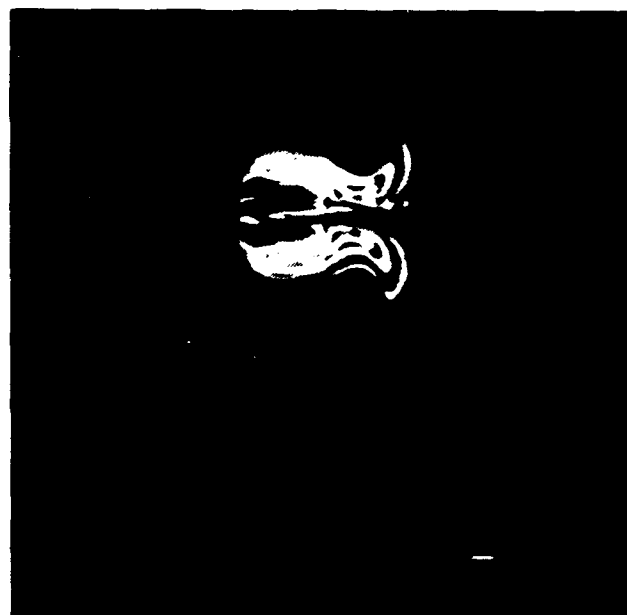
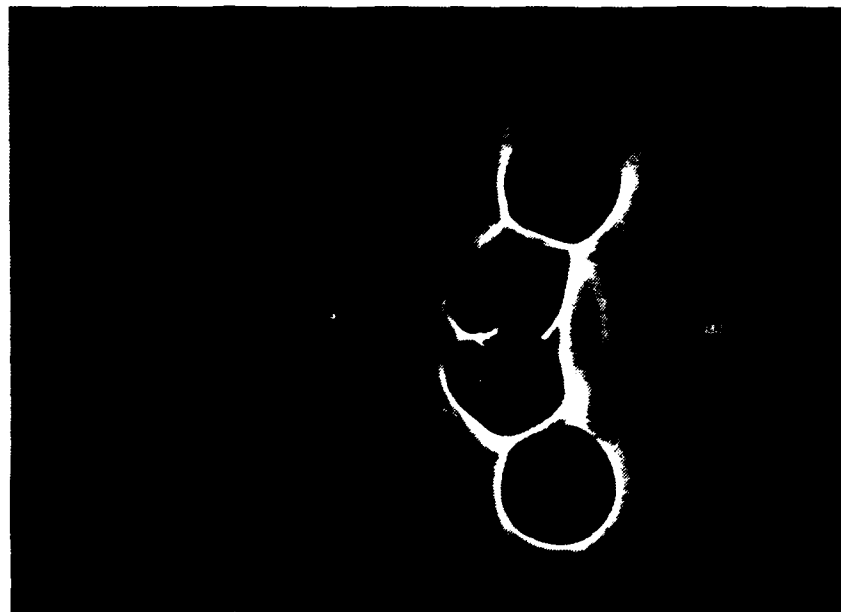
(c)  $\Gamma/a^2 = 6.58$

Figure 4.16 Continued.



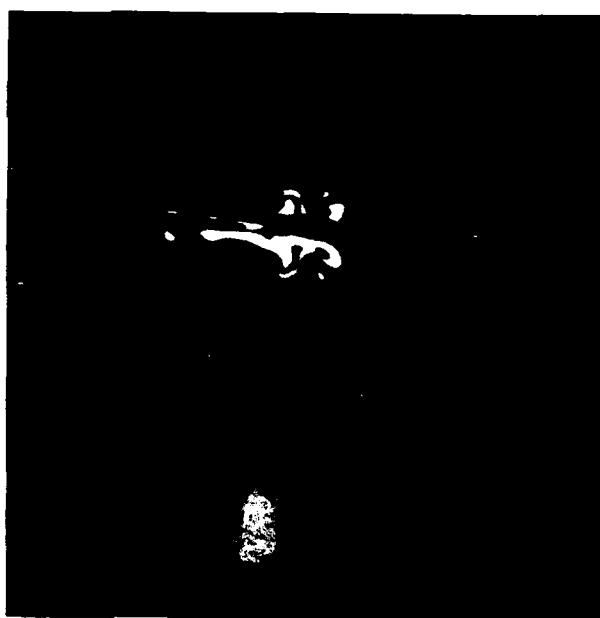
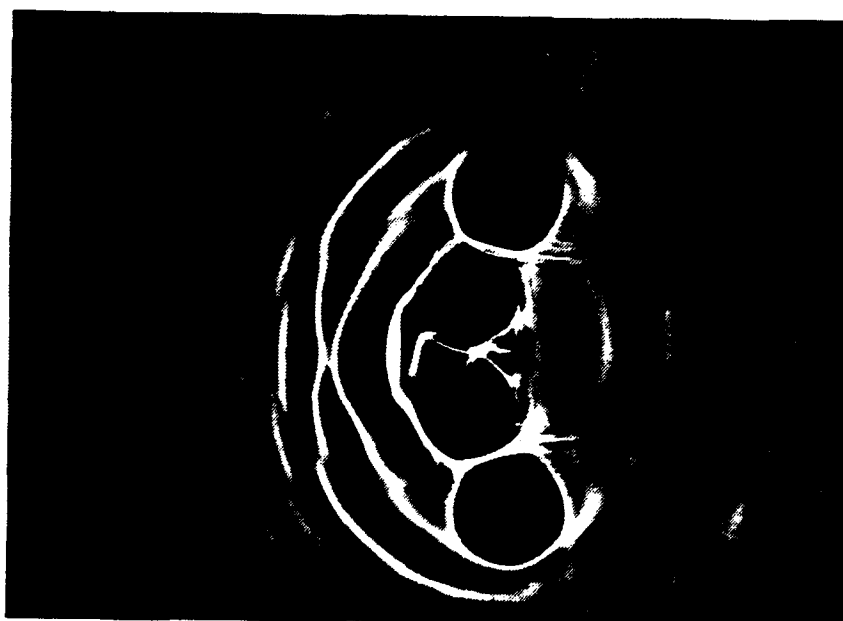
(d)  $\Gamma/a^2 = 7.59$

Figure 4.16 Continued.



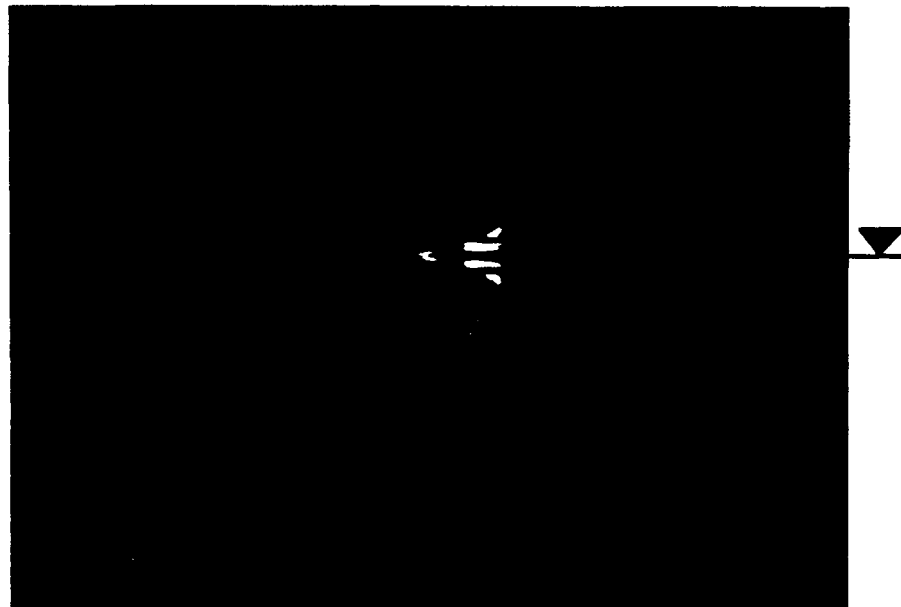
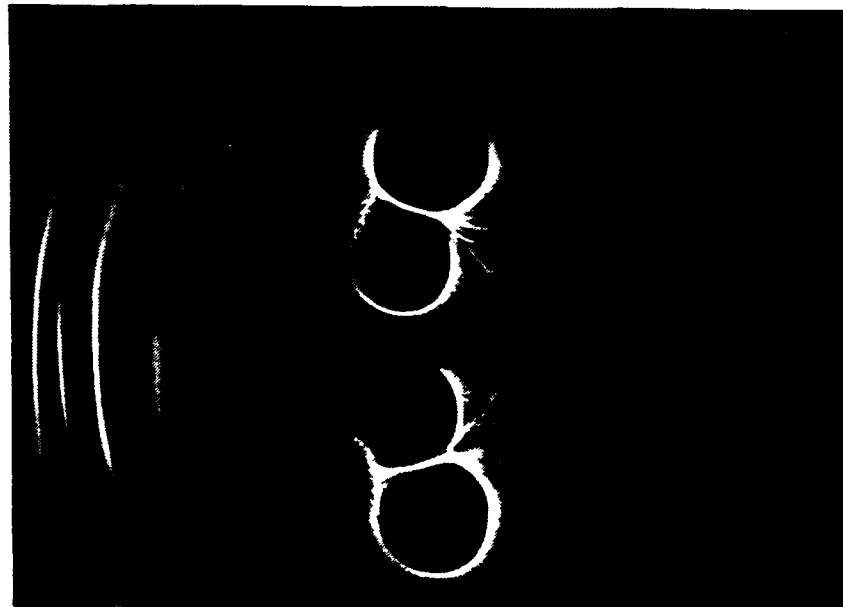
(e)  $\Gamma/a^2 = 8.61$

Figure 4.16 Continued.



(f)  $\Gamma/a^2 = 9.62$

Figure 4.16 Continued.



(g)  $\Gamma v/a^2 = 10.63$

Figure 4.16 Concluded.

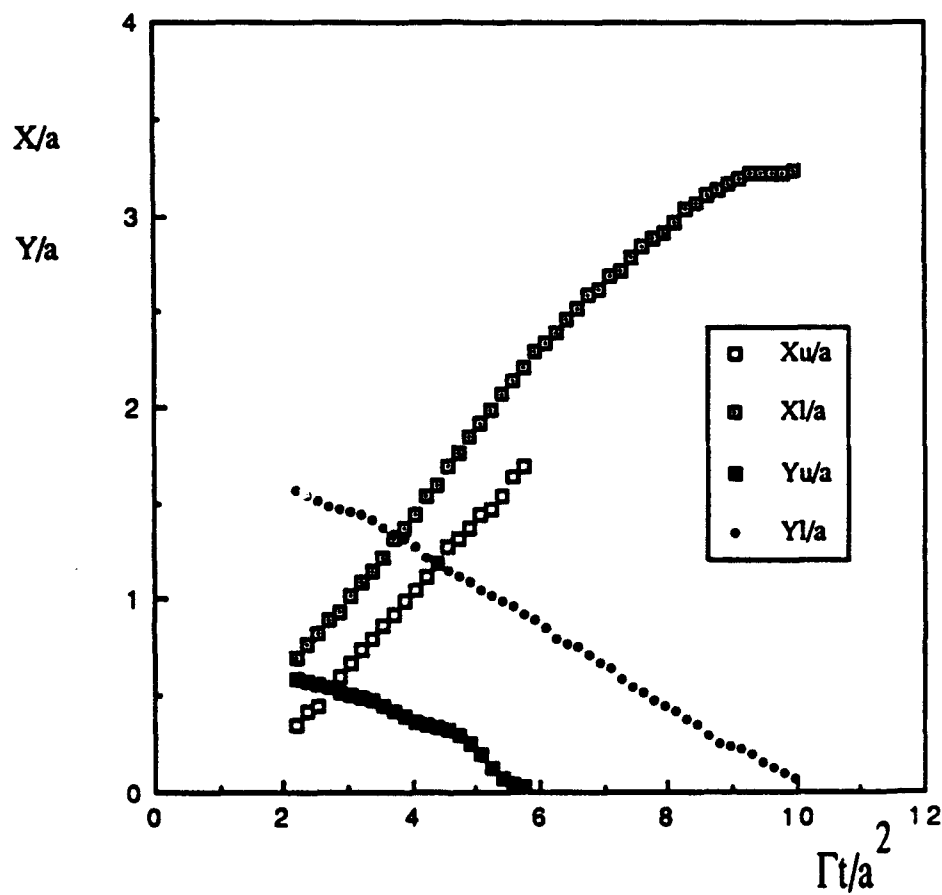


Figure 4.17 Position of vortex cores in cross-section view as a function of time.  
 $\Gamma/\nu = 5000$ ,  $\alpha = 20^\circ$ .

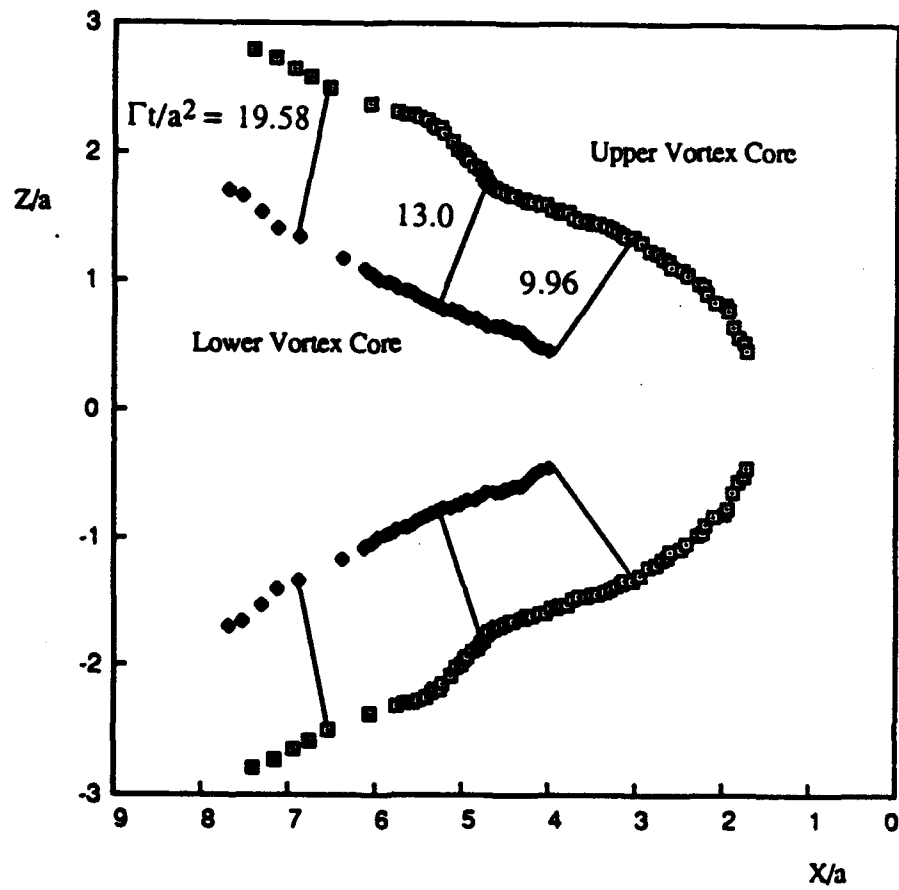


Figure 4.18 Trajectory of vortex core on the free surface.  
 $\Gamma/\nu = 5000$ ,  $\alpha = 20^\circ$ .



(a)  $\Gamma/a^2 = 4.56$   
(Right edge  $X/D_0=1.3$ , Left edge  $X/D_0=5.3$ )

Figure 4.19 Sequence of speckle photographs of double reconnection by interaction of a vortex ring with a free surface,  $\Gamma/\nu = 5000$ ,  $\alpha = 20^\circ$ .



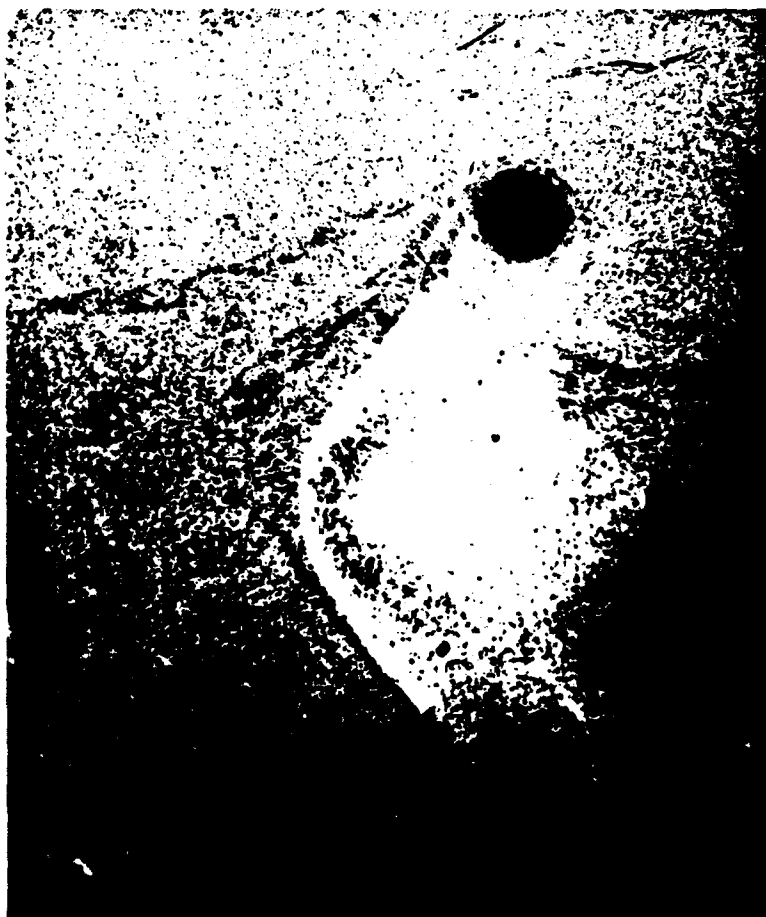
(b)  $\Gamma/a^2 = 5.57$   
(Right edge  $X/D_0=1.3$ , Left edge  $X/D_0=5.3$ )

Figure 4.19 Continued.



(c)  $\Gamma/a^2 = 7.09$   
(Right edge  $X/D_0=1.3$ , Left edge  $X/D_0=5.3$ )

Figure 4.19 Continued.



(d)  $\Gamma/a^2 \approx 8.10$   
(Right edge  $X/D_0=2.3$ , Left edge  $X/D_0=6.3$ )

Figure 4.19 Continued.



(c)  $\Gamma v/a^2 = 9.62$   
(Right edge  $X/D_0=2.8$ , Left edge  $X/D_0=6.8$ )

Figure 4.19 Continued.



(f)  $\Gamma/a^2 = 10.63$   
(Right edge  $X/D_0=3.8$ , Left edge  $X/D_0=7.8$ )

Figure 4.19 Concluded.

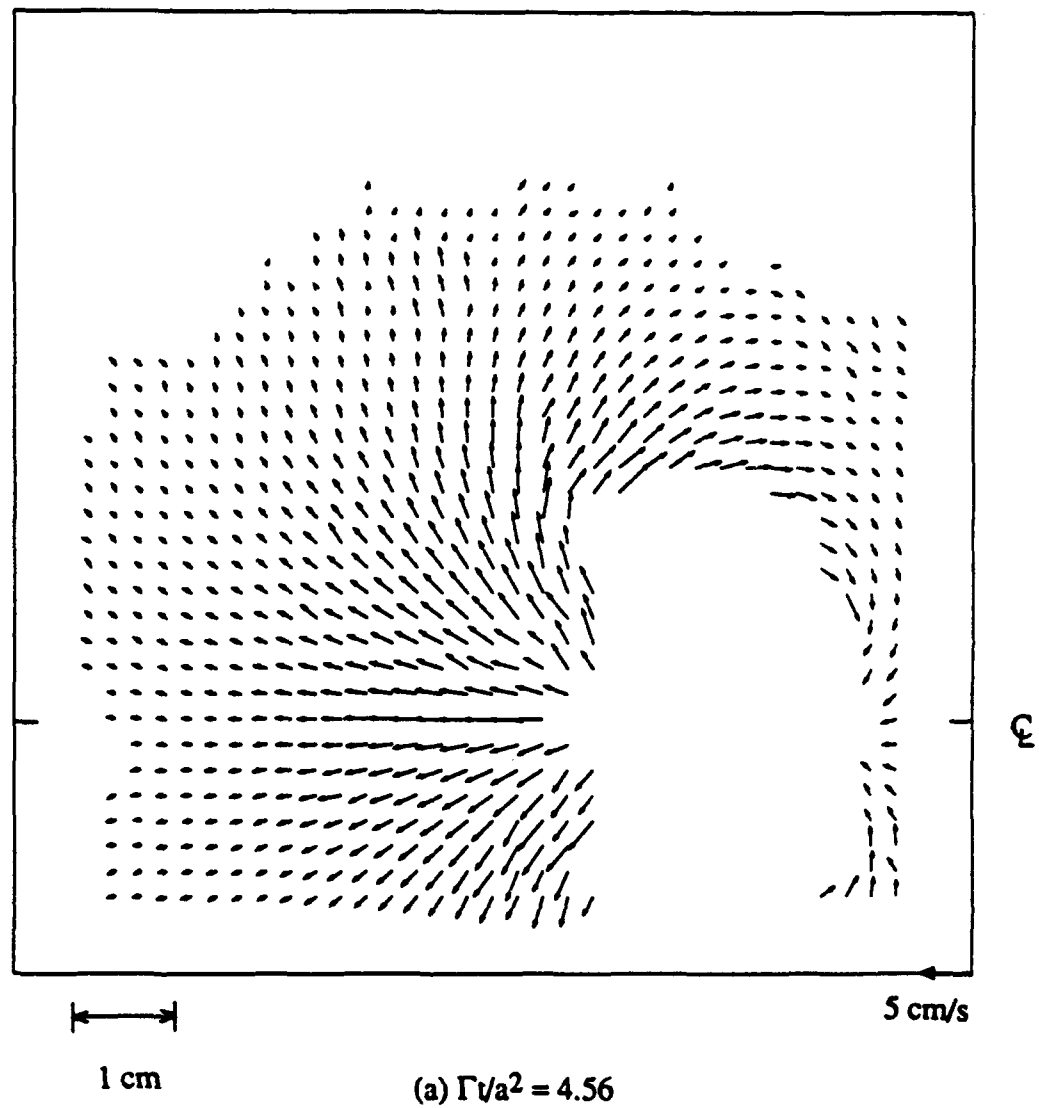
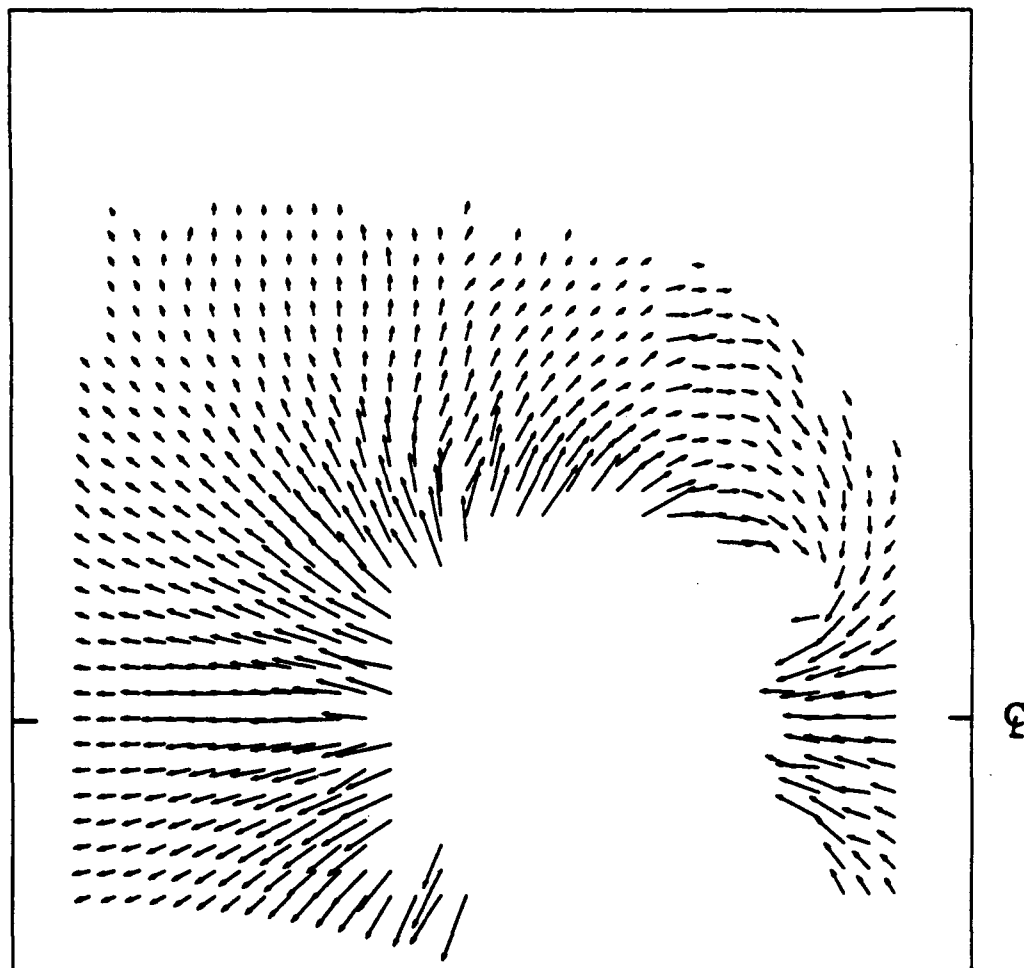


Figure 4.20 Vector plot of a free surface velocity field obtained from speckle photographs in Figure 4.19.



(b)  $\Gamma/a^2 = 5.57$

Figure 4.20 Continued.

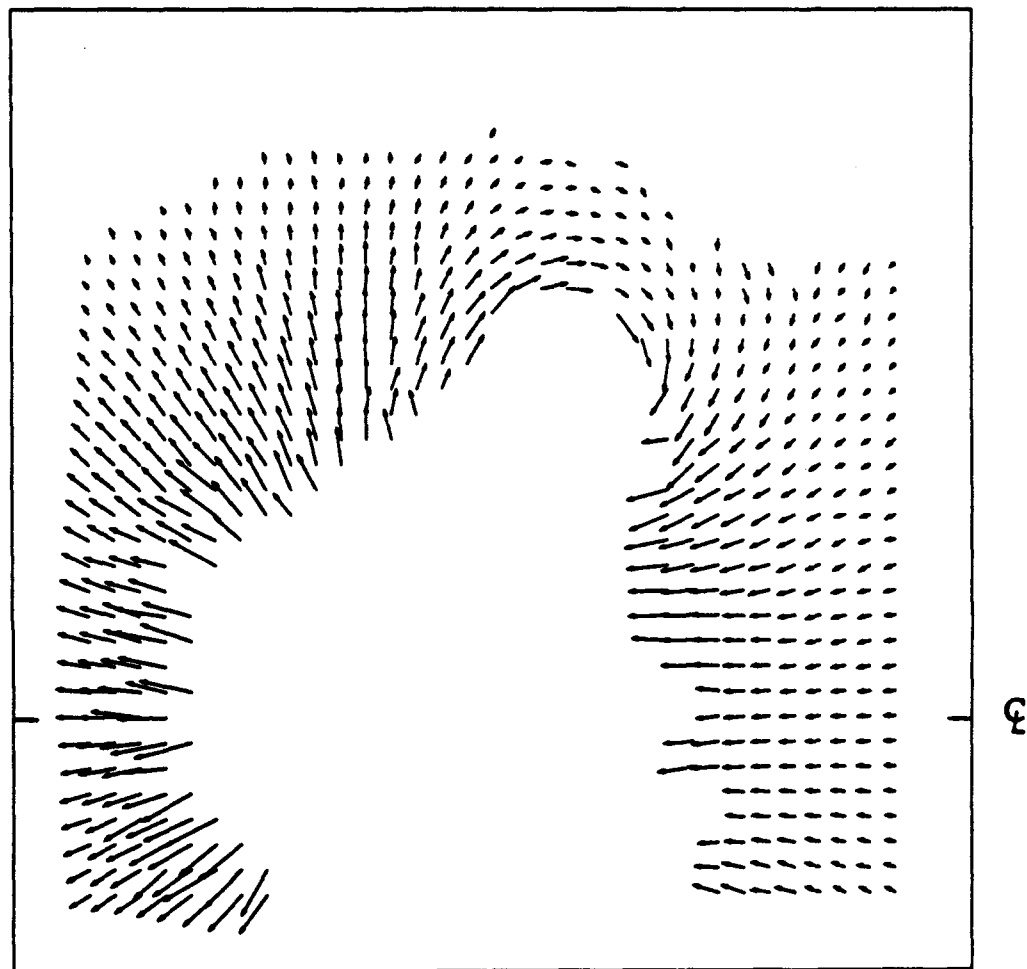
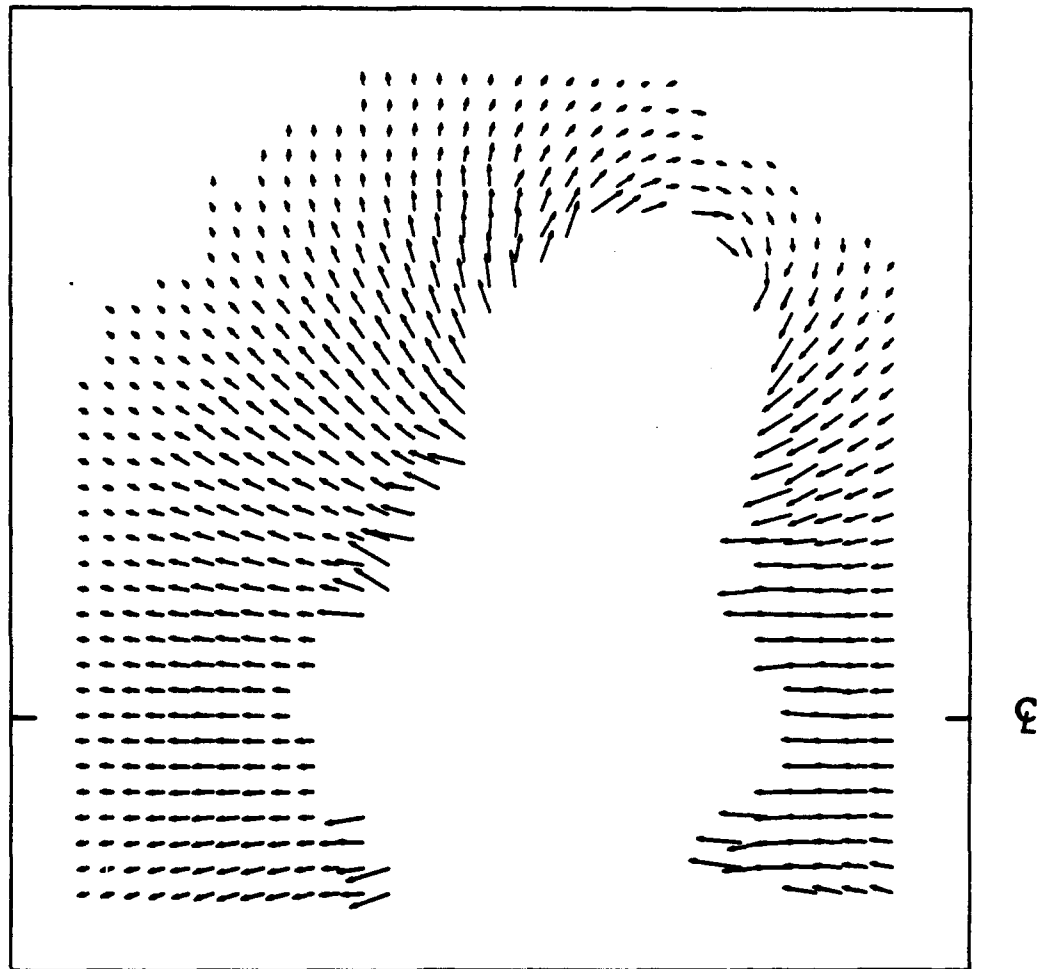
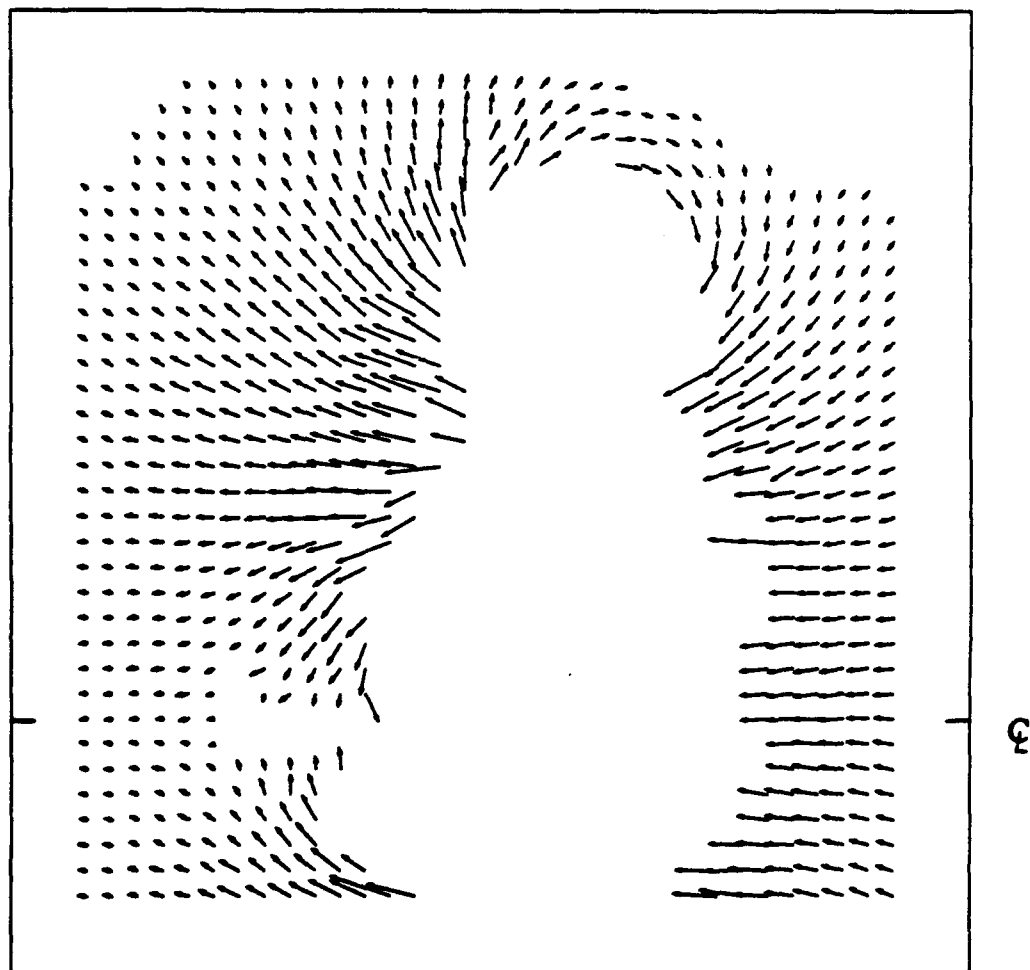
(c)  $\Gamma/a^2 = 7.09$ 

Figure 4.20 Continued.



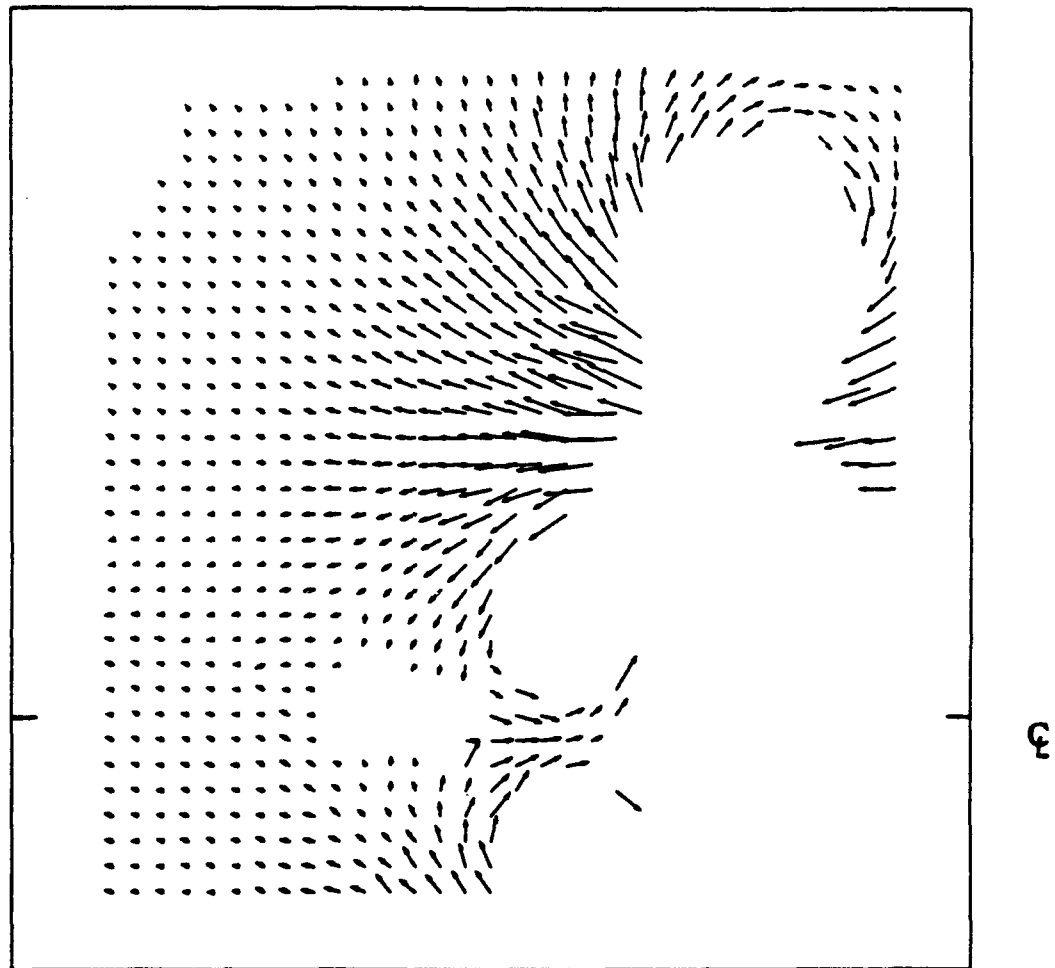
(d)  $\Gamma/a^2 = 8.10$

Figure 4.20 Continued.



(e)  $\Gamma/a^2 = 9.62$

Figure 4.20 Continued.



(f)  $\Gamma/a^2 = 10.63$

Figure 4.20 Concluded.

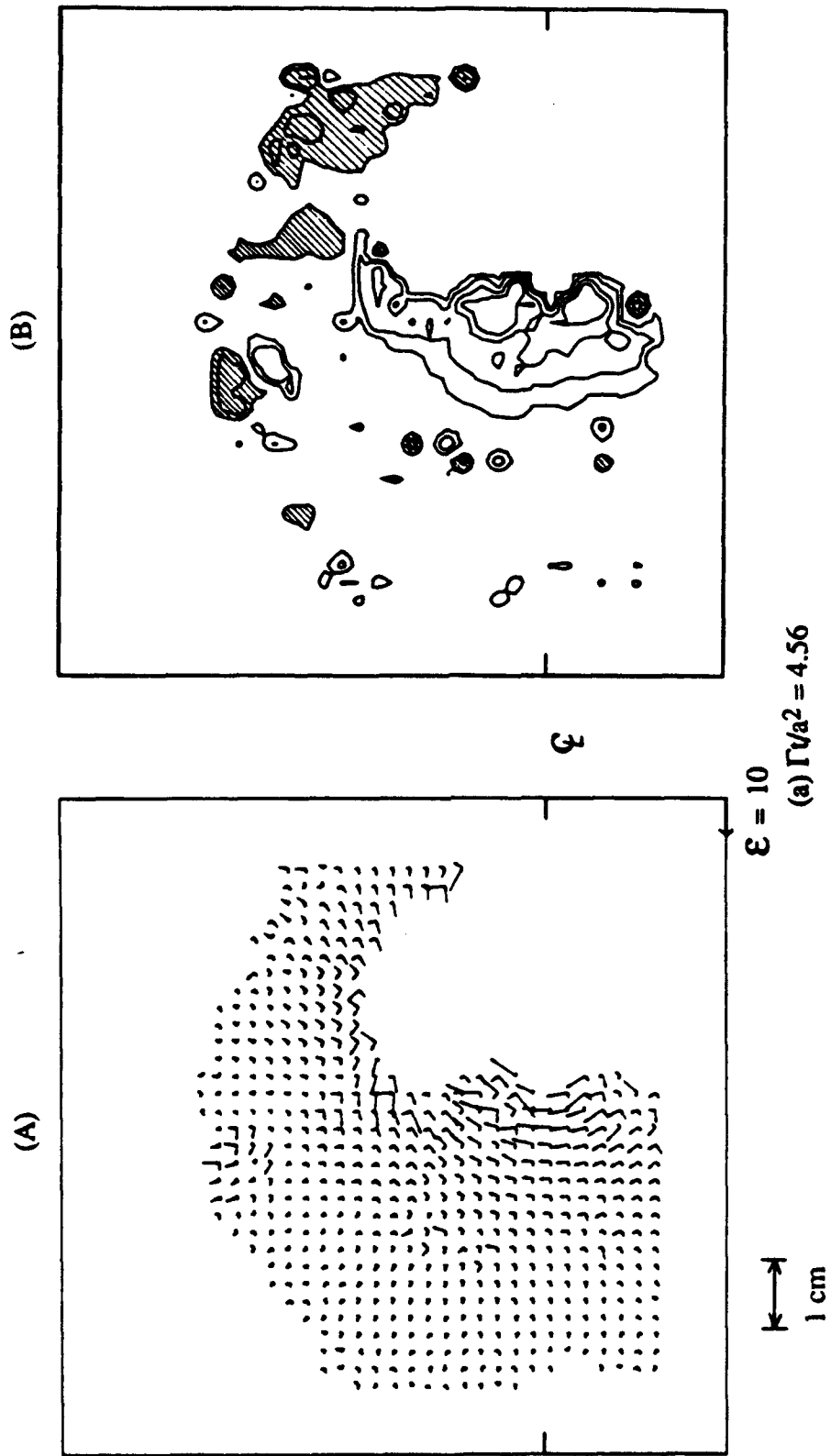


Figure 4.21 Sequence of vector plot and contour plot of free surface strain field obtained from velocity measurements.

(A) Vector plot of  $E_{11}$  and  $E_{22}$ , (B) Contour plot of  $E_{33}$  (Cross line region;  $E_{33} > 0$ ).

(B)

 $\zeta$ 

(A)

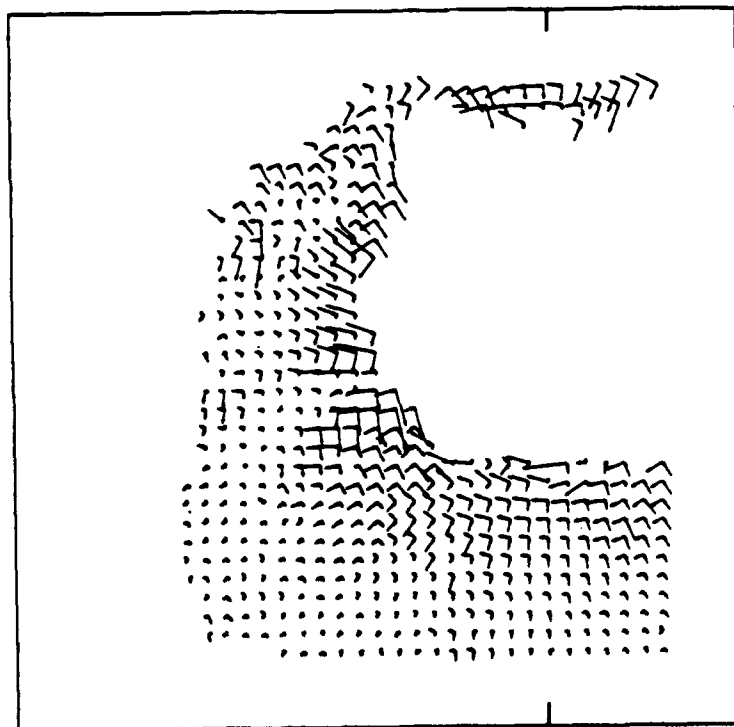
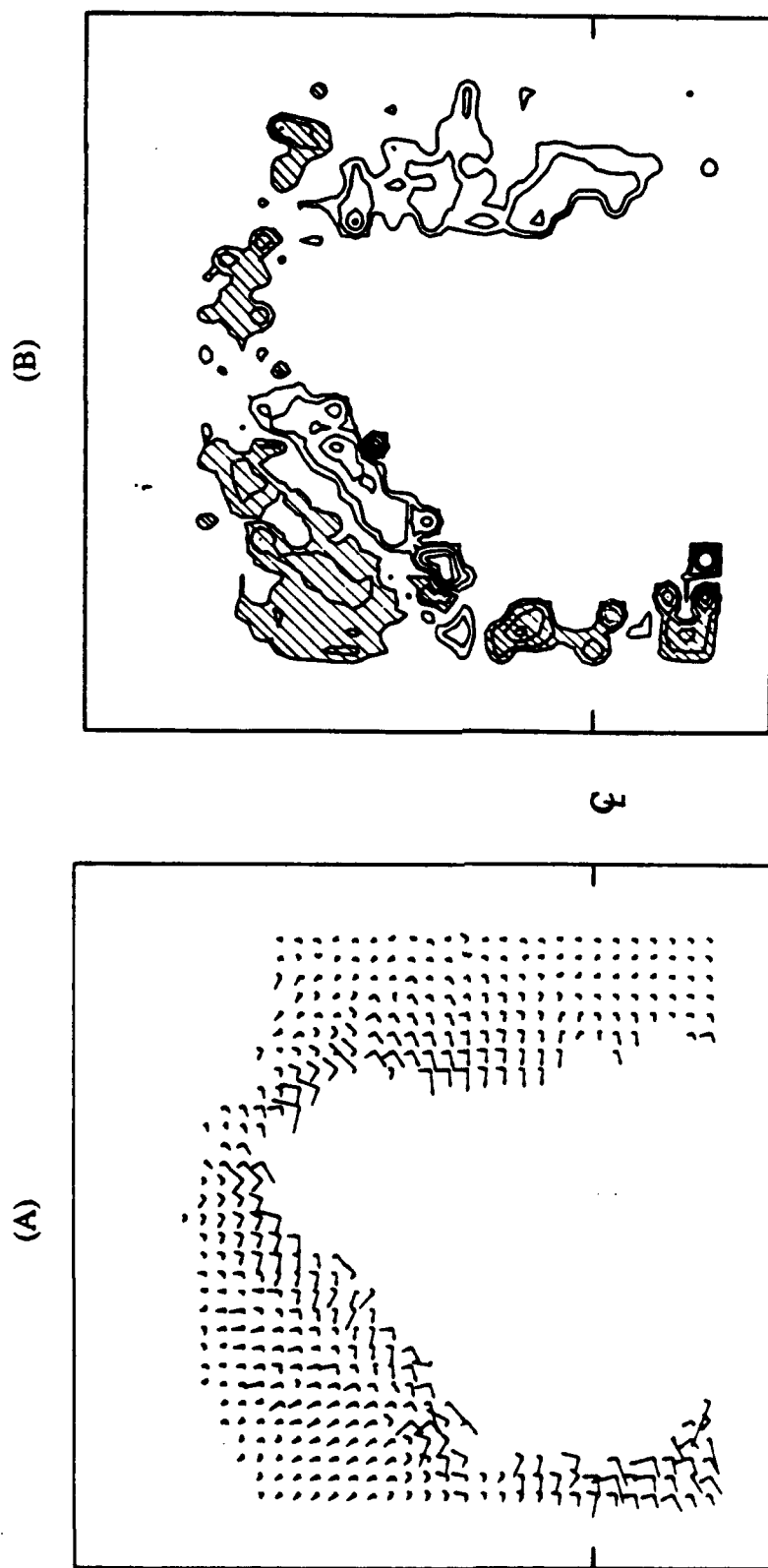
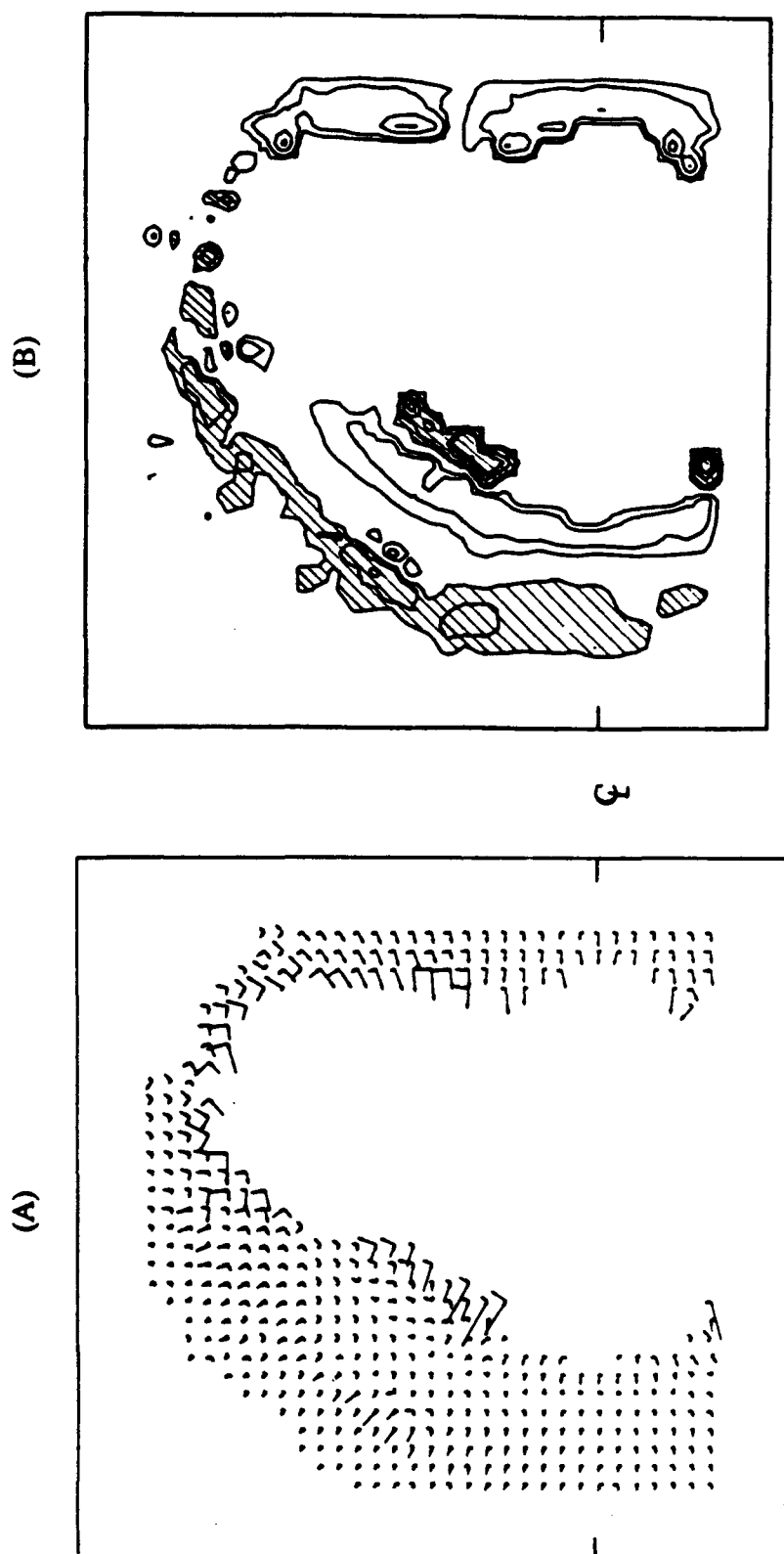
(b)  $\Gamma/a^2 = 5.57$ 

Figure 4.21 Continued.



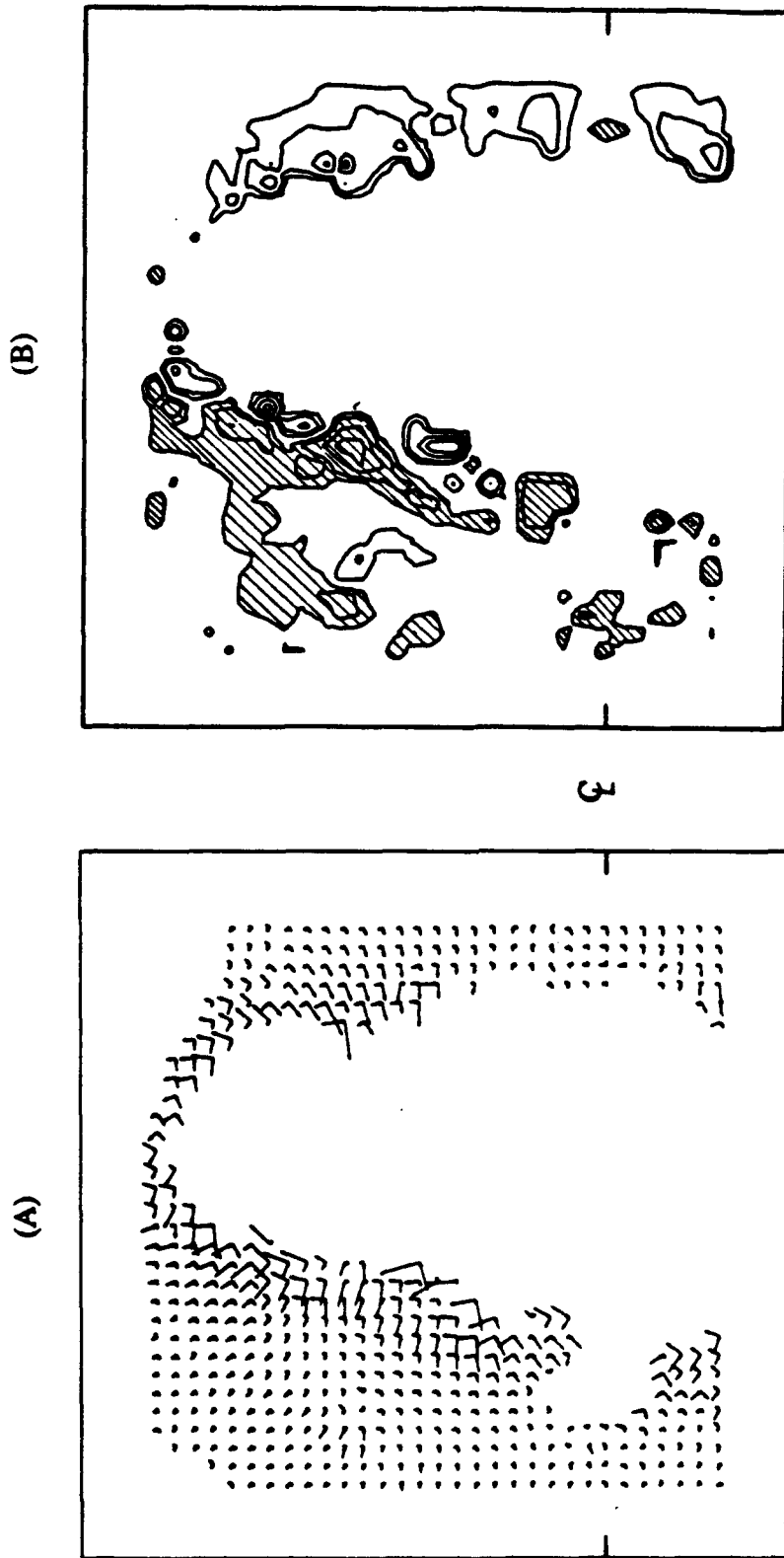
(c)  $\Gamma/a^2 = 7.09$

Figure 4.21 Continued.



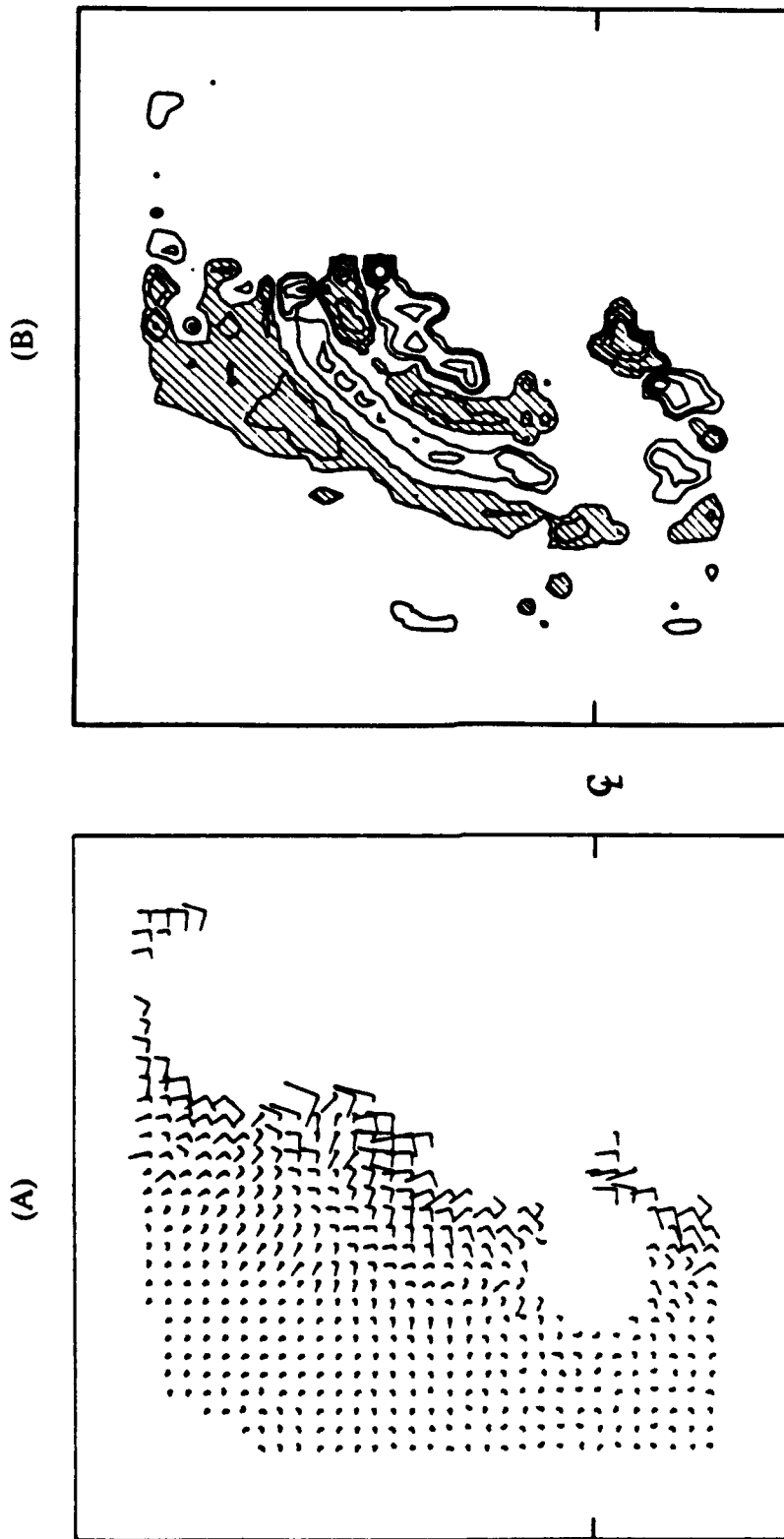
(d)  $\Gamma/a^2 = 8.10$

Figure 4.21 Continued.



(c)  $\Gamma/a^2 = 9.62$

Figure 4.21 Continued.



(C)  $\Gamma/a^2 = 10.63$

Figure 4.21 Concluded.

**TABLE**

Table 4.1 Measurements of Vortex Ring Characteristics

No.	Condition (p, N, m, sec)	$U_0$ (cm/sec)	$\Gamma_0$ (cm <sup>2</sup> /sec)	$L_0/D_0$	$U_t$ (cm/sec)	$\Gamma$ (cm <sup>2</sup> /sec)	a (cm)	$\delta$ (cm)	$\Gamma/(ga^3)^{1/2}$
(1)	p=2, N=3/4, To=0.2	10.0	12.0	0.79	4.36	24.1	2.89	0.67	0.16
(2)	p=1.5, N=3/4, To=0.6	10.9	37.9	2.57	6.02	44.5	3.66	1.02	0.20
(3)	p=4, N=3/4, To=0.2	14.7	29.0	1.16	7.32	49.6*	3.13	1.07	0.29
(4)	p=4, N=1, To=0.2	18.7	46.9	1.47	9.38	63.6	3.29	0.97	0.34
(5)	p=4, N=3/4, To=0.6	17.3	96.3	4.09	9.71	88.1	4.02	1.55	0.35

\*  $\Gamma$  ; Estimated from Figure 4.5.

## APPENDIX A

### JET TANK VORTEX RING GENERATOR

Experiments were conducted using a jet tank vortex ring generator. This facility is a modification of the jet tank used by Madnia (1989) to generate vortex rings parallel to a free surface. The free surface tank and optical system arrangement were the same as described in Figure 2.6 for the simultaneous flow visualizations of the underwater flow and free surface deformation. The set-up for removing the surface contaminants was not installed for this experiment and the small jet tank (53x76x30 cm) instead of the vortex generator system was used to generate vortex rings. The small jet tank which was constructed from PVC and Acrylic plates is shown in Figure A.1. The jet exit orifice, which had a circular-arc-shaped nozzle with a radius equal to the wall thickness, had a circular cross-section 2.54 cm in diameter. The vortex rings were produced by a short duration pressure pulse applied to the small jet tank using the solenoid valve (ASCO 8262A214) and timing circuit. A hot film probe at the jet exit plane was used to measure the velocity trace with respect to the time to determine the vortex ring circulation. Because of the very large mass of water in the jet tank the velocity trace at the exit showed very long duration of water flow. This was considered inadequate. For more systematic studies the vortex generator described in Section 2.2 was designed and built to avoid this problem.

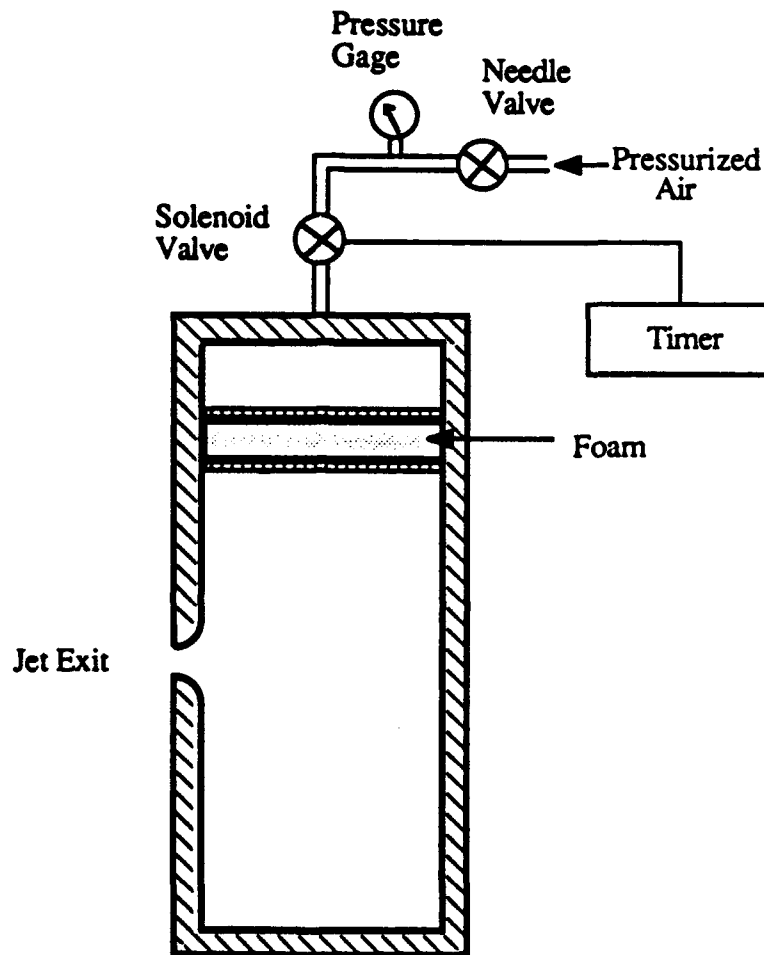


Figure A.1 Schematic diagram of a small jet tank vortex ring generation facility.

## BIBLIOGRAPHY

- Adrian,R.J., "Scattering particles characteristics and their effect on pulsed laser measurements of fluid flow: Speckle velocimetry vs. particle image velocimetry," *Applied Optics*, Vol.23, No.11, pp.1690-1691, 1984.
- Ashurst,W.T. and Meiron,D.I., "Numerical study of vortex reconnection," *Phys.Rev. Lett.*, Vol.58, pp.1632-1635, 1987.
- Adrian,R.J., "An image shifting technique to resolve directional ambiguity in double-pulse laser velocimetry," *Applied Optics*, Vol.25, pp.3855, 1986.
- Adrian,R.J. and Yao,C.S., "Pulsed laser technique application to liquid and gaseous flows and the scattering power of seed materials," *Applied Optics*, Vol.24, pp.44-52, 1985.
- Barker,D.B. and Fourney,M.E., "Measuring fluid velocities with speckle patterns," *Optics letters*, Vol.1, No.4, pp.135-137, 1977.
- Barker,S.J. and Crow,S.C., "The motion of two-dimensional vortex pairs in a ground effect," *J.Fluid Mech.*, Vol.82, pp.659-671, 1977.
- Batchelor,G.K., *An introduction to Fluid Dynamics*, Cambridge University Press, Cambridge, 1967.
- Bernal,L.P. and Madnia,K., "Interaction of a turbulent round jet with the free surface," *Proc.17<sup>th</sup> Symposium of Naval Hydrodynamics*, 1988.
- Berry,M.V. and Hajnal,J.V., "The shadows of floating objects and dissipating vortices," *OPTICA ACTA*, Vol.30, No.1, pp.23-40, 1983.
- Cerra,Jr.A.W. and Smith,C.R., "Experimental observations of vortex ring interaction with the fluid adjacent to a surface," *Report FM-4*, Lehigh Univ., 1983.
- Crow,S.C., "Stability theory for a pair of trailing vortices," *AIAA J*, Vol.18, pp.2172-2179, 1970.
- Dahm,W.J.A., Scheil,C.M. and Tryggvason,G., to appear in *J.Fluid Mech.*, 1989.
- Didden,N., "Untersuchung laminarer, instabiler Ringwirbel mittels Laser-Doppler-Anemometrie," *Mitt.Nr.64*, Gottingen:Max-Planck-Inst.Stromungsforschung, 1977.
- Didden,N., "On the formation of vortex rings: Rolling up and production of circulation," *Journal of Applied Math. and Physics (ZAMP)*, Vol.30, pp.102-116, 1979.

- Dudderar, T.D., Meynart, R. and Simpkins, P.G., "Laser speckle velocimetry," AT&T Bell Laboratories, 1986.
- Dudderar, T.D. and Simpkins, P.G., "Laser speckle photography in a fluid medium," *Nature*, Vol. 270, No. 5632, pp. 45-47, 1977.
- Fohl, T. and Turner, J.S., "Colliding vortex rings," *Physics of Fluids*, Vol. 18, pp. 433-436, 1975.
- Glezer, A., An Experimental Study of a Turbulent Vortex Ring, Ph.D. Thesis, Caltech., 1981.
- Glezer, A., "The formation of vortex rings," *Physics of Fluids*, Vol. 31, No. 12, pp. 3532-3542, 1988.
- Gonzalez, R.C. and Wintz, P., *Digital Image Processing*, Addison-Wesley, Massachusetts, 1977.
- Grousson, R. and Mallick, S., "Study of the flow pattern in a fluid by scattered laser light," *Applied Optics*, Vol. 16, No. 9, pp. 2334-2336, 1977.
- Kambe, T. and Takao, T., "Motion of distorted vortex rings," *J. Phy. Soc. Japan*, Vol. 31, No. 2, pp. 591-599, 1971.
- Lamb, H., *Hydrodynamics*, Dover, New York, 1945.
- Lauterborn, W. and Vogel, A., "Modern optical techniques in fluid mechanics," *Ann. Rev. Fluid Mech.*, Vol. 16, pp. 223-244, 1984.
- Lourenco, L. and Krothapalli, A., "The role of photographic parameters in laser speckle or particle image displacement velocimetry," *Experiments in Fluids*, Vol. 5, pp. 29-32, 1987.
- Lourenco, L., Krothapalli, A., Buchlin, J.M. and Riethmuller, M.L., "A non-invasive experimental technique for the measurement of unsteady velocity field and vorticity field," AGARD-CP-413, pp. 23-1~23-9, 1986.
- Madnia, K., Interaction of a Turbulent Round Jet with the Free Surface, Ph.D. Thesis, University of Michigan, 1989.
- Maxworthy, T., "The structure and stability of vortex rings," *J. Fluid Mech.*, Vol. 51, pp. 15-32, 1972.
- Maxworthy, T., "Some experimental studies of vortex rings," *J. Fluid Mech.*, Vol. 81, pp. 465-495, 1977.
- Meynart, R., "Digital image processing for speckle flow velocimetry," *Rev. Sci. Instrm.* Vol. 53, No. 1, 1982.
- Meynart, R., "Instantaneous velocity field measurements in unsteady gas flow by speckle velocimetry," *Applied Optics*, Vol. 22, No. 4, pp. 535-540, 1983.
- Meynart, R., "Speckle velocimetry study of vortex pairing in a low-Re. unexited jet," *Physics of Fluids*, Vol. 26, No. 8, pp. 2074-2079, 1983.

- Merzkirch, W., Flow Visualization, Academic Press. Inc., Second Edition, 1987.
- Morton, B.R., "The strength of vortex and swirling core flows," J.Fluid Mech., Vol.38, Part 2, pp.315-333, 1969.
- Morton, B.R., "The generation and decay of vorticity," Geophys.Astrophys.Fluid Dynamics, Vol.28, pp.277-308, 1984.
- Oshima, Y., "Motion of vortex rings in water," J.Phy.Soc., Japan, Vol.32, No.4, pp.1125-1131, 1972.
- Oshima, Y. and Asaka, S., "Interaction of two vortex rings along parallel axes in air," J.Phy.Soc., Japan, Vol.42, No.2, pp.708-713, 1977.
- Oshima, Y. and Izutsu, N., "Cross-linking of two vortex rings," Physics of Fluids, Vol.31, No.9, pp.2401-2403, 1988.
- Pearson, J.B., Hilko, B., Houtman, H. and Curzon, F.L., "Laser speckle measurements of flow velocity in a simplified gas jet," Rev.Sci.Instrum., Vol.57, No.3, pp.374-376, 1986.
- Saffman, P.G., "The velocity of viscous vortex rings," Studies in Applied Mathematics, Vol.49, pp.371-380, 1970.
- Saffman, P.G., "On the formation of vortex rings," Studies in Applied Mathematics, Vol.54, pp.261-268, 1975.
- Saffman, P.G. and Baker, R.G., "Vortex interactions," Annual Review of Fluid Mechanics, Vol.11, pp.95-122, 1979.
- Sarpkaya, T., "Trailing vortices in homogeneous and density-stratified media," J.Fluid Mech., Vol.136, pp.85-109, 1983.
- Sarpkaya, T. and Henderson Jr., D.O., "Free surface scars and striations due to trailing vortices generated by a submerged lifting surface," AIAA 23rd Aerospace Meeting, Jan. 14-17, 1985.
- Schatzle, P.R., An Experimental Study of Fusion of Vortex Rings, Ph.D Thesis, Caltech., 1987.
- Schlichting, H., Boundary Layer Theory, McGraw-Hill, New York, 1955.
- Simpkins, P.G. and Dudderar, T.D., "Laser speckle measurements of transient Bernard convection," J.Fluid Mech., Vol.89, No.4, pp.665-671, 1978.
- Sterling, M.H., Gorman, M., Widmann, P.J., Coffman, S.C., Strozier, J. and Kiehn, R.M., "Why are these disks dark? The optics of Rankine vortices," Physics of Fluids, Vol.30, No.11, pp.3624-3626, 1987.
- Stetson, K.A., "A review of speckle photography and interferometry," Optical Engineering, Vol.14, NO.5, pp.482-489, 1975.
- Sullivan, J.P., Widnall, S.E. and Ezekiel, S., "Study of vortex rings using a laser doppler velocimeter," AIAA J, Vol.11, pp.1384-1389, 1973.

Tiziani, H.J., "Application of speckling for in-plane vibration analysis," *Optica ACTA*, Vol.18, No.12, pp.891-902, 1971.

Vest, C.M., *Holographic Interferometry*, Wiley, New York, 1979.

Walker, J.D.A., Smith, C.R., Cerra, A.W. and Doligalski, T.L., "The impact of a vortex ring on a wall," *J.Fluid Mech.*, Vol.181, pp.99-140, 1984

Welch, P.D., "The use of fast Fourier transform for the estimation of power spectra: A method based on time averaging over short, modified periodograms," *IEEE Transactions on Audio and Electroacoustics*, Vol.AU-15, No.2, 1967.

Widnall, S.E. and Sullivan, J.P., "On the stability of vortex rings," *Proc.Roy.Soc.*, Vol.A332, pp.465-495, 1973.

Willmarth, W.W., "The effect of cross flow and isolated roughness elements on the boundary layer and wall pressure fluctuation on circular cylinders," The University of Michigan Dept. of Aerospace Engr. Report # 014439-01, 4.

Willmarth, W.W., Tryggvason, G., Hirs, A. and Yu, D., "Vortex pair generation and interaction with a free surface," *Phys.Fluids a*, Vol.1, No.2, 1989.